DESIGN OPTIMIZATION STUDIES FOR ACTIVE MATRIX FLAT PANEL IMAGERS BASED ON SEGMENTED CRYSTALLINE SCINTILLATORS FOR RADIOTHERAPY IMAGING

by

Langechuan Liu

A dissertation submitted in partial fulfillment
of the requirements for the degree of
Doctor of Philosophy
(Physics)
in the University of Michigan
2015

Doctoral Committee:

Professor Larry E. Antonuk, Chair
Professor James M. Balter
Emeritus Professor Frederick D. Becchetti Jr
Assistant Professor Emanuel Gull
Professor Cagliyan Kurdak

業精於勤荒於嬉　行成於思毀於隨
—— 韓愈《進學解》（唐）元和八年

Study excels with diligence and decays with indolence
Conduct succeeds by thinking and fails by following
——— Han Yu, *On Knowledge Improvement* (A.D. 813)

Dedicated to those who shaped my life.

ACKNOWLEDGEMENT

Scientific research to unravel the mysteries of nature resembles in many ways a quest to uncover lost treasures. Without guidance, the treasure hunter would be hopelessly disoriented. Without company, the journey would be a lonely one. I am grateful and lucky to have had both for my quest.

First of all, I would like to thank my academic advisor and committee chair Dr. Larry Antonuk for his guidance and mentorship. His constant encouragement and support have motivated me to go further and achieve more than I thought I could. From the orientation of my research to my writing styles, his feedbacks have always been of tremendous help, which supported me to overcome many critical situations and finish this dissertation timely. I also greatly appreciate the comments and feedbacks from my committee members who kindly agreed to examine this dissertation.

My colleagues, the present and past members from the flat-panel imaging group of the Department of Radiation Oncology, have greatly contributed to the work presented here and therefore deserve special credit. I would like to thank Dr. Youcef El-Mohri and Dr. Qihua Zhao for shedding light on the conundrums I encountered during my research. My sincere thanks need to be addressed to Dr. Hao Jiang and

fellow graduate students Martin Konicezk, Albert K. Liang and Richard Choroszucha for numerous heated discussions that helped to fill gaps in my knowledge. I also thank Allen Young, John McDonald, Chuck Martelli and Mike Yeakey for their technical and academic support. Working with such a group of diverse and talented scientists and engineers has been one of the most intellectually rewarding and enriching experiences in my graduate life.

Finally, I want to extend my deepest gratitude to my family – my parents, who have always been supportive of my decisions with full confidence in me, and my wife, Lina, who has accompanied me during the hardships and has shared the joy for every little discovery I made.

TABLE OF CONTENTS

LIST OF FIGURES

LIST OF TABLES

LIST OF APPENDICES

CHAPTER 1

INTRODUCTION

I. EXTERNAL PHOTON BEAM RADIOTHERAPY

Well over a century after their discovery by Wilhelm Röntgen in 1895,[1] X rays continue to be one of the most versatile tools in modern medicine. For example, X rays at kilovoltage (kV) energies are used for diagnostic imaging procedures such as radiography and computed tomography (CT), and megavoltage (MV) X rays are used to kill cancerous cells using a variety of treatment techniques.

One such technique, referred to as external photon beam radiotherapy, is commonly performed using a gantry-mounted medical linear accelerator (LINAC). In such treatment machines, electrons are accelerated to MeV energies before colliding with a high-Z metallic target (e.g., tungsten), generating Bremsstrahlung X rays (and much smaller amounts of characteristic X rays). These X rays are filtered and collimated to achieve clinically desirable energy spectra, intensity profiles and field shapes, and are typically delivered to the patient in a "cross-firing" manner from different angles via rotation of the LINAC gantry around a patient support couch.

In external photon beam radiotherapy, normal tissues along the radiation path will inevitably be irradiated, potentially leading to adverse side effects. For that reason, a central goal is to maximize the radiation dose to the tumor while minimizing the dose to surrounding normal tissues. This goal is assisted through the routine use of MV portal imaging and/or kV cone beam CT (CBCT) imaging in the treatment room.[2, 3]

II. IMAGING IN RADIOTHERAPY

II.A. Portal imaging and MV AMFPIs

Portal imaging entails acquisition of projection images of the patient in the treatment position using the treatment beam and can be carried out in two ways referred to as *localization* and *verification* imaging. *Localization imaging* is performed immediately prior to delivery of the treatment dose to allow for possible adjustment of patient setup while *verification imaging* is performed during treatment to provide a record of treatment delivery. The electronic portal imaging devices (EPIDs) presently employed to perform such imaging are typically based on the technology of active matrix flat-panel imagers (AMFPIs).[4]

An AMFPI consists of an x-ray converter coupled to an underlying backplane. The backplane comprises a two-dimensional array of pixels, each of which contains a pixel storage capacitor connected to a switch that typically takes the form of a hydrogenated amorphous silicon (a-Si:H) thin film transistor (TFT). An electronic acquisition system controls the operation and readout of the array.

Depending on the strategy employed for the conversion of incident radiation, AMFPIs can be divided into two broad categories – *direct* and *indirect* detection. In an *indirect* detection AMFPI, the converter consists of a scintillating layer which is positioned directly over the array. In this case, the pixel storage capacitor takes the form of a photosensor, most commonly an a-Si:H photodiode across which a reverse bias voltage is applied. In such AMFPIs, radiation energy is converted in the scintillating layer to optical photons, some of which escape into the photodiodes where they are converted with high efficiency into electron-hole pairs. The signal induced by the movement of electron-hole pairs is stored in the capacitive structure of the photodiode until readout. By comparison, in a *direct* detection AMFPI, the converter consists of a layer of photoconductive material (typically amorphous selenium, a-Se). This photoconductive layer is deposited directly on the surface of the array – electrically coupling it to the pixel storage capacitors. In this case, the energy of the incident radiation is directly converted into electron-hole pairs in the photoconductive layer and the imaging signal is stored in the storage capacitors until readout.

MV AMFPIs fall into the indirect detection category and employ a converter incorporating a relatively thick, powdered-phosphor screen along with an overlying metal plate (e.g., ~360 μm of Gd_2O_2S:Tb with a surface density of ~133 mg/cm^2 and a ~1 mm thick copper plate).[4-7] The metal plate filters low energy, secondary X rays and electrons scattered from the patient and LINAC as well as increases the quantum efficiency (QE) of the converter through generation of secondary electrons. Quantum

efficiency is defined as the ratio of the number of detected X rays to the number of incident X rays. Due to their many advantages,[7] MV AMFPIs have largely replaced portal film and earlier EPID technologies, and are currently regarded as the gold standard for portal imaging.[7, 8]

While the usefulness of MV AMFPIs has made these devices nearly ubiquitous in radiotherapy environments, their performance is strongly constrained by their inefficient use of the incident radiation. Specifically, the QE for MV AMFPIs is only ~2% at 6 MV (by convention, a 6 MV beam energy refers to the Bremsstrahlung spectrum generated by 6 MeV electrons in a radiotherapy treatment machine). Simply increasing the thickness of the powdered-phosphor screen to increase QE results in spatial resolution loss due to increased spread of optical photons.[9, 10] As explained below, this tradeoff between QE and spatial resolution leads to a dilemma that inhibits performance improvement through use of thicker powdered-phosphor screens.

To explain this dilemma, it is useful to introduce the concept known as detective quantum efficiency (DQE). DQE is a widely-accepted, observer-independent metric that serves to characterize the imaging performance of x-ray imaging systems. It is related to the efficiency of transfer of signal-to-noise information from the input to the output of an imaging system, and can be defined as

$$DQE = \frac{SNR_{out}^2}{SNR_{in}^2} \qquad (0 \leq DQE \leq 1). \tag{1.1}$$

In this equation, SNR_{in} and SNR_{out} represent the signal-to-noise ratio of the system at the input and output, respectively. It is desirable for the DQE of a system to be large and as close to 1 as possible. In general, DQE is determined as a function of spatial frequency, f, which is the appropriate independent variable for x-ray imaging systems. The frequency-dependent DQE can be mathematically expressed in terms of measurable quantities as follows

$$DQE(f) = \frac{\bar{A}^2 MTF^2(f)}{\bar{q}_0 NPS(f)}. \tag{1.2}$$

In this expression, $\bar{q}_0$ is the incident x-ray fluence (i.e., number per unit area), $\bar{A}$ is the average pixel signal, $MTF(f)$ is the modulation transfer function (MTF) (which characterizes the spatial resolution of the imaging system), and $NPS(f)$ is the noise power spectrum (which characterizes the noise properties of the system). In Eq. (1.2), both $\bar{A}$ and $NPS(f)$ are directly proportional to QE, therefore

$$DQE(f) \propto QE \times MTF^2(f). \tag{1.3}$$

Due to the aforementioned tradeoff between QE and spatial resolution in MV AMFPIs incorporating a powdered-phosphor screen, the approach of increasing the screen thickness will not generally result in DQE improvement for such imagers.[9]

In addition to degraded spatial resolution, the use of thicker scintillating layers based on materials with poor optical transparency (such as powdered-phosphors) will also lead to increased levels of NPS and, based on Eq. (1.2), result in further degradation of DQE. This increase in NPS is due to higher Swank noise.[11] Swank noise originates from the variation in the pulse height distribution (PHD) – a

distribution of signal response from the detection of each X ray. Swank noise can be quantitatively represented by a parameter referred to as Swank factor, which ranges from 0 to 1, where higher values correspond to lower Swank noise. Swank factors can be calculated using

$$I = \frac{M_1^2}{M_0 M_2}, \tag{1.4}$$

where M_i is the i^{th} order moment of the PHD, $P(x)$,

$$M_i = \sum_k x_k^i \, P(x_k). \tag{1.5}$$

In Eq. (1.5), x_k corresponds to the energy of the kth bin of the discrete PHD. In the absence of electronic noise and noise power aliasing, the value of DQE at zero spatial frequency can be expressed as

$$DQE(0) = QE \times I. \tag{1.6}$$

Constrained by a Swank factor of ~0.5 and a low QE of ~2%, the DQE(0) for MV AMFPIs based on powdered-phosphor screens is ~1%, which is much lower than that for AMFPIs designed for kV imaging (up to ~80%).[12-15]

II.B. Volumetric imaging based on AMFPIs

In portal imaging, the projection of the three-dimensional patient positioning information onto a two-dimensional plane results in overlap of anatomical structures, obscuring the visibility of the soft tissues in the vicinity of the tumor region. In order to achieve better soft-tissue visualization, various volumetric imaging techniques using kV or MV radiation sources have been previously developed.[8, 16-23] One such technique involving the use of a gantry-mounted kV cone-beam CT (CBCT) system

has been widely employed during the last decade.[16-18] A kV CBCT system consists of a dedicated diagnostic x-ray source and an indirect detection AMFPI employing a converter typically consisting of a CsI:Tl screen (typically ~600 μm thick).[24-26] The kV source and the AMFPI are positioned so that their imaging axis is at a 90° rotational offset with respect to the central axis of the treatment beam. Such systems can provide diagnostic quality volumetric images with soft-tissue information in the treatment room at an imaging dose of only a few centigray (cGy).

CBCT can also be performed using the treatment beam itself with a MV AMFPI. Although the contrast of anatomical structures is inherently lower at MV energies compared to kV energies (due to the smaller difference in attenuation properties between contrasting objects at MV energies), a relatively high degree of soft-tissue visualization is nevertheless achievable through MV CBCT.[8, 19-23] Moreover, compared to kV CBCT, MV CBCT has several distinct advantages. MV CBCT images exhibit significantly reduced streak artifacts for patients with metal implants,[8, 19, 20] and CT-numbers obtained from MV CBCT can be more readily used for dose calculation in treatment planning.[21-23] The fact that MV CBCT images are obtained using the therapy beam itself also eliminates the type of geometric uncertainties relative to the treatment beam introduced by the use of an independent kV source and imager.

A major obstacle to widespread clinical implementation of MV CBCT lies in the low DQE of MV AMFPIs. As a result, in order to achieve a reasonable degree of

soft-tissue visualization, MV CBCT would require rather high (and, most likely, clinically impractical) imaging doses (e.g., ~50-200 cGy).[27-29]

II.C. Thick, segmented scintillators

In response to the challenge posed by the extremely low DQE of commercially available, powdered-phosphor-based MV AMFPIs (referred to as *conventional* MV AMFPIs), many strategies have been previously explored to increase DQE performance — with various prototypes based on area [30-33] and linear [34-37] detectors providing DQE values as high as ~9% and 20%, respectively. In addition, an innovative linear scanning system based on a double row of discrete $ZnWO_4$ crystals was shown to provide a QE of ~50%.[38] One strategy that has shown particular promise in recent empirical and theoretical investigations involves replacement of the powdered-phosphor screen with a thick, crystalline, segmented scintillator.[39-44] As illustrated in Fig. 1.1, segmented scintillators consist of a two-dimensional matrix of high-aspect-ratio elements in the form of scintillating crystals separated by septal wall material (e.g., polystyrene) which limits lateral spread of optical photons.[42] In addition, compared to a powdered-phosphor screen, the superior optical transparency of crystalline scintillator material limits the deterioration of DQE due to optical Swank noise.[32, 42] These properties allow segmented scintillators to achieve progressively higher DQE performance with increasing thickness, while limiting the loss of spatial resolution due to optical blur. For example, a prototype MV AMFPI incorporating an ~1.13 cm thick segmented BGO ($Bi_4Ge_3O_{12}$)

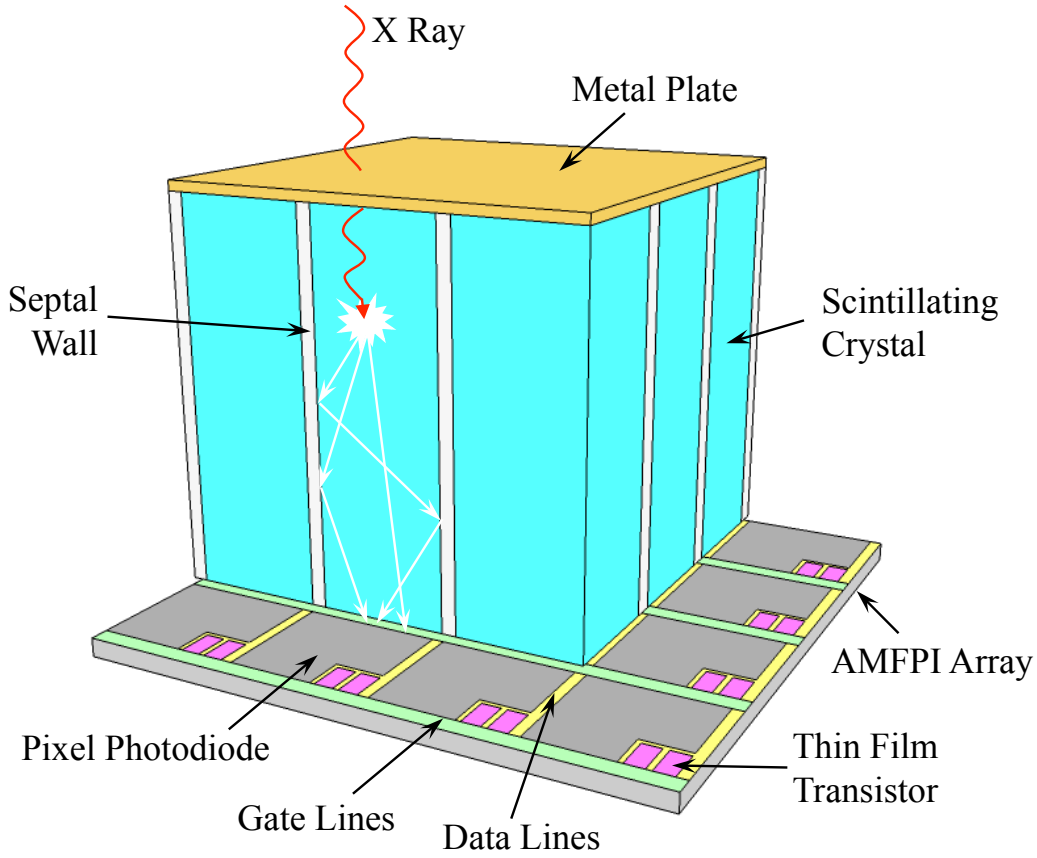

Figure 1.1. Schematic cross-sectional view illustrating selected details of a segmented scintillator-based x-ray converter coupled to an underlying AMFPI array (without the use of any additional coupling medium). In this figure, individual scintillating crystals, as well as septal walls, are illustrated. The structures portrayed on the part of the array extending beyond the footprint of the illustrated portion of the converter correspond to address lines, photodiodes and thin film addressing transistors. The interaction of incident x-ray radiation with the converter, as well as the generation and transport of optical photons within a scintillating crystal, are also portrayed.

scintillator with an element-to-element pitch of 1.016 mm has been shown to provide a maximum DQE value of ~20%, which is ~20 times greater than that of a conventional MV AMFPI.[43]

The primary importance of such order-of-magnitude increases in DQE is that the dose necessary to capture a single projection image can be greatly reduced down

to as low as a single beam pulse. This, in turn, makes it possible to acquire the large number of projection images required to perform megavoltage cone-beam computed tomography (MV CBCT) at much lower, and more clinically practical doses. For example, using the aforementioned prototype BGO segmented scintillator, a tomographical scan with 180 projections was performed at a total dose comparable to that required to capture a single projection image with a conventional MV AMFPI.[37, 44] From the resulting reconstructed CT images, differences in electron density as small as ~2.76% were delineated.

III. IMPROVING SEGMENTED SCINTILLATOR DESIGNS THROUGH THEORETICAL MODELING

Given the encouraging results obtained in earlier investigations of the segmented scintillator approach, it is of interest to examine how variations in the design of segmented scintillators can affect performance. This was pursued through theoretical modeling involving Monte Carlo simulation, which has been previously proven to be an effective tool for predicting the imaging performance of AMFPIs incorporating segmented scintillators.[40-43, 45-48] In the case of indirect detection AMFPIs, such simulation is generally divided into two stages, *radiation* transport and *optical* transport. Radiation transport traces the propagation and interaction of primary X rays (i.e., those directly originating from the x-ray source) and secondary radiation quanta (such as recoil X rays, electrons and positrons) until the radiation quanta deposit their entire energies within, or exit, the region of interest. Optical transport tracks the propagation and interaction of optical photons generated from the

energy deposited in the scintillating layer until they are absorbed in the scintillator, or are detected by the AMFPI array, or leave the region of interest.

Theoretical modeling through Monte Carlo simulation makes it possible to gain valuable insight about the performance of a wide range of hypothetical segmented scintillator designs without the expense of fabricating numerous prototypes. In particular, such modeling provides a powerful tool for investigating a series of challenges that are of critical importance for the identification of designs that offer maximum imaging performance. These challenges are described below.

III.A. Countering beam divergence

For scintillator thicknesses greater than ~1 cm, spatial resolution (quantified by MTF) and DQE performance are increasingly compromised by geometric beam divergence.[47] This effect originates from the oblique angle of incidence of primary X rays originating from the source with respect to the side walls of a segmented scintillator at locations away from the central beam axis. As a result, primary X rays following a given track can deposit energy in different neighboring elements depending on the point of interaction across the thickness of the scintillator — resulting in spatial resolution loss and DQE degradation.

One possible strategy to counter the performance degrading effects of beam divergence is to construct the individual segmented scintillator elements so that they are focused toward the radiation source. Since beam divergence is a geometric

effect [49, 50] and is expected to be primarily determined by the locations where incident X rays interact,[47] the use of radiation transport simulation (without inclusion of optical effects) is sufficient to investigate this effect.

III.B. Accounting for optical effects in simulation

In order to perform more general evaluation (beyond the effect of beam divergence) of hypothetical scintillator designs and to facilitate direct comparison between theoretical and empirical results, a complete simulation framework accounting for *both radiation and optical* effects is needed. An obvious approach for implementing such a complete framework would involve Monte Carlo based, event-by-event simulation of both radiation and optical transport so as to account for the most important physical effects.[42, 45] However, since scintillation yields range from ~8,000 to 54,000 optical photons generated per MeV of deposited x-ray energy for the most promising scintillating materials (BGO, LYSO, $CdWO_4$ and CsI:Tl),[51, 52] the computational demands related to optical transport would greatly exceed those related to radiation transport by several orders of magnitude. This, plus the fact that the number of x-ray histories required for such studies is itself often very large (so as to achieve clinically realistic doses or a desired level of statistical precision), means that studies quickly become computationally too burdensome to be carried out on practical timescales. One way to circumvent this restriction is to simply reduce the scintillation yield, but this can be done only up to the point where deviations from results obtained with the nominal yield begin to fall outside the tolerance of the study. For example, in a previous study of the optical Swank factor of segmented

scintillators,[42] while it was possible to reduce the yield for CsI:Tl from 54,000 to 5,400 in the simulations, no such reduction for BGO is feasible given the already relatively low yield (8,000 photons per MeV of deposited energy) of this material.

In order to account for optical effects within practical computational time scales, a new type of simulation technique was required in order to circumvent the prohibitive computational burden of brute-force Monte Carlo simulation of both radiation and optical transport.

III.C. Investigations of the design of a dual energy, kV/MV imager

Expansion of the clinical utility of kV CBCT could be achieved through use of a beam's eye view (BEV) geometry in which the diagnostic source is positioned so as to provide the same radiation field of view (FOV) as that of the MV treatment source. Such BEV kV imaging has been investigated using different approaches: through integration of an additional kV source in the treatment head,[53-55] and through modification of the treatment beam line so as to increase the low energy component of the beam.[56-67] The latter, imaging beam line approach has been explored through the use of a low-Z target,[56-65] a modified linear accelerator waveguide,[66] or reduction of the electron beam energy.[67] Compared with current kV CBCT imaging which is performed with the aforementioned rotational offset of the kV source relative to the MV source, BEV kV imaging would eliminate drawbacks such as the geometric uncertainties associated with that offset and the need for additional quality assurance effort to ensure the coincidence of the isocenters of the kV and MV radiation fields,

while preserving the superior contrast of kV images compared to that obtained using the MV treatment beam. BEV kV imaging could also significantly enhance the effectiveness of real-time tracking of tumors.[68] Furthermore, the coincidence of the kV and MV FOVs would facilitate reconstruction of images with the complementary strengths of kV and MV imaging, such as superior contrast-to-noise ratio (CNR) and reduced metal artifacts, respectively. (Note that CBCT imaging based on a combination of kV and MV image acquisition has been explored with a conventional, orthogonally mounted kV system.)[69, 70]

Motivated by previous studies of kV BEV imaging as well as by the encouraging performance of MV AMFPIs incorporating segmented scintillators, it is of interest to explore to what extent it is possible to preserve the benefits of kV and MV imaging using a single AMFPI design, given the considerably different x-ray energy spectra used for kV and MV imaging.

IV. ORGANIZATION OF REMAINING CHAPTERS

A series of theoretical studies of hypothetical scintillator designs were performed to address the challenges detailed in the previous section. Each study is presented in one of the following chapters.

In Chapter 2, to counter the detrimental effect of beam divergence, segmented scintillators constructed so that the crystals are individually focused toward the radiation source are proposed and theoretically investigated. The study was

performed using Monte Carlo simulation of radiation transport to examine the MTF and DQE of focused segmented scintillators with thicknesses ranging from 0.5 to 6 cm. The sensitivity of such scintillators to positional displacements in different directions, which could potentially compromise their practical clinical use, was also evaluated.

In Chapter 3, a hybrid modeling technique, which involves Monte Carlo simulation of radiation transport combined with simulation of optical Swank noise and optical blur, is described. The technique facilitates accounting for both radiation and optical effects during simulation on practical computational time scales. Using the technique, the imaging performance of various hypothetical AMFPI designs based on segmented scintillators was examined in terms of contrast-to-noise ratio (CNR) and spatial resolution toward the goal of identifying designs that offer optimum performance for MV CBCT. In this study, all hypothetical designs employed BGO material with thicknesses and element-to-element pitches ranging from 0.5 to 6 cm and from 0.508 to 1.524 mm, respectively.

In Chapter 4, considerations for the design of a dual energy (kV and MV) imager are explored through examination of the performance of a variety of hypothetical AMFPI designs based on x-ray converters employing the segmented scintillator approach. In this study, all designs employed BGO material with thicknesses and element-to-element pitches ranging from 0.25 to 4 cm and from 0.508 to 1.016 mm, respectively. The performance of these designs is characterized in

terms of contrast, noise and CNR using volumetric (CBCT) imaging, as well as MTF, Swank factor and signal using projection imaging. Hybrid modeling, coupled with electronic additive noise modeling, was employed to simulate the converter and the AMFPI array.

The work presented in Chapters 2 and 3 have been adapted from two peer-reviewed articles (i.e., references 71 and 72, respectively) by the author of this dissertation. Likewise, Chapter 4 has been adapted from a manuscript recently submitted for publication.[73] Finally, the summary and conclusions for this dissertation are presented in Chapter 5.

REFERENCES – CHAPTER 1

[1] W. C. Röntgen, "On a New Kind of Rays," Science **3**, 227-231 (1896).

[2] P. M. Evans, "Anatomical imaging for radiotherapy," Phys. Med. Biol. **53**, R151-R191 (2008).

[3] F.-F. Yin, J. Wong, J. Balter, S. Benedict, J. Craig, L. Dong, D. Jaffray, S. Jiang, S. Kim and C. Ma, "The role of in-room kV X-ray imaging for patient setup and target localization," Report of AAPM Task Group **104** (2009).

[4] L. E. Antonuk, "a-Si:H TFT-based active matrix flat-panel imagers for medical x-ray applications," in *Thin Film Transistors, Materials and Processes, Volume 1: Amorphous Silicon Thin Film Transistors*, *Vol. 1,* edited by Y. Kuo (Kluwer Academic Publishers, Boston, 2004), pp. 395-484.

[5] L. E. Antonuk, J. Boudry, W. Huang, D. L. McShan, E. J. Morton, J. Yorkston, M. J. Longo and R. A. Street, "Demonstration of megavoltage and diagnostic x-ray imaging with hydrogenated amorphous silicon arrays," Med. Phys. **19**, 1455-1466 (1992).

[6] Y. El-Mohri, K.-W. Jee, L. E. Antonuk, M. Maolinbay and Q. Zhao, "Determination of the detective quantum efficiency of a prototype, megavoltage indirect detection, active matrix flat-panel imager," Med. Phys. **28**, 2538-2550 (2001); Med. Phys. **33**, 251 (2006) (Erratum).

[7] L. E. Antonuk, "Electronic portal imaging devices: a review and historical perspective of contemporary technologies and research," Phys. Med. Biol. **47**, R31-R65 (2002).

[8] J. Pouliot, A. Bani-Hashemi, J. Chen, M. Svatos, F. Ghelmansarai, M. Mitschke, M. Aubin, P. Xia, O. Morin, K. Bucci, M. Roach 3rd, P. Hernandez, Z. Zheng, D. Hristov and L. Verhey, "Low-dose megavoltage cone-beam CT for radiation therapy," Int. J. Radiat. Oncol., Biol., Phys. **61**, 552-560 (2005).

[9] B. Wowk and S. Shalev, "Thick phosphor screens for on-line portal imaging," Med. Phys. **21**, 1269-1276 (1994).

[10] J.-P. Bissonnette, I. A. Cunningham and P. Munro, "Optimal phosphor thickness for portal imaging," Med. Phys. **24**, 803-814 (1997).

[11] R. K. Swank, "Absorption and noise in x-ray phosphors," J. Appl. Phys. **44**, 4199-4203 (1973).

[12] L. E. Antonuk, K.-W. Jee, Y. El-Mohri, M. Maolinbay, S. Nassif, X. Rong, Q. Zhao, J. H. Siewerdsen, R. A. Street and K. S. Shah, "Strategies to improve the signal and noise performance of active matrix, flat-panel imagers for diagnostic x-ray applications," Med. Phys. **27**, 289-306 (2000).

[13] P. R. Granfors, R. Aufrichtig, G. E. Possin, B. W. Giambattista, Z. S. Huang, J. Liu and B. Ma, "Performance of a 41×41 cm2 amorphous silicon flat panel x-ray detector designed for angiographic and R&F imaging applications," Med. Phys. **30**, 2715-2726 (2003).

[14] Y. El-Mohri, L. E. Antonuk, Q. Zhao, Y. Wang, Y. Li, H. Du and A. Sawant, "Performance of a high fill factor, indirect detection prototype flat-panel imager for mammography," Med. Phys. **34**, 315-327 (2007).

[15] N. W. Marshall, A. Mackenzie and I. E. Honey, "Quality control measurements for digital x-ray detectors," Phys. Med. Biol. **56**, 979-999 (2011).
[16] D. A. Jaffray, J. H. Siewerdsen, J. W. Wong and A. A. Martinez, "Flat-panel cone-beam computed tomography for image-guided radiation therapy," International Journal of Radiation Oncology*Biology*Physics **53**, 1337-1349 (2002).
[17] J. H. Siewerdsen and D. A. Jaffray, "Cone-beam computed tomography with a flat-panel imager: Magnitude and effects of x-ray scatter," Med. Phys. **28**, 220-231 (2001).
[18] D. A. Jaffray and J. H. Siewerdsen, "Cone-beam computed tomography with a flat-panel imager: Initial performance characterization," Med. Phys. **27**, 1311-1323 (2000).
[19] O. Morin, A. Gillis, J. Chen, M. Aubin, M. K. Bucci, M. Roach, III and J. Pouliot, "Megavoltage cone-beam CT: system description and clinical applications," Med. Dos. **31**, 51-61 (2006).
[20] M. Aubin, O. Morin, J. Chen, A. Gillis, B. Pickett, J. F. Aubry, C. Akazawa, J. Speight, M. Roach III and J. Pouliot, "The use of megavoltage cone-beam CT to complement CT for target definition in pelvic radiotherapy in the presence of hip replacement," Brit J Radiol **79**, 918-921 (2006).
[21] H. Guan, F. F. Yin and J. H. Kim, "Accuracy of inhomogeneity correction in photon radiotherapy from CT scans with different settings," Phys. Med. Biol. **47**, N223-N231 (2002).
[22] K. M. Langen, S. L. Meeks, D. O. Poole, T. H. Wagner, T. R. Willoughby, P. A. Kupelian, K. J. Ruchala, J. Haimerl and G. H. Olivera, "The use of megavoltage CT (MVCT) images for dose recomputations," Phys. Med. Biol. **50**, 4259-4276 (2005).
[23] O. Morin, J. Chen, M. Aubin, A. Gillis, J.-F. Aubry, S. Bose, H. Chen, M. Descovich, P. Xia and J. Pouliot, "Dose calculation using megavoltage cone-beam CT," Int. J. Radiat. Oncol. Biol. Phys. **67**, 1201-1210 (2007).
[24] N. Mail, D. Moseley, J. Siewerdsen and D. Jaffray, "The influence of bowtie filtration on cone-beam CT image quality," Med. Phys. **36**, 22-32 (2009).
[25] R. E. Colbeth, I. P. Mollov, P. G. Roos and E. G. Shapiro, "Flat panel CT detectors for sub-second volumetric scanning," in *Medical Imaging 2005,* (International Society for Optics and Photonics, 2005), pp. 387-398.
[26] G. Rose, J. Wiegert, D. Schaefer, K. Fiedler, N. Conrads, J. Timmer, V. Rasche, N. Noordhoek, E. Klotz and R. Koppe, "Image quality of flat-panel cone beam CT," Medical Imaging 2003, 677-683 (2003).
[27] B. A. Groh, J. H. Siewerdsen, D. G. Drake, J. W. Wong and D. A. Jaffray, "A performance comparison of flat-panel imager-based MV and kV cone-beam CT," Med. Phys. **29**, 967-975 (2002).
[28] E. C. Ford, J. Chang, K. Mueller, K. Sidhu, D. Todor, G. Mageras, E. Yorke, C. C. Ling and H. Amols, "Cone-beam CT with megavoltage beams and an amorphous silicon electronic portal imaging device: Potential for verification of radiotherapy of lung cancer," Med. Phys. **29**, 2913-2924 (2002).

[29] O. Gayou, D. S. Parda, M. Johnson and M. Miften, "Patient dose and image quality from mega-voltage cone beam computed tomography imaging," Med. Phys. **34**, 499-506 (2007).
[30] M. A. Mosleh-Shirazi, P. M. Evans, W. Swindell, J. R. N. Symonds-Tayler, S. Webb and M. Partridge, "Rapid portal imaging with a high-efficiency, large field-of-view detector," Med. Phys. **25**, 2333-2346 (1998).
[31] E. J. Seppi, P. Munro, S. W. Johnsen, E. G. Shapiro, C. Tognina, D. Jones, J. M. Pavkovich, C. Webb, I. Mollov, L. D. Partain and R. E. Colbeth, "Megavoltage Cone-Beam Computed Tomography Using a High-Efficiency Image Receptor," Int. J. Rad. Onc. Biol. Phys. **55**, 793-803 (2003).
[32] A. Sawant, L. E. Antonuk, Y. El-Mohri, Y. Li, Z. Su, Y. Wang, J. Yamamoto, Q. Zhao, H. Du, J. Daniel and R. A. Street, "Segmented phosphors: MEMS-based high quantum efficiency detectors for megavoltage x-ray imaging," Med. Phys. **32**, 553-565 (2005).
[33] J. Maltz, A. Dubouloz, A. Paidi, B. Gangadharan, J. Hartmann, A. Bani-Hashemi and G. Hoerauf, "Thick monolithic pixelated scintillator array for megavoltage imaging - Conference Abstract," Med. Phys. **36**, 2818-2819 (2009).
[34] H. Keller, M. Glass, R. Hinderer, K. Ruchala, R. Jeraj, G. Olivera and T. R. Mackie, "Monte Carlo Study of a Highly Efficient Gas Ionization Detector for Megavoltage Imaging and Image-Guided Radiotherapy," Med. Phys. **29**, 165-175 (2002).
[35] S. Rathee, D. Tu, T. T. Monajemi, D. W. Rickey and B. G. Fallone, "A bench-top megavoltage fan-beam CT using CdWO4-photodiode detectors. I. System description and detector characterization," Med. Phys. **33**, 1078-1089 (2006).
[36] S. S. Samant and A. Gopal, "Analysis of the kinestatic charge detection system as a high detective quantum efficiency electronic portal imaging device," Med. Phys. **33**, 3557-3567 (2006).
[37] P. F. Kirvan, T. T. Monajemi, B. G. Fallone and S. Rathee, "Performance characterization of a MVCT scanner using multislice thick, segmented cadmium tungstate-photodode detectors," Med. Phys. **37**, 249-257 (2010).
[38] E. J. Morton, W. Swindell, D. G. Lewis and P. M. Evans, "A linear array, scintillation crystal-photodiode detector for megavoltage imaging," Med. Phys. **18**, 681-691 (1991).
[39] A. Sawant, L. E. Antonuk, Y. El-Mohri, Q. Zhao, Y. Li, Z. Su, Y. Wang, J. Yamamoto, H. Du, I. Cunningham, M. Klugerman and K. Shah, "Segmented crystalline scintillators: an initial investigation of high quantum efficiency detectors for megavoltage x-ray imaging," Med. Phys. **32**, 3067-3083 (2005).
[40] A. Sawant, L. E. Antonuk, Y. El-Mohri, Q. Zhao, Y. Wang, Y. Li, H. Du and L. Perna, "Segmented crystalline scintillators: Empirical and theoretical investigation of a high quantum efficiency EPID based on an initial engineering prototype CsI(Tl) detector," Med. Phys. **33**, 1053-1066 (2006).
[41] Y. Wang, L. E. Antonuk, Y. El-Mohri, Q. Zhao, A. Sawant and H. Du, "Monte Carlo investigations of megavoltage cone-beam CT using thick,

segmented scintillating detectors for soft tissue visualization," Med. Phys. **35**, 145-158 (2008).
[42] Y. Wang, L. E. Antonuk, Y. El-Mohri and Q. Zhao, "A Monte Carlo investigation of Swank noise for thick, segmented, crystalline scintillators for radiotherapy imaging," Med. Phys. **36**, 3227-3238 (2009).
[43] Y. Wang, L. E. Antonuk, Q. Zhao, Y. El-Mohri and L. Perna, "High-DQE EPIDs based on thick, segmented BGO and CsI:Tl scintillators: Performance evaluation at extremely low dose," Med. Phys. **36**, 5707-5718 (2009).
[44] Y. El-Mohri, L. E. Antonuk, Q. Zhao, R. B. Choroszucha, H. Jiang and L. Liu, "Low-dose megavoltage cone-beam CT imaging using thick, segmented scintillators," Phys. Med. Biol. **56**, 1509-1527 (2011).
[45] T. T. Monajemi, S. Steciw, B. G. Fallone and S. Rathee, "Modeling scintillator-photodiodes as detectors for megavoltage CT," Med. Phys. **31**, 1225-1234 (2004).
[46] P. M. Evans, M. A. Mosleh-Shirazi, E. J. Harris and J. Seco, "Monte Carlo and Lambertian light guide models of the light output from scintillation crystals at megavoltage energies," Med. Phys. **33**, 1797-1809 (2006).
[47] Y. Wang, Y. El-Mohri, L. E. Antonuk and Q. Zhao, "Monte Carlo investigations of the effect of beam divergence on thick, segmented crystalline scintillators for radiotherapy imaging," Phys. Med. Biol. **55**, 3659-3673 (2010).
[48] T. T. Monajemi, B. G. Fallone and S. Rathee, "Thick, segmented CdWO4-photodiode detector for cone beam megavoltage CT: A Monte Carlo study of system design parameters," Med. Phys. **33**, 4567-4577 (2006).
[49] W. Que and J. A. Rowlands, "X-ray imaging using amorphous selenium: Inherent spatial resolution," Med. Phys. **22**, 365-374 (1995).
[50] G. Hajdok and I. A. Cunningham, "Penalty on the detective quantum efficiency from off-axis incident x rays," in *Medical Imaging 2004*, *Vol. 5368,* (International Society for Optics and Photonics, 2004), pp. 109-118.
[51] G. F. Knoll, *Radiation Detection and Measurement*. (John Wiley & Sons, Hoboken, NJ, 2010).
[52] Y. El-Mohri, L. E. Antonuk, R. B. Choroszucha, Q. Zhao, H. Jiang and L. Liu, "Optimization of the performance of segmented scintillators for radiotherapy imaging through novel binning techniques," Phys. Med. Biol. **59**, 797 (2014).
[53] M. Weissbluth, C. Karzmark, R. Steele and A. Selby, "The Stanford Medical Linear Accelerator: II. Installation and Physical Measurements 1," Radiology **72**, 242-265 (1959).
[54] H. Johns and J. Cunningham, "A precision cobalt 60 unit for fixed field and rotation therapy," Am. J. Roentgenol. Radium Therapy Nuclear Med. **81**, 4-12 (1959).
[55] Y. Cho and P. Munro, "Kilovision: thermal modeling of a kilovoltage x-ray source integrated into a medical linear accelerator," Med. Phys. **29**, 2101-2108 (2002).
[56] D. M. Galbraith, "Low-energy imaging with high-energy bremsstrahlung beams," Med. Phys. **16**, 734-746 (1989).

[57] A. Tsechanski, A. F. Bielajew, S. Faermann and Y. Krutman, "A thin target approach for portal imaging in medical accelerators," Phys. Med. Biol. **43**, 2221-2236 (1998).
[58] O. Ostapiak, P. O'Brien and B. Faddegon, "Megavoltage imaging with low Z targets: Implementation and characterization of an investigational system," Med. Phys. **25**, 1910-1918 (1998).
[59] S. Flampouri, P. Evans, F. Verhaegen, A. Nahum, E. Spezi and M. Partridge, "Optimization of accelerator target and detector for portal imaging using Monte Carlo simulation and experiment," Phys. Med. Biol. **47**, 3331-3349 (2002).
[60] J. Robar, "Generation and modelling of megavoltage photon beams for contrast-enhanced radiation therapy," Phys. Med. Biol. **51**, 5487-5504 (2006).
[61] B. A. Faddegon, V. Wu, J. Pouliot, B. Gangadharan and A. Bani-Hashemi, "Low dose megavoltage cone beam computed tomography with an unflattened 4 MV beam from a carbon target," Med. Phys. **35**, 5777-5786 (2008).
[62] J. L. Robar, T. Connell, W. Huang and R. G. Kelly, "Megavoltage planar and cone-beam imaging with low-Z targets: Dependence of image quality improvement on beam energy and patient separation," Med. Phys. **36**, 3955-3963 (2009).
[63] R. T. Flynn, J. Hartmann, A. Bani-Hashemi, E. Nixon, R. Alfredo, C. Siochi, E. C. Pennington and J. E. Bayouth, "Dosimetric characterization and application of an imaging beam line with a carbon electron target for megavoltage cone beam computed tomography," Med. Phys. **36**, 2181-2192 (2009).
[64] B. A. Faddegon, M. Aubin, A. Bani-Hashemi, B. Gangadharan, A. R. Gottschalk, O. Morin, D. Sawkey, V. Wu and S. S. Yom, "Comparison of patient megavoltage cone beam CT images acquired with an unflattened beam from a carbon target and a flattened treatment beam," Med. Phys. **37**, 1737-1741 (2010).
[65] T. Connell and J. L. Robar, "Low-Z target optimization for spatial resolution improvement in megavoltage imaging," Med. Phys. **37**, 124-131 (2010).
[66] D. Roberts, V. Hansen, M. Thompson, G. Poludniowski, A. Niven, J. Seco and P. Evans, "Kilovoltage energy imaging with a radiotherapy linac with a continuously variable energy range," Med. Phys. **39**, 1218-1226 (2012).
[67] D. Parsons, J. L. Robar and D. Sawkey, "A Monte Carlo investigation of low-Z target image quality generated in a linear accelerator using Varian's VirtuaLinac," Med. Phys. **41**, 021719 (2014).
[68] J. Rottmann, M. Aristophanous, A. Chen, L. Court and R. Berbeco, "A multi-region algorithm for markerless beam's-eye view lung tumor tracking," Phys. Med. Biol. **55**, 5585-5598 (2010).
[69] F.-F. Yin, H. Guan and W. Lu, "A technique for on-board CT reconstruction using both kilovoltage and megavoltage beam projections for 3D treatment verification," Med. Phys. **32**, 2819-2826 (2005).

[70] J. Zhang and F. F. Yin, "Minimizing image noise in on-board CT reconstruction using both kilovoltage and megavoltage beam projections," Med. Phys. **34**, 3665-3673 (2007).
[71] L. Liu, L. E. Antonuk, Q. Zhao, Y. El-Mohri and H. Jiang, "Countering beam divergence effects with focused segmented scintillators for high DQE megavoltage active matrix imagers," Phys. Med. Biol. **57**, 5343-5358 (2012).
[72] L. Liu, L. E. Antonuk, Y. El-Mohri, Q. Zhao and H. Jiang, "Optimization of the design of thick, segmented scintillators for megavoltage cone-beam CT using a novel, hybrid modeling technique," Med. Phys. **41**, 061916 (2014).
[73] L. Liu, L. E. Antonuk, Y. El-Mohri, Q. Zhao and H. Jiang, "Theoretical investigation of the design and performance of a dual energy (kV and MV) radiotherapy imager," submitted to Medical Physics (2015).

CHAPTER 2

COUNTERING BEAM DIVERGENCE EFFECTS WITH FOCUSED SEGMENTED SCINTILLATORS

I. INTRODUCTION

Although segmented scintillators have demonstrated encouraging performance in earlier investigations, those with thicknesses greater than ~1 cm are susceptible to the detrimental effect of beam divergence, resulting in MTF and DQE degradation.[1] As illustrated in Figs. 2.1(a) and 2.1(b), this effect becomes increasingly pronounced at locations progressively farther from the central beam axis, as well as for progressively thicker scintillators.

In order to counter the performance degrading effect of beam divergence, the individual elements (both the scintillating crystals as well as the septal walls) should be constructed so as to be focused toward the radiation source. Illustrations of two different geometric approaches that satisfy this requirement are shown in Figs. 2.1(c) and 2.1(d).

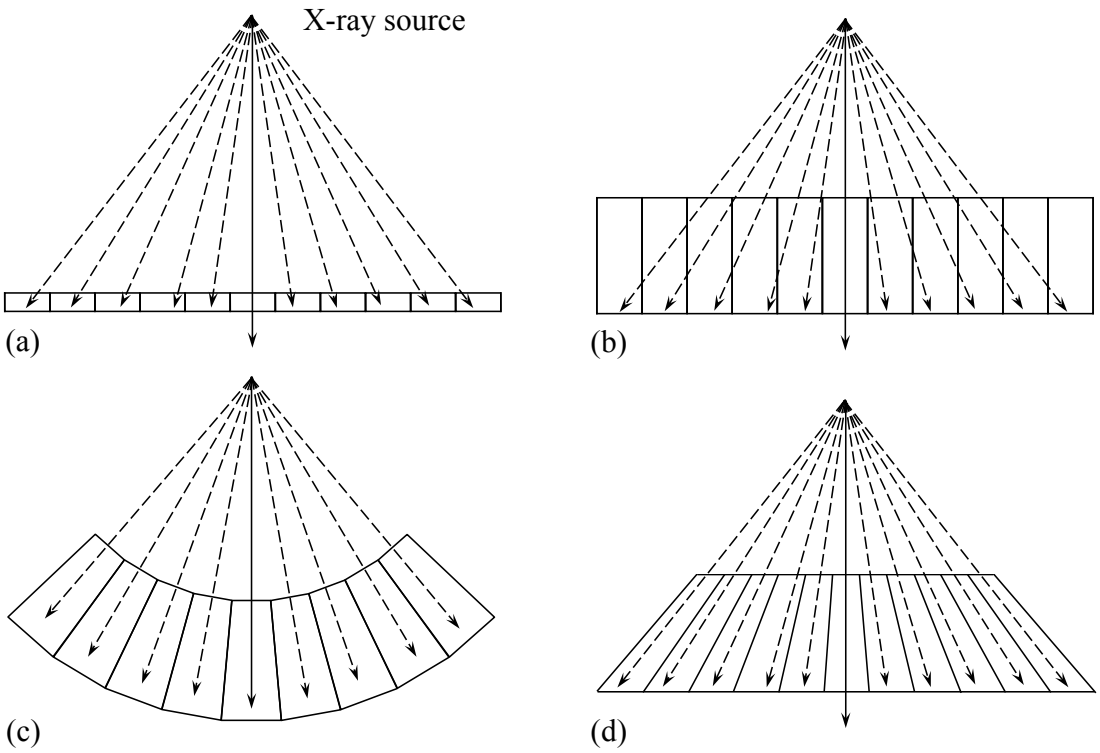

Figure 2.1. (a, b) Schematic illustration (not to scale) of the problematic effect of geometric beam divergence. X rays following a given track (black dashed arrows) away from the central beam axis (black solid arrows) can deposit energy in different neighboring scintillating crystals, leading to loss of spatial resolution — an effect that becomes more pronounced with increasing scintillator thickness, as illustrated in (a) and (b). Schematic cross-sectional view of two geometric approaches for addressing beam divergence: (c) a curved, focused scintillator geometry; and (d) a planar, focused scintillator geometry. Note that, for purposes of clarity of illustration, the metal plate typically positioned over the scintillator is not shown in this or in following figures in this chapter.

Figure 2.1(c) illustrates the conceptually simple approach of employing a curved geometry in which the top and bottom surfaces of the scintillator have the shape of concentric spherical caps with a common virtual center located at the position of the radiation source. In one embodiment of this geometry, every crystal has the same shape and is focused toward, and positioned at the same distance from, the radiation source. The use of a single crystal shape across such a curved geometry

offers the possible advantage of relatively straightforward crystal fabrication. Two possible arrangements of the crystals for such an embodiment, each employing a different crystal shape, are illustrated in Figs. 2.2(a) and 2.2(b). In Fig. 2.2(a), a warped rectangular arrangement in which the crystals are positioned along two sets of perpendicularly intersecting longitudinal lines on the spherical cap is shown. (Note that the crystals are truncated in the peripheral region.) In Fig. 2.2(b), a concentric ring arrangement in which the crystals are positioned along a series of latitudinal lines with equal angular separation is shown. Both designs provide a scintillating crystal occupancy (which shall be referred to as *fill factor*) of less than 100%, since it is impossible to tessellate a spherical cap with thousands of crystals of the same single shape.[2] More importantly, the designs in Figs. 2.2(a) and 2.2(b) have a variable element-to-element pitch (defined as the distance between the center of two adjacent elements), which would significantly complicate registration between the elements and the pixels in an underlying imaging array. In addition, the spherical bottom surface of such scintillators favors the use of an imaging array having the same curved shape – precluding the use of existing flat panel array technology which employs rigid substrates.[3, 4] While a prototype active matrix imaging array fabricated on a flexible substrate and configured into an approximately hemispherical shape has been demonstrated,[5] the development of such imaging arrays is only in its infancy, and the registration of scintillators consisting of thousands of crystals with such curved arrays would present formidable challenges.

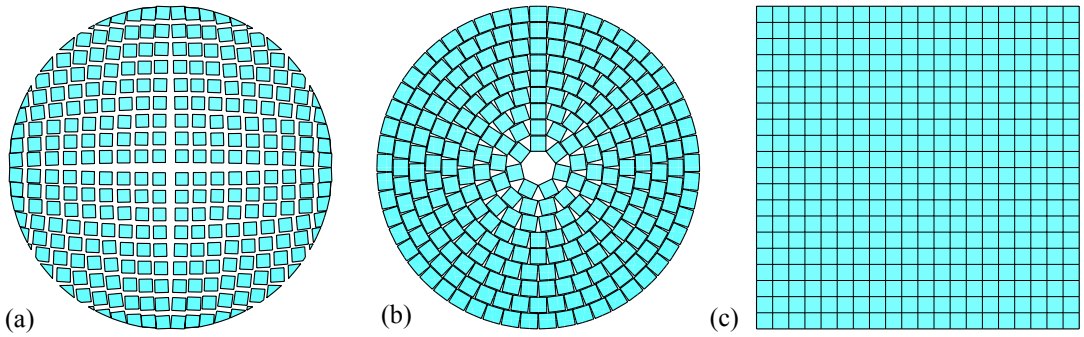

Figure 2.2. Top views of two possible arrangements of individual scintillating crystals on a spherical cap: (a) a warped rectangular arrangement and (b) a concentric ring arrangement – both of which correspond to the curved, focused geometry of Fig. 2.1(c). (c) Top view of a rectilinear grid arrangement of individual scintillating crystals in the absence of septal wall material – corresponding to the planar, focused geometry of Fig. 2.1(d).

An alternative to the spherical cap approach, involving a planar geometry, is shown in Fig. 2.1(d) in which both the top and bottom surfaces of the scintillator are flat and parallel to each other. The methods required to fabricate specific designs of such focused planar geometries are expected to require adjustment to the techniques [6] presently used to construct unfocused segmented prototypes. However, the rectilinear grid arrangement of scintillating crystals illustrated in Fig. 2.2(c) provides a fill factor higher than those of curved designs in the presence of septal walls of the same minimum width – as discussed in Appendix A. Moreover, this geometry offers the considerable advantage of a fixed element-to-element pitch. The flat bottom surface and the fixed pitch of scintillator designs based on this approach would facilitate straightforward registration with existing AMFPI arrays. Overall, given the probable practical advantages in creating MV AMFPIs employing converters based on the focused, planar, segmented scintillator approach, a study concentrating on the

theoretical performance of such converters was performed, the results of which are reported below.

II. METHODS

II.A. Monte Carlo simulations

The MTF, noise power spectrum (NPS) and DQE performance of a variety of hypothetical MV x-ray converter designs incorporating segmented scintillators were examined through Monte Carlo simulation of radiation transport. Optical transport of photons generated in the scintillators was not included in this study due to the fact that beam divergence is expected to be primarily determined by radiation transport. The simulations were performed using the EGSnrc code, a package widely employed for medical physics applications.[7] Simulations were performed on a variety of focused and unfocused designs. In the simulations, the geometric shapes of the designs were modeled using the EGSnrc C++ class library (egspp).[8] The user code, as well as the geometry configuration input file, were modified, as necessary, to facilitate the present studies.

The simulations employed a point x-ray source with a 6 MV spectrum obtained through interpolation of a tabulated file corresponding to the energy spectrum of a Varian LINAC.[9] Cutoff energies for photons and electrons were set to 0.01 and 0.521 MeV, respectively – both corresponding to a kinetic energy of 10 keV. Other simulation parameters were set to the values used in a previous segmented scintillator study.[1] Using a 64-bit Linux CPU cluster with ~100, 1.8 GHz AMD

Opteron processors, a total of ~142,000 CPU hours were required to perform the simulations.

II.B. Overview of converter designs

For the hypothetical converters investigated in this study, segmented scintillator thicknesses, T_{sci}, of 0.5, 1, 2, 4 and 6 cm, coupled to an overlying 1 mm thick copper plate, were simulated. In an earlier theoretical study of the effects of beam divergence on unfocused segmented scintillators,[1] incoming radiation was modeled as a parallel rectangular beam tilted at different incident angles to quantify those effects in unfocused converter designs. In the present study, a point radiation source is employed to more accurately model the physical situation. Use of even more realistic extended sources was found to result in negligible (i.e., less than 1%) changes to MTF for both unfocused and focused converters compared to a point source. In addition, both focused and unfocused converter designs were examined – to investigate the effectiveness of focused designs in addressing the imaging performance degradation due to beam divergence. Conceptually, as illustrated in Fig. 2.3, the converters were considered to have a 40×40 cm^2 detection area, centered at the central beam axis of the radiation field and situated at a source to detector distance (SDD) of 130 cm, reflecting the approximate size and positioning of typical clinical MV AMFPIs. In order to evaluate the performance of the converters for increasingly oblique incident angles, selected regions of the converter located progressively further away (i.e., at distances of 0, 5, 10, 15, and 20 cm) from the

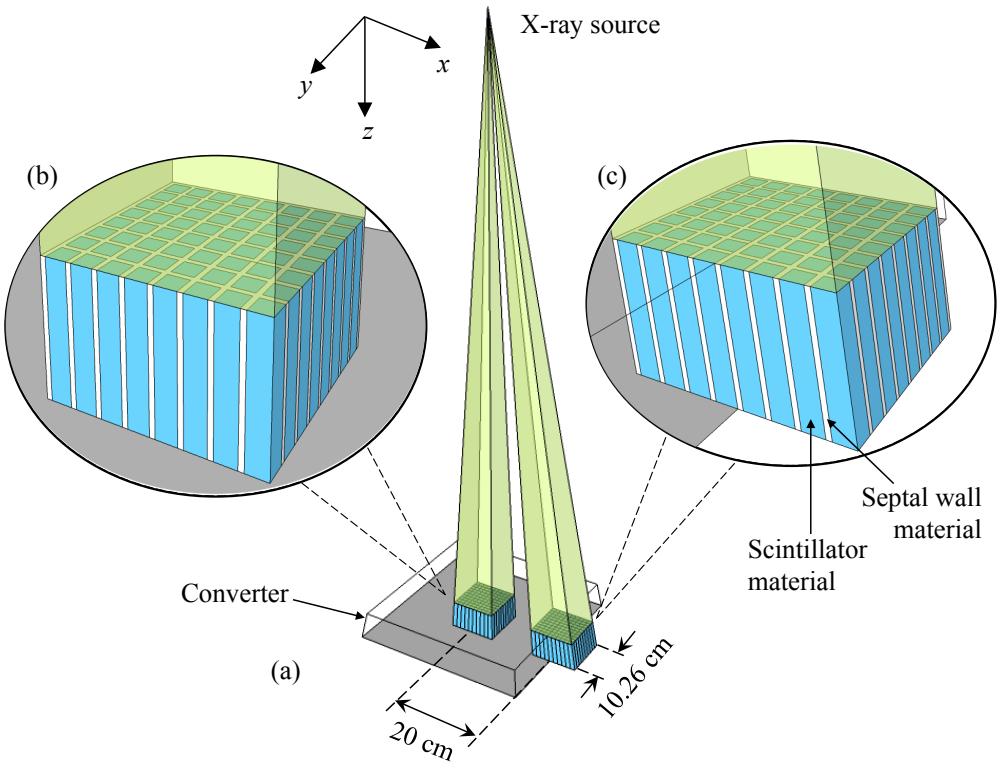

Figure 2.3. (a) Schematic illustration of the geometric setup employed in the radiation transport simulations. The converter (depicted as a transparent wire frame with a gray bottom surface) incorporates a thick, focused, segmented scintillator design. Two simulated regions, each consisting of a sub-matrix of scintillator elements (with blue and white areas corresponding to scintillator and septal wall material, respectively), are portrayed at the central beam axis and 20 cm off-axis at the periphery of the converter. As illustrated in magnified insets (b) and (c) corresponding to these regions, those scintillator elements located toward the periphery of the converter are more obliquely shaped. Note that the sub-matrix shown in (c) extends beyond the edge of the converter, so as to facilitate evaluation of imaging performance near the periphery. The transparent green volumes delineate the space traversed by X rays that are emitted from the source and reach the top surface of each selected region.

central beam axis were modeled. Each of these simulated regions consists of a sub-matrix of 101×101 scintillator elements (corresponding to an area of 10.26×10.26 cm^2 at the bottom surface of the scintillator) centered at the designated location. This area is sufficiently large to allow accurate local determination of frequency dependent

metrics, while small enough to allow the simulations to be performed within manageable times. For example, the NPS simulation for a single region required between ~120 and 2,700 CPU hours (corresponding to elapsed run times of ~1.2 to 27 hours), depending upon the design of the converter.

For the focused designs, each element is a square frustum (i.e., a truncated pyramid) with the virtual apex located at the point radiation source. Within a given quadrant of the converter, the shape of every frustum is different in order to accommodate the changing obliqueness of the incident radiation. However, the square bottom bases of all the individual frusta are geometrically identical, resulting in uniform pitch at the bottom surface of the segmented scintillator. This pitch was chosen to be 1.016 mm (with 0.1 mm polystyrene septal walls and 0.916 mm scintillator crystals) in both orthogonal directions — corresponding to the dimensions and wall composition of several prototypes previously reported by our group.[6] Since the shapes of the top and bottom bases are geometrically similar, the pitch at the top surface of the scintillator is also uniform, and is reduced by a factor of φ compared to that at the bottom surface, where:

$$\varphi = \frac{SDD}{SDD + T_{sci}}. \tag{2.1}$$

It is interesting to note that, for a focused converter of a given thickness and element pitch, the ability of elements to detect incident X rays varies slowly as a function of position across the converter. While the volume of the elements, as well as the fill factor of the elements (i.e., the fraction of element volume occupied by

scintillator material), remain constant throughout the converter (see Appendix B), the efficiency of detection of incident X rays (i.e., the x-ray QE) increases for elements more distant from the center of the converter as a result of the increasing radiation path-length for those elements. As a result, elements located on the periphery of a 40×40 cm^2 converter are ~0.9% to 0.3% more efficient in detecting incident radiation compared to elements near the center of the converter for thicknesses ranging from 0.5 to 6 cm.

In the simulations, four candidate scintillator materials (CsI:Tl, BGO [$Bi_4Ge_3O_{12}$], LYSO [$Lu_{1.8}Y_{0.2}SiO_4$:Ce] and $CdWO_4$) were examined. These materials were selected on the basis of their desirable properties which include high physical and electron densities, high optical output, high refractive index, and short decay time, as summarized in Table 2.1. For each of the CsI:Tl and BGO materials, a total of 10 converter designs (corresponding to 5 scintillator thicknesses for each of the focused

Table 2.1. Physical properties [10, 11] of the various scintillator materials examined in this study. Note that the decay times listed for CsI:Tl and $CdWO_4$ consist of two components with corresponding weightings indicated in the brackets.

Material	Light output (photons/MeV)	Refractive index	Decay time (μs)	Physical density (g/cm^3)	Electron density (mol/cm^3)
CsI:Tl	64,800	1.79	0.68 (64%), 3.34 (36%)	4.51	1.87
BGO	8,000	2.15	0.3	7.13	3.00
LYSO	32,000	1.81	0.04	7.10	3.04
$CdWO_4$	15,000	2.3	1.1 (40%), 14.5 (60%)	7.9	3.38

and unfocused geometries) were modeled, while fewer designs were modeled for LYSO and $CdWO_4$.

II.C. Determination of MTF

As shown in Fig. 2.4(a), each MTF (and NPS) simulation was performed on a portion of the converter located at a distance d_x from the central beam axis. MTF was determined by calculating the one-dimensional Fourier transform of a line spread function (LSF) obtained using the angled slit technique.[12, 13] In the simulations, the slit was modeled as a 10.26 cm × 4 μm area, defining an aperture for the incident

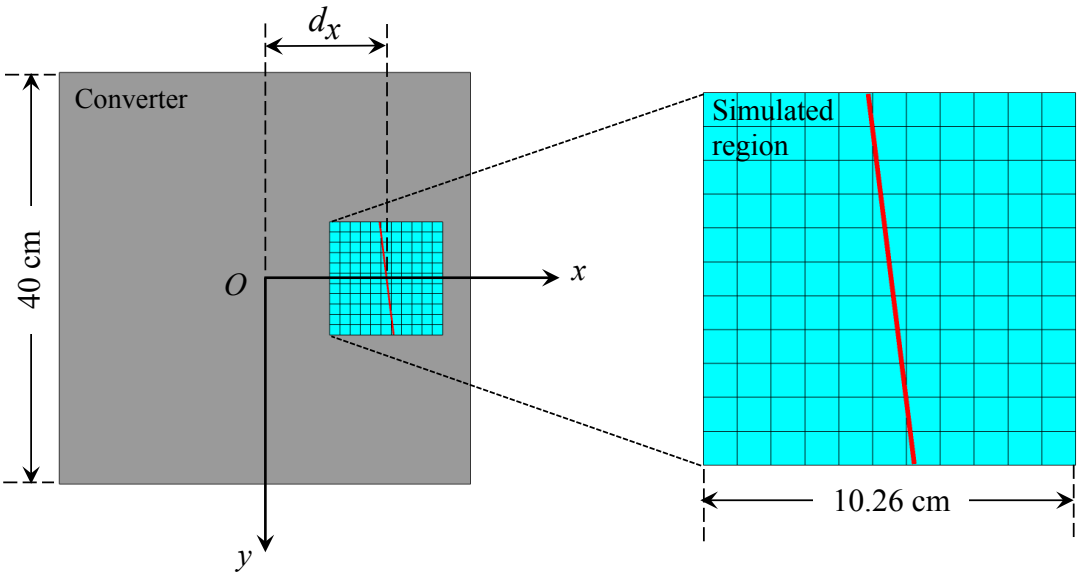

Figure 2.4. (a) Schematic illustration of the simulation geometry used in the determination of MTF and NPS. The blue area represents a simulated region of the converter (indicated in gray). For the case of the MTF simulations, the red line corresponds to the slit area which forms a 2° angle with respect to the *y*-axis. In the present study, simulations were performed at various regions located at distances, d_x, ranging from 0 to 20 cm from the central beam axis, *O*. (b) A magnified view of the simulated portion of the converter.

X rays. The longer dimension of this area was positioned at a 2° tilt angle relative to the y-axis, as schematically illustrated in Fig. 2.4(b). Energy deposited in each scintillating crystal within the region of interest was plotted as a function of the distance between the center of the elements and the tilted slit, resulting in the LSF. For each simulated region of each converter design, 4×10^5 primary x-ray histories were employed – a number sufficient to keep statistical errors below 0.9%.

II.D. Determination of Normalized NPS (NNPS) and DQE

NPS was obtained from the Fourier transform of zero-mean data realizations, using the synthesized slit technique.[14-16] For each simulated region of each converter design, a total of 400 simulations were performed with 10 million primary x-ray histories per simulation, resulting in 400 frames. For each frame, only the central 81×81 elements (leaving a 10 element wide margin on each side) were used and summed along one direction, providing a realization with 81 points. For each realization, the average of the 81 points was subtracted from the value for each point, generating a zero-mean realization, upon which a one-dimensional Fourier transform was performed. NPS was obtained by averaging the 400 Fourier transforms obtained from the 400 frames, and normalized NPS (NNPS) was then determined from the equation [1]

$$NNPS(f) = \frac{\bar{q}_0 NPS(f)}{\bar{A}^2}, \tag{2.2}$$

where $\bar{q}_0$ is the incident x-ray fluence, and $\bar{A}$ is the average energy deposited in each scintillating crystal. Finally, DQE was calculated from the simulation results for MTF and NNPS using the equation [17]

$$DQE(f) = \frac{MTF^2(f)}{NNPS(f)}, \tag{2.3}$$

III. RESULTS

III.A. MTF

Simulation results for MTF performance for converter designs incorporating segmented BGO scintillators with thicknesses ranging from 0.5 to 6 cm are shown in Fig. 2.5. For unfocused converters, MTF determined at the central beam axis (where beam divergence effects are negligible) degrades with increasing thickness, as seen in Fig. 2.5(a). For example, at a spatial frequency of 0.49 mm^{-1} (corresponding to the Nyquist frequency associated with the 1.016 mm pitch of the elements), MTF drops from ~0.4 to ~0.3. This degradation of spatial resolution for thicker scintillators is mainly due to the increasing lateral spread of energy deposited by Compton electrons, as well as the higher probability of re-absorption of recoil Compton X rays. For regions located further away from the central beam axis, beam divergence effects become progressively more pronounced for thicker, unfocused scintillators, as illustrated in Fig. 2.5(b) which shows results corresponding to 20 cm off-axis. (Note that the first minimum in the results for thicker scintillators appears at increasingly lower frequencies, which correspond closely to the lateral displacement created by the projection of the possible points of interaction across the thickness of the scintillator.[1]) At 0.49 mm^{-1}, the MTF results for the 0.5 cm thickness exhibits only a

slight degradation from 0.4 at the central beam axis to ~0.3 at 20 cm off-axis. By comparison, the MTF results for the 6 cm thickness decrease dramatically from ~0.3 at the central beam axis to less than 0.05 at 20 cm off-axis. Such a significant drop in

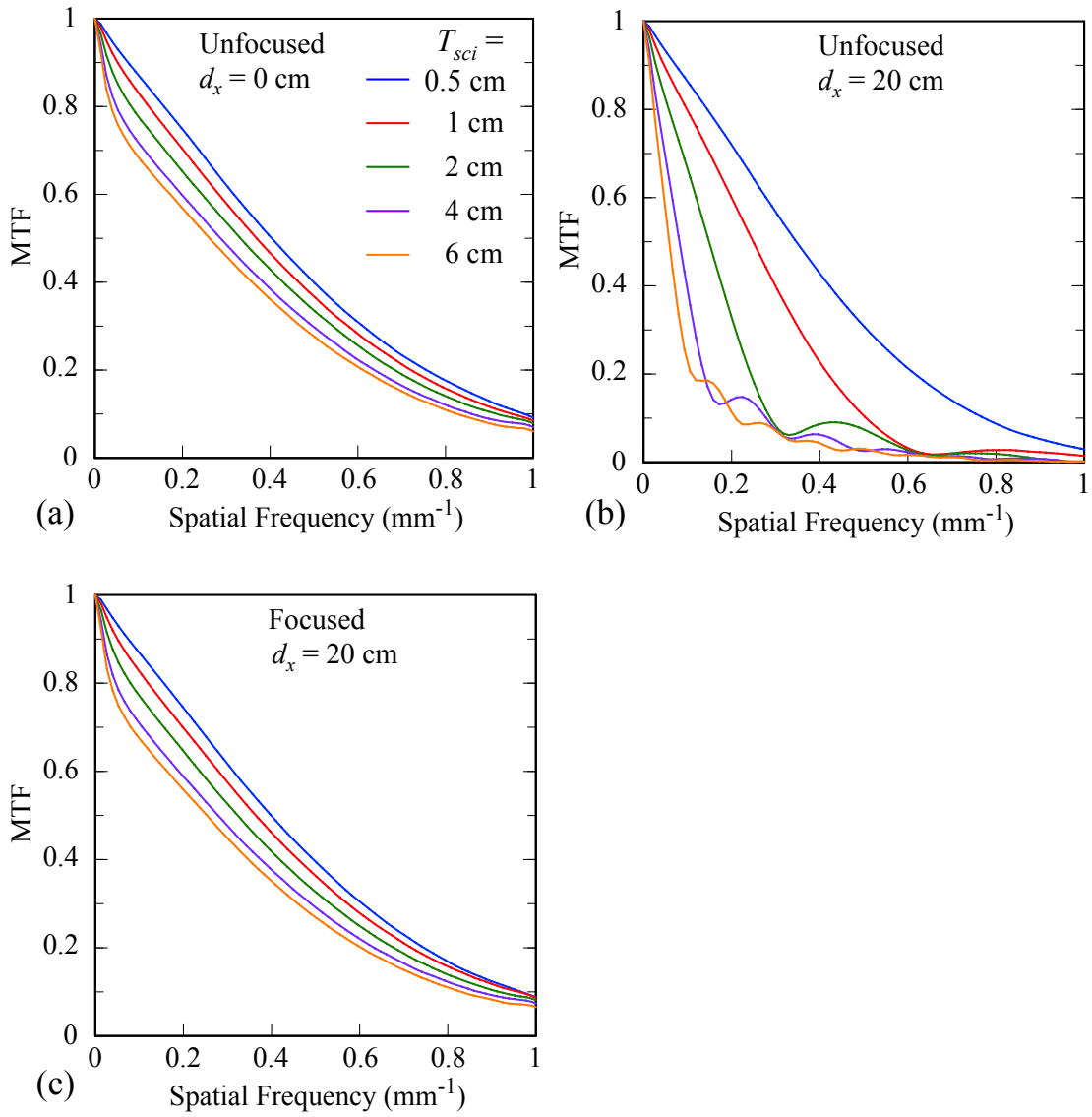

Figure 2.5. MTF results for converters incorporating segmented BGO scintillators with thicknesses, T_{sci}, ranging from 0.5 to 6 cm for: (a) unfocused designs at a location corresponding to the central beam axis, (b) unfocused designs at 20 cm off-axis, and (c) focused designs at 20 cm off-axis.

MTF largely nullifies the advantage of greater attenuation provided by thicker segmented scintillators. However, as demonstrated in Fig. 2.5(c), for converter designs incorporating focused segmented scintillators, MTF values 20 cm off-axis are restored to levels very close to (i.e., within 0.01) the central beam axis values shown in Fig. 2.5(a).

MTF results for converters incorporating unfocused and focused 6 cm thick BGO segmented scintillators at various locations away from the central beam axis are shown in Fig. 2.6. For the unfocused converter, MTF decreases at locations increasingly farther from the central beam axis, as shown in Fig. 2.6(a). Such variation of MTF would result in blurrier images in regions further away from the central axis. For the focused converter, the MTF is observed to be nearly independent

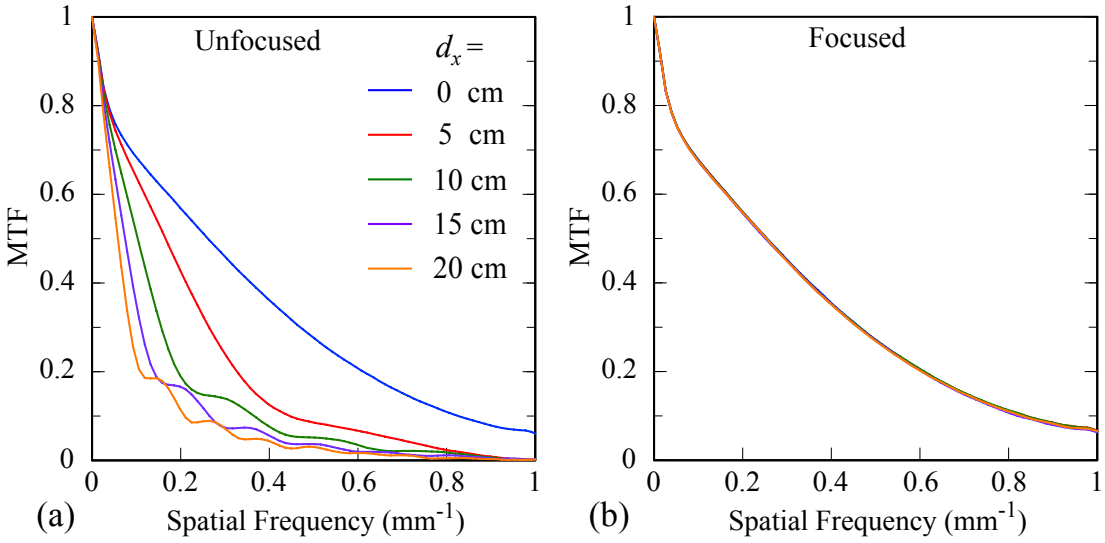

Figure 2.6. MTF results for converters incorporating 6 cm thick BGO scintillators at locations, d_x, ranging from 0 to 20 cm away from the central beam axis for (a) unfocused and (b) focused designs.

of location, as is evident by the almost completely overlapping curves in Fig. 2.6(b), indicating high and uniform spatial resolution across the entire 40×40 cm^2 converter.

III.B. NNPS

Normalized NPS performance for two converters incorporating unfocused and focused 6 cm thick BGO segmented scintillators for various locations away from the central beam axis is shown in Fig. 2.7. Note that the fluctuations in the NNPS results in Figs. 2.7 and 2.10 (as well as the DQE results in Figs. 2.8 through 2.10), which do not affect the level and trend of the curves, originate from the finite number of frames used for the determination of NNPS. For the converter employing the unfocused scintillator, NNPS for the various regions largely overlap, as shown in Fig. 2.7(a). This invariance in NNPS is due to the largely unchanged size and shape of the energy

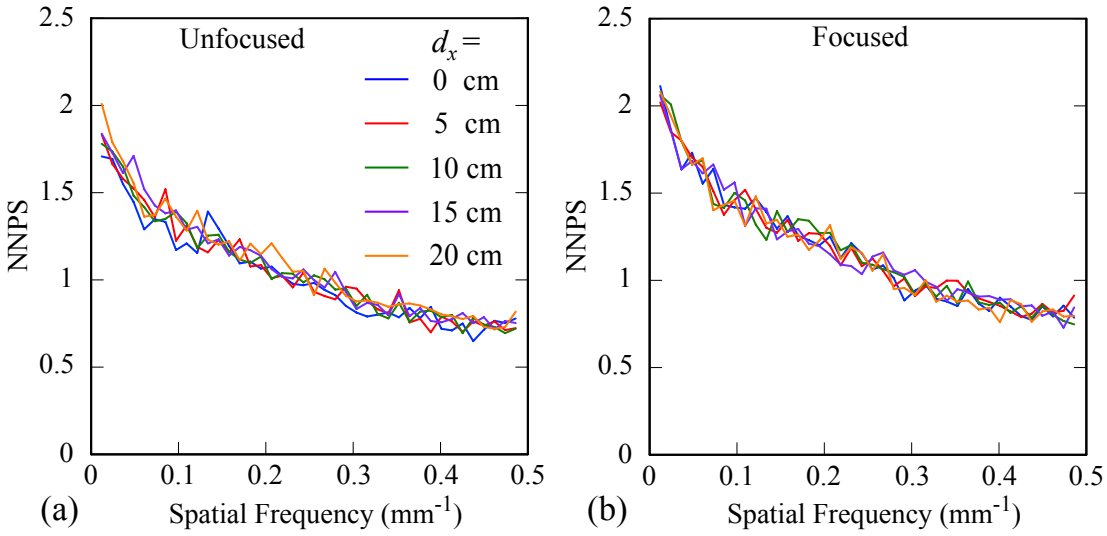

Figure 2.7. NNPS results for two converters incorporating 6 cm thick BGO scintillators at locations, d_x, ranging from 0 to 20 cm away from the central beam axis for (a) unfocused and (b) focused designs.

deposition of secondary Compton electrons over the range of incident x-ray angles employed in the simulations.[1] For the converter employing the focused scintillator, while NNPS for the various regions also largely overlap (for the same reasons as above), the results are systematically larger than those for the unfocused converter – as seen in Fig. 2.7(b). This difference is due to the lower x-ray detection efficiency of the focused converter (~6% less for a 6 cm BGO scintillator) that is a consequence of the good alignment of the less attenuating septal wall material with x-ray trajectories from the source.

III.C. DQE

DQE performance for converter designs incorporating segmented BGO scintillators with various thicknesses is shown in Fig. 2.8. For unfocused converters and at the central beam axis, DQE increases with scintillator thickness for all frequencies up to the Nyquist frequency, as seen in Fig. 2.8(a). However as seen in Fig. 2.8(b), at 20 cm off-axis and compared with thinner scintillators, although converters with thicker unfocused scintillators have greater low-frequency DQE values, they suffer from faster and steeper drop in DQE at high frequencies due to more severe beam divergence effects. As a consequence, beyond certain frequencies, DQE values for thicker unfocused scintillators are even lower than those of thinner scintillators. For example, for the converter with a 6 cm thick unfocused scintillator, the DQE value decreases significantly from over 0.40 at zero frequency to ~0.04 at 0.1 mm^{-1}. This decrease in DQE is mainly due to the severe drop in MTF at high frequencies shown in Fig. 2.6(a). However, as can be seen in Fig. 2.8(c), with the

introduction of focusing, DQE values at 20 cm off-axis are restored to within 0.10 of their levels without focusing at the central beam axis [Fig. 2.8(a)], as would be expected given the corresponding MTF and NNPS behaviors observed in Figs. 2.6(b) and 2.7(b), respectively. This is a significant restoration – representing, in the

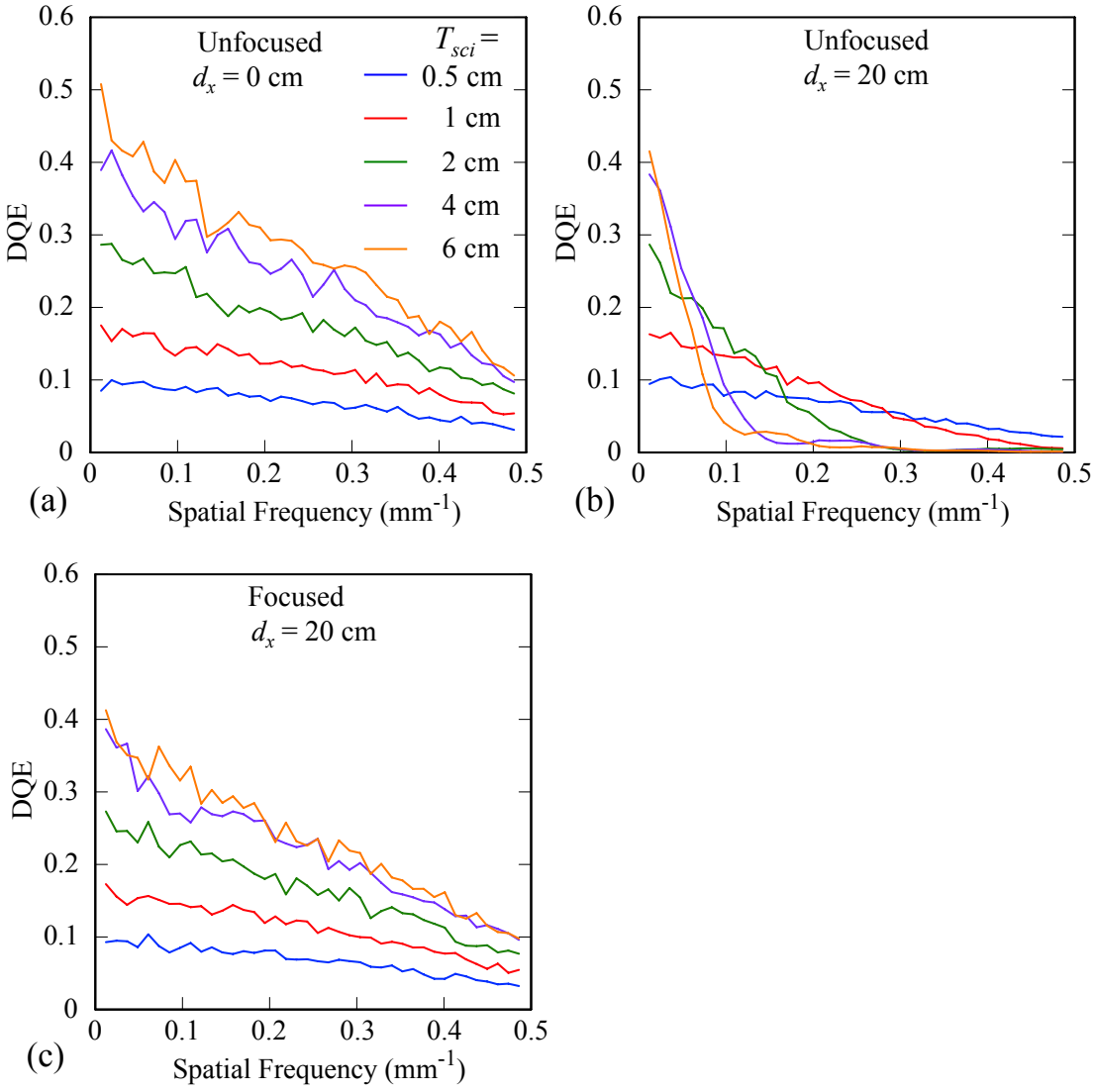

Figure 2.8. DQE results for converters incorporating segmented BGO scintillators with thicknesses, T_{sci}, ranging from 0.5 to 6 cm for: (a) unfocused designs at a location corresponding to the central beam axis, (b) unfocused designs at 20 cm off-axis, and (c) focused designs at 20 cm off-axis.

example of a 6 cm thick BGO scintillator, an increase in DQE of up to a factor of ~130 compared to the corresponding unfocused scintillator.

DQE results for converters incorporating unfocused and focused 6 cm thick BGO segmented scintillators at various locations are shown in Fig. 2.9. For the unfocused converter, DQE exhibits a dramatic decrease at locations progressively further away from the central beam axis, as shown in Fig. 2.9(a). Such variation in DQE, which is due to MTF loss for locations off-axis, would lead to progressive degradation of image quality further away from the central beam axis. For the focused converter, DQE curves are independent of location, as is evident in Fig. 2.9(b) – which should lead to greatly improved and more uniform image quality across a 40×40 cm^2 converter.

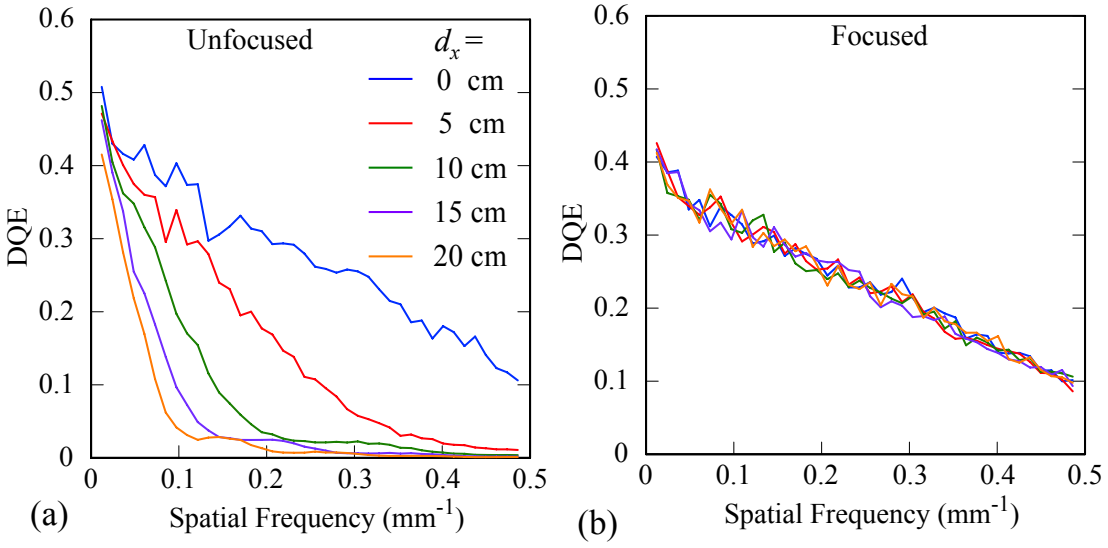

Figure 2.9. DQE results for converters incorporating 6 cm thick BGO scintillators at locations, d_x, ranging from 0 to 20 cm away from the central beam axis for (a) unfocused and (b) focused designs.

III.D. Simulation of converters based on other scintillator materials

Imaging performance at 20 cm off-axis for converter designs incorporating 6 cm thick, focused scintillators based on various scintillator materials is shown in Fig. 2.10. As seen in Fig. 2.10(a), the MTF values for BGO, LYSO and $CdWO_4$

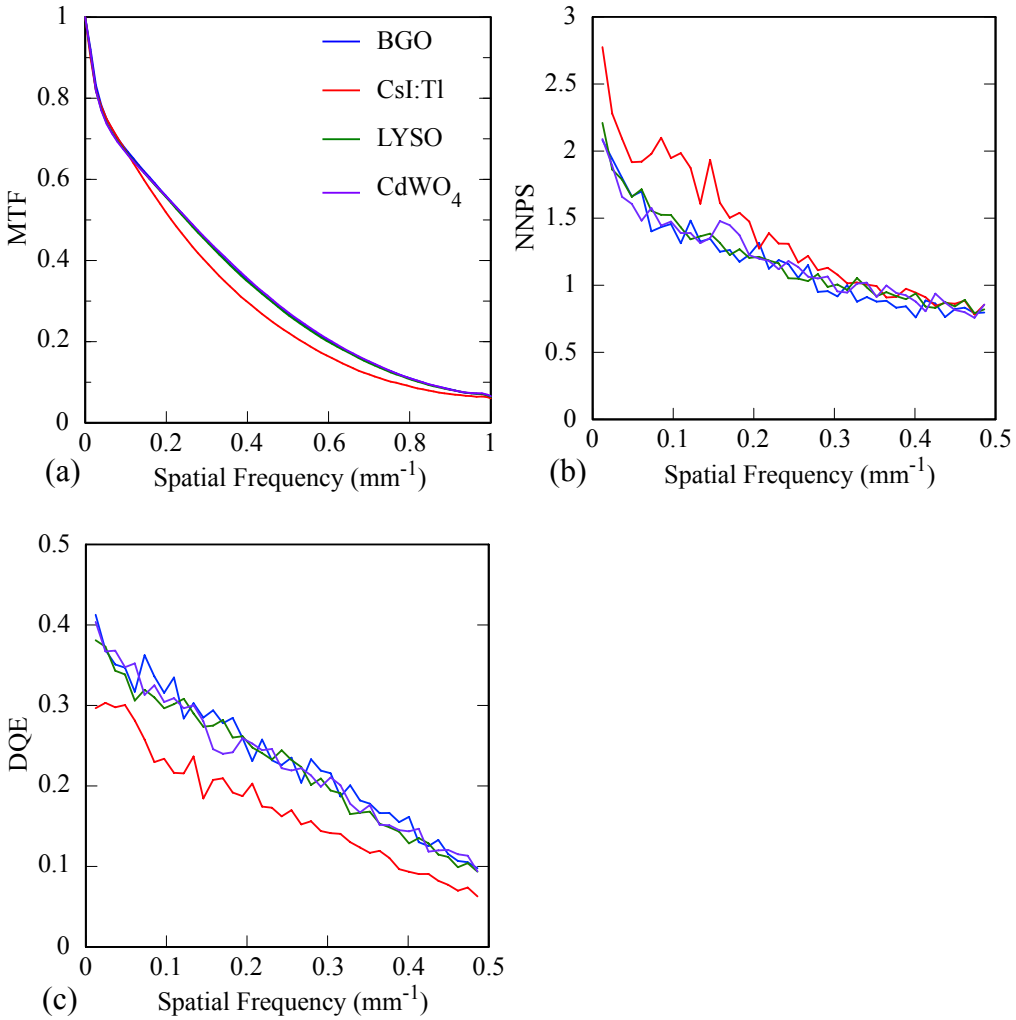

Figure 2.10. Simulation results at 20 cm off-axis for focused converters incorporating 6 cm thick scintillators consisting of various scintillator materials for: (a) MTF, (b) NNPS and (c) DQE.

converters largely overlap, providing similar spatial resolution. This can be attributed to a similar degree of lateral spread of deposited energy as a result of the similar electron densities (and therefore radiation stopping powers) of these materials. Note that the slightly lower MTF of the CsI:Tl converter is a result of reduced capacity to limit lateral spread of Compton electrons due to a lower electron density. For the same reason (i.e., lower electron density and thus lower x-ray detection efficiency), the CsI:Tl converter exhibits higher NNPS values than those based on the other three scintillator materials which almost overlap, as shown in Fig. 2.10(b). Therefore, as expected from Eq. (2.3), converter designs with BGO, LYSO and $CdWO_4$ scintillators provide similar DQE performance that is higher than that for CsI:Tl.

III.E. Tolerance of focused converter designs to imager displacement

A given focused planar converter design will generally be constructed for a specific position (e.g., for a specified SDD and for no lateral displacement with respect to the central beam axis) so as to ensure optimal focusing and imaging performance over the entire converter. Displacement of the converter from that intended position would be expected to lead to defocusing, resulting in some degree of degradation of spatial resolution and DQE performance.

To quantify the effect of operating a focused converter at non-optimal positions, simulations were performed for a converter incorporating a 6 cm thick BGO segmented scintillator designed for optimal performance at an SDD of 130 cm, as a function of SDD (z-direction) and lateral (x-direction) displacements, as

schematically illustrated in Figs. 2.11(a) and 2.12(a), respectively. Figure 2.11(b) shows MTF performance at 20 cm off-axis, for SDD displacements progressively further away from the radiation source. It can be seen that MTF suffers only slight degradation, even for a 10 cm SDD displacement, and still provides much higher performance than that of an unfocused converter. Note that while these MTF results are for displacements in the positive z-direction, results for displacements in the negative z-direction (i.e., closer to the radiation source) exhibit almost identical

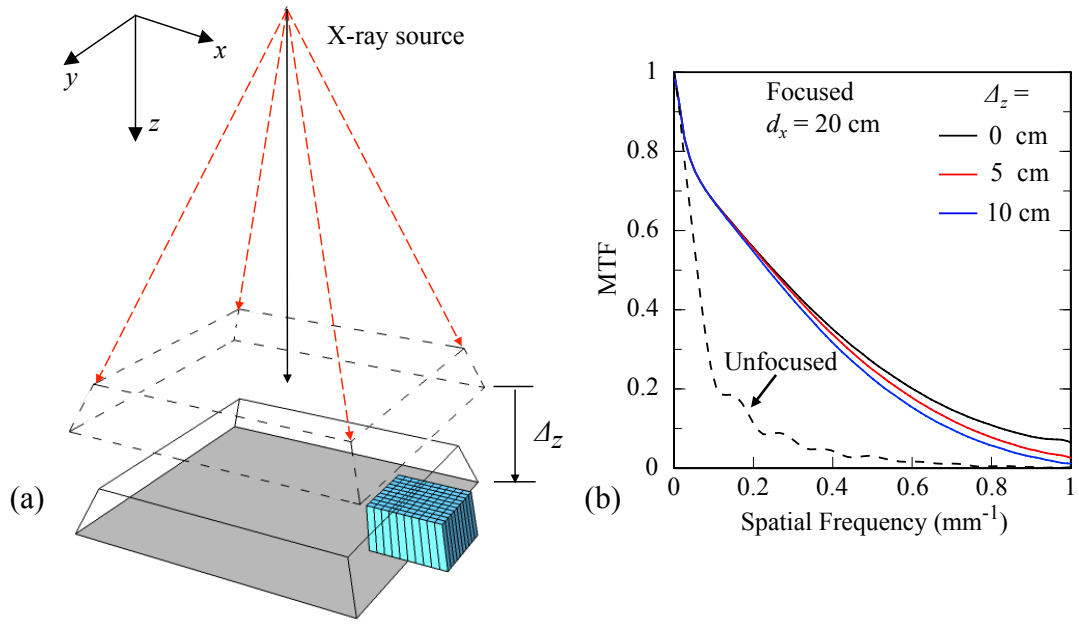

Figure 2.11. (a) Schematic drawing corresponding to simulations in which a converter (represented as a wire frame with a gray bottom surface) is displaced by a distance Δ_z along the source-to-detector (z-) direction from the optimal focusing position (dashed wire frame). In these simulations, the converter has no lateral displacement and is therefore centered at the central beam axis (black solid arrow). The simulated region (in blue) is located 20 cm off-axis. (b) MTF results for that region, for a focused converter with a 6 cm thick BGO scintillator, for various Δ_z displacements. For comparison, the MTF determined at 20 cm off-axis for an unfocused converter with a 6 cm thick BGO scintillator (with no SDD displacement) is shown by the dashed line.

values and thus are not shown. Figure 2.12(b) shows MTF performance at 20 cm off-axis for various lateral displacements. The MTF degradation caused by a 2 cm lateral displacement is found to be very similar to that caused by a 10 cm SDD displacement.

These results suggest that the MTF performance of focused converters is more sensitive to lateral displacement than SDD displacement, as would perhaps be expected, given the geometric construction of the focused elements. However, the results also indicate that, even when focused converters are operated relatively far from their optimal focusing position (i.e., up to at least 10 cm in the SDD direction or

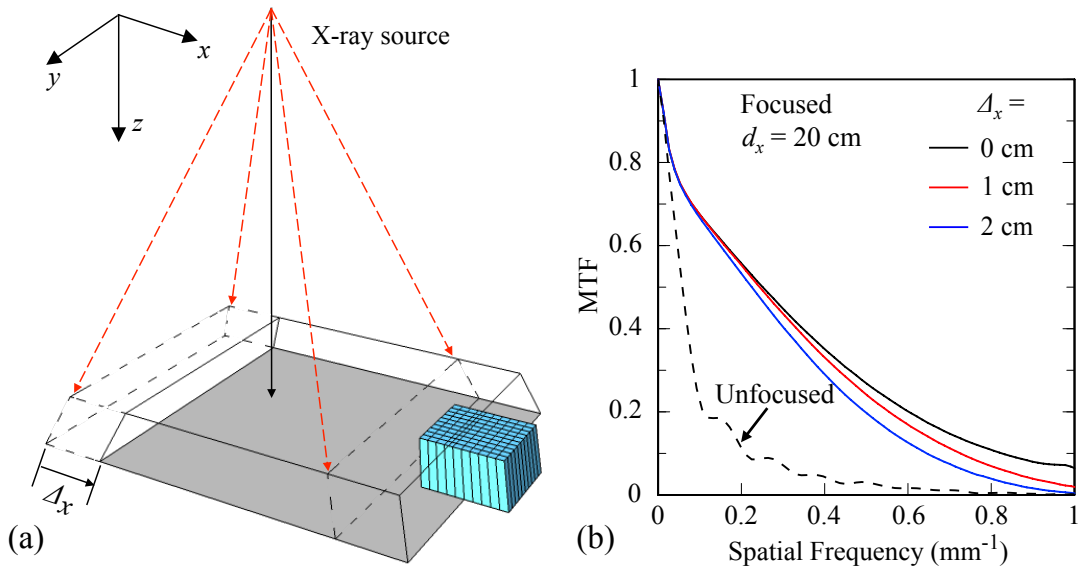

Figure 2.12. (a) Schematic drawing corresponding to simulations in which a converter is displaced a distance Δ_x in a lateral (x-) direction from the optimal focusing position (dashed wire frame). In these simulations, the converter has no SDD displacement. The simulated region (in blue) is located 20 cm away from the center of the converter. (b) MTF results for that region, for a focused converter with a 6 cm thick BGO scintillator, for various Δ_x displacements. For comparison, the MTF determined at 20 cm off-axis for an unfocused converter with a 6 cm thick BGO scintillator is shown by the dashed line.

2 cm in the lateral direction), they still provide significantly improved spatial resolution compared to that of unfocused converters. Note that NNPS was found to remain essentially unchanged for all displacements considered and, thus, DQE degradation can largely be attributed to MTF loss. The relatively small sensitivity of imager performance to SDD and lateral displacement could be of practical interest if it were clinically useful to allow such displacement capability so as to accommodate unusual clinical situations – e.g., larger SDD to accommodate particularly obese patients or lateral displacement to view far-off-axis regions of large fields.

IV. SUMMARY AND DISCUSSION

The results reported in this study strongly suggest that the degradation of imaging performance of thick converters caused by beam divergence can be largely eliminated through introduction of planar, focused segmented scintillators – at least for thicknesses up to 6 cm. Moreover, the performance of the focused planar converter designs examined in this study is only weakly degraded by moderate SDD or lateral displacement from the optimal focusing position.

REFERENCES – CHAPTER 2

[1] Y. Wang, Y. El-Mohri, L. E. Antonuk and Q. Zhao, "Monte Carlo investigations of the effect of beam divergence on thick, segmented crystalline scintillators for radiotherapy imaging," Phys. Med. Biol. **55**, 3659-3673 (2010).

[2] D. White, J. A. Kimerling and S. W. Overton, "Cartographic and geometric components of a global sampling design for environmental monitoring," Cartography and Geographic Information Science **19**, 5-22 (1992).

[3] L. E. Antonuk, "Electronic portal imaging devices: a review and historical perspective of contemporary technologies and research," Phys. Med. Biol. **47**, R31-R65 (2002).

[4] L. E. Antonuk, "a-Si:H TFT-based active matrix flat-panel imagers for medical x-ray applications," in *Thin Film Transistors, Materials and Processes, Volume 1: Amorphous Silicon Thin Film Transistors*, *Vol. 1,* edited by Y. Kuo (Kluwer Academic Publishers, Boston, 2004), pp. 395-484.

[5] R. A. Street, W. S. Wong and R. Lujan, "Curved electronic pixel arrays using a cut and bend approach," Journal of Applied Physics **105**, 104504 (2009).

[6] A. Sawant, L. E. Antonuk, Y. El-Mohri, Q. Zhao, Y. Wang, Y. Li, H. Du and L. Perna, "Segmented crystalline scintillators: Empirical and theoretical investigation of a high quantum efficiency EPID based on an initial engineering prototype CsI(Tl) detector," Med. Phys. **33**, 1053-1066 (2006).

[7] I. Kawrakow and D. W. O. Rogers, "The EGSnrc code system: Monte Carlo simulation of electron and photon transport," Technical Report PIRS-701, National Research Council of Canada, Ottawa, Canada (2000).

[8] I. Kawrakow, "egspp: the EGSnrc C++ class library," Technical Report PIRS-899, National Research Council of Canada, Ottawa, Canada (2005).

[9] D. Sheikh-Bagheri, "Monte Carlo study of photon beams from medical linear accelerators: Optimization, benchmark and spectra," Ph.D. dissertation, Department of Physics, Carleton University, Ottawa, Canada (1999).

[10] G. F. Knoll, *Radiation Detection and Measurement*. (John Wiley & Sons, 2010).

[11] Z. W. Bell, "Scintillation Counters," in *Handbook of Particle Detection and Imaging,* edited by C. Grupen and I. Buvat (Springer, Berlin, Heidelberg, 2012), pp. 349-375.

[12] H. Fujita, D. Y. Tsai, T. Itoh, K. Doi, J. Morishita, K. Ueda and A. Ohtsuka, "A simple method for determining the modulation transfer function in digital radiography," Medical Imaging, IEEE Transactions on **11**, 34-39 (1992).

[13] J. T. Dobbins, "Image quality metrics for digital systems," in *Handbook of Medical Imaging,* edited by J. Beutel, H. L. Kundel and R. L. V. Metter (SPIE Press, Bellingham, Washington, 2000), pp. 163–222.

[14] M. L. Giger, K. Doi and C. E. Metz, "Investigation of basic imaging properties in digital radiography. 2. Noise Wiener spectrum," Med. Phys. **11**, 797-805 (1984).

[15] A. D. A. Maidment and M. J. Yaffe, "Analysis of the spatial-frequency-dependent DQE of optically coupled digital mammography detectors," Med. Phys. **21**, 721-729 (1994).

[16] A. Sawant, L. E. Antonuk, Y. El-Mohri, Q. Zhao, Y. Li, Z. Su, Y. Wang, J. Yamamoto, H. Du, I. Cunningham, M. Klugerman and K. Shah, "Segmented crystalline scintillators: an initial investigation of high quantum efficiency detectors for megavoltage x-ray imaging," Med. Phys. **32**, 3067-3083 (2005).

[17] I. A. Cunningham, "Applied Linear -Systems Theory," in *Handbook of Medical Imaging,* edited by J. Beutel, H. L. Kundel and R. L. V. Metter (SPIE Press, Bellingham, Washinton, 2000), pp. 79-160.

CHAPTER 3

OPTIMIZATION OF THE DESIGN OF SEGMENTED SCINTILLATORS FOR MEGAVOLTAGE CONE-BEAM CT USING A NOVEL, HYBRID MODELING TECHNIQUE

I. INTRODUCTION

In this chapter, an examination of how variations in the design of BGO segmented scintillators affect imaging performance is reported. BGO was chosen due to the generally promising performance of previous prototype segmented scintillators incorporating this material, resulting from properties such as high electron density and refractive index, as well as a high degree of optical transparency. [1-3] The present investigation involves simulation of reconstructed images of a contrast phantom using a CBCT geometry at clinically realistic radiation doses – accounting for both radiation and optical transport effects. Given the very large number of x-ray histories required for the study, a purely event-by-event Monte Carlo modeling approach would have been computationally prohibitive even had the scintillation yield been reduced to a level consistent with avoiding deleterious effect on accuracy. For that reason, a novel hybrid modeling technique that reduced the computational time required to model various scintillator designs to a practical level was devised and implemented. This technique was used to evaluate the performance, in terms of

contrast, noise, and contrast-to-noise ratio (CNR), of a variety of hypothetical designs. The technique was also used to examine the spatial resolution performance of the designs in terms of the modulation transfer function (MTF). CNR is a widely-accepted metric that is commonly employed for characterization of the performance of volumetric CBCT imaging systems employing AMFPIs.[2, 4-11] MTF is a standard metric commonly employed for characterization of 2D imaging system spatial resolution performance. Improvements to MTF resulting from adjustments to scintillator design are expected to lead to 3D spatial resolution improvement, the degree of which depends on the multitude of factors that affect the latter, as described in Section IV. Finally, a graphical method of combining CNR and MTF simulation results so as to provide further insight into design considerations that affect performance is introduced and discussed.

II. METHODS

II.A. Overview of converter designs and radiation simulation setup

Each segmented scintillator design examined in the study consists of a two-dimensional matrix of elements comprising rectangular cuboid-shaped (i.e., unfocused) scintillator crystals separated by 0.05 mm thick, polystyrene septal walls. All designs employ BGO material with thicknesses ranging from 0.5 to 6 cm and element-to-element pitches ranging from 0.508 to 1.524 mm. The 0.5 cm lower limit on thickness corresponds to a point below which improvements in detection efficiency become marginal, whereas the 6 cm upper limit corresponds to a point beyond which the rate of improvement in detection efficiency as a function of

thickness rapidly declines. The range chosen for pitch roughly brackets the range of spatial resolution of interest for therapy imaging.

For the CBCT simulation study, the scintillators have a detection area of ~70×140 mm^2 with pitches of 0.508, 0.762, 1.016, 1.270, and 1.524 mm, resulting in matrix formats of 141×281, 95×189, 71×141, 57×113, and 47×93, respectively. This detector area was chosen to be sufficiently large so as to allow imaging of the contrast phantom discussed below. For each scintillator, the radiation transport simulations included a 1 mm thick overlying layer of copper, representing the metal plate that is commonly used in MV portal imagers. Details of the setup are shown in Fig. 3.1 and a brief description follows. A point x-ray source, simulating a 6 MV photon beam with a spectral output corresponding to that of a Varian radiotherapy linear accelerator [12] and located 130 cm away from the scintillator, was used. A contrast phantom with dimensions, composition and inserts similar to those of an actual phantom used in a previous empirical MV CBCT study [2] was simulated. The phantom was positioned above the scintillator with its center at a distance of 124.2 cm from the source. It consists of an 11.4 cm diameter solid water cylinder with three cylindrical inserts, all having a common length of 6 cm. A total of 12 different inserts, each having a diameter of 2.8 cm, were simulated, corresponding to four different phantom insert sets. The designations and physical properties of these materials are summarized in Table 3.1. In the simulations, the x-ray fluence (i.e., the number of X rays per unit area) incident on the phantom per tomographic scan was set to a value of 4.32×10^7 X rays/mm^2 at a SDD of 130 cm. This value was determined through

separate simulations in such a way as to provide a dose equivalent to the 4 cGy used in the previous empirical CBCT study – thereby facilitating direct comparisons with those results.

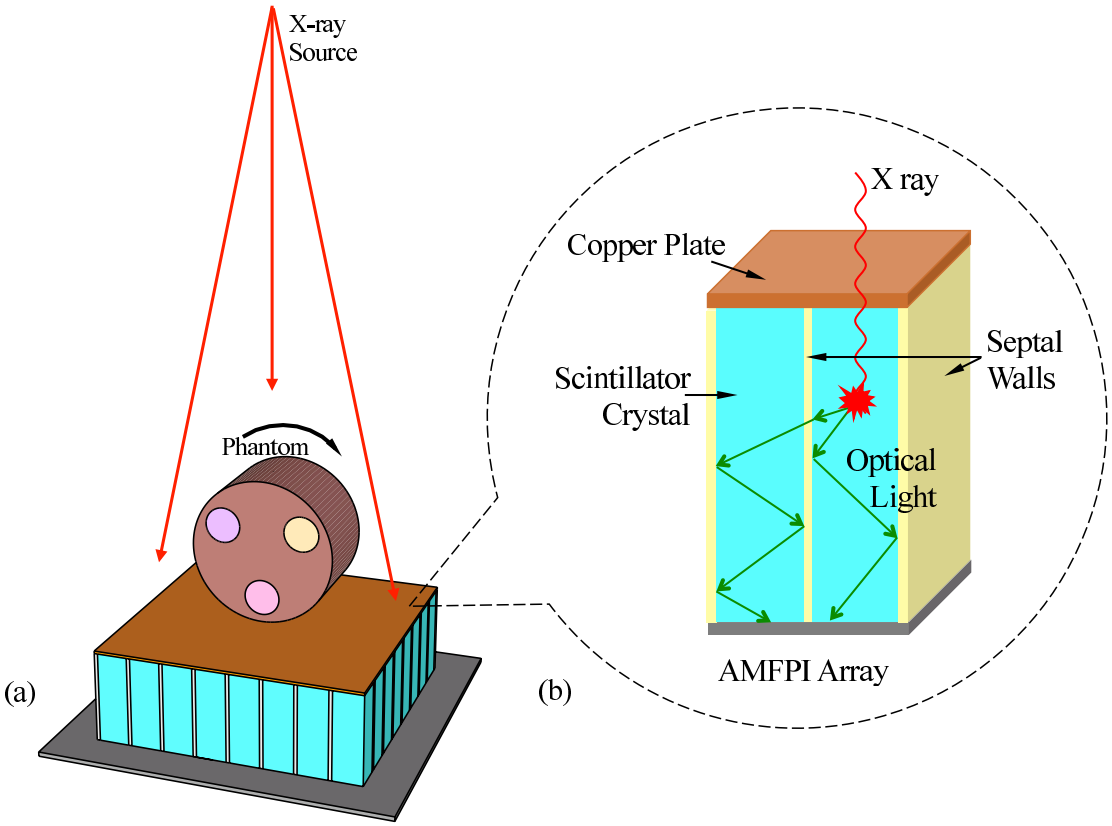

Figure 3.1. (a) Schematic illustration of the setup employed in the CBCT simulations, including the x-ray converter and contrast phantom. The x-ray converter consists of a copper plate and a regular, two-dimensional matrix of elements (comprising scintillator and septal wall material) which are registered to the pixels of an underlying, indirect detection AMFPI array. (b) Enlarged view of the scintillator elements illustrating the physical process of energy deposition as well as of generation and transport of optical photons.

For the radiation transport part of the MTF simulation study, the spatial resolution for each scintillator design was characterized in terms of the presampled MTF, using the angled slit technique.[1, 13, 14] The simulation method used to determine

MTF follows that reported in Chapter 2 and is briefly summarized as follows. Each design was simulated as a matrix of 101×101 scintillator elements with an overlying, 1 mm thick, copper plate located at a distance of 130 cm from an x-ray point source. The slit was modeled as a fan beam of 6 MV incident X rays, defining an aperture, centered along the central beam axis, of 10.26 cm × 4 μm at the detector entrance surface. The longer dimension of the slit was oriented at a small, fixed angle of 2° with respect to one direction of the matrix of scintillator elements. For each MTF simulation, 4×10^5 primary x-ray histories were employed – a number sufficient to keep statistical errors below 0.9%.

Table 3.1. List of designations, densities and electron densities relative to water for the tissue-equivalent materials of the simulated contrast phantom examined in this study. In these simulations, the composition and physical properties of each of the materials correspond to those of the actual phantom used in a previous empirical study [2] – as provided by the manufacturer (Tissue Characterization Phantom, Gammex 467, Gammex rmi, Middleton, WI). Note that there are two entries for solid water material: one for the material comprising the main body of the phantom, and another for one of the tissue-equivalent inserts.

Designation of Tissue-equivalent Materials	Density (g/cm^3)	Electron Density Relative to Water
Lung (LN-300)	0.29	0.280
Lung (LN-450)	0.44	0.429
Adipose (AP6)	0.94	0.925
Breast	0.98	0.954
Solid Water (Insert)	1.017	0.988
Solid Water (Phantom)	1.046	1.016
Brain	1.053	1.049
Liver (LV1)	1.097	1.065
Inner Bone	1.143	1.096
Bone (B200)	1.154	1.106
Bone (CB2-30% Mineral)	1.335	1.280
Bone (CB2-50% Mineral)	1.56	1.470
SB3 Cortical Bone	1.825	1.697

II.B. Hybrid modeling technique

Simulation of the reconstructed CBCT images of the contrast phantom and of MTF was performed using a hybrid modeling technique. For each scintillator design, the technique entails a sequential process. First, projection radiation images are obtained from radiation transport simulation. Next, to account for the stochastic noise associated with energy-to-light conversion and detection, optical Swank noise,[15] deduced from optical gain distributions obtained from optical transport simulation, is added to those images. Finally, to account for spatial spreading of optical photons, optical blur is introduced through convolution of the noise-corrected images with an optical point spread function (PSF) that is obtained from the same optical transport simulation. A flowchart illustrating the implementation of the modeling technique is shown in Fig. 3.2 and a description of the various steps follows.

The Monte Carlo simulations of radiation transport were performed using the EGSnrc code.[16] In the simulations, the geometry of the scintillators and the contrast phantom were modeled using the EGSnrc C++ class library (egspp)[17] – with the user code, as well as the input file that defines the geometry, modified as necessary. A unified input file generator for EGSnrc was created to facilitate the generation of numerous input files for a variety of purposes (e.g., determination of MTF, NPS, DQE, CBCT, etc) – the details of which are documented in Appendix C. In the simulations, the cutoff energies for photons and electrons were set to 0.01 and 0.521 MeV, respectively, corresponding to a kinetic energy of 0.01 MeV. The EXACT boundary-crossing algorithm, PRESTA-II electron-step algorithm and NIST

bremsstrahlung cross sections were also used. The simulations were performed on a 64-bit Linux cluster with ~800 processor cores (4.0 GHz AMD FX Series). The parallelization of simulations on the cluster is detailed in Appendix D.

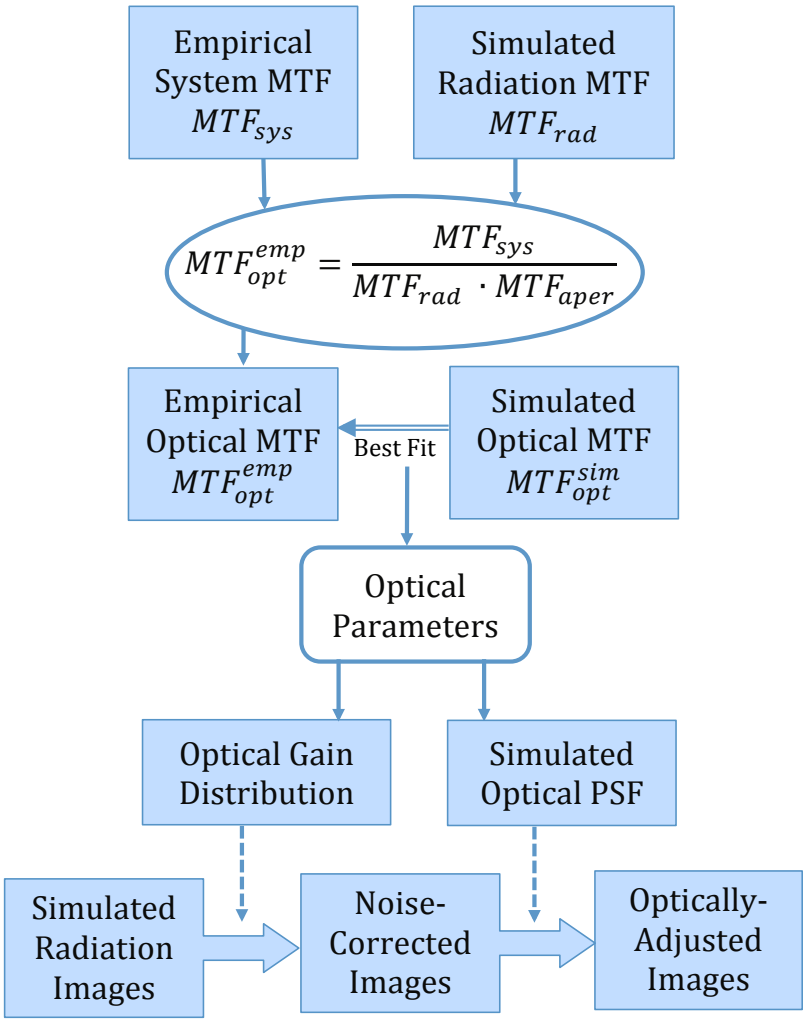

Figure 3.2. Flowchart illustrating the hybrid modeling technique used to determine the CBCT and MTF performance of various scintillator designs. The lower half of the chart depicts how, for each scintillator design, optical effects are introduced using a simulated optical gain distribution and PSF. The upper half of the chart depicts how the optical parameters used to simulate the optical gain distributions and PSFs are obtained. See main text for details.

The optical gain distribution and PSF for each design were also obtained through Monte Carlo simulation. These simulations employed optical parameters extracted from fits to published empirical MTF results for a 1.13 cm thick, 1.016 mm pitch prototype BGO segmented scintillator with septal walls consisting of 0.05 mm thick polymer reflector.[1] For the determination of these parameters, the expression representing the MTF of the system:

$$MTF_{sys} = \frac{MTF_{rad} \times MTF_{opt}}{MTF_{aper}}, \tag{3.1}$$

is based on an expression from reference 18, where the system MTF is assumed to consist of radiation, optical and aperture components. In Eq. (3.1), MTF_{rad}, MTF_{opt} and MTF_{aper} represent the radiation MTF, the optical MTF, and the aperture sinc function corresponding to the aperture defined by the cross sectional size of the crystal of a scintillator element, respectively. Compared to the expression in reference 18, Eq. (3.1) takes a slightly different (though mathematically equivalent) form by deliberately including the contribution of MTF_{aper} into both MTF_{rad} and MTF_{opt} – a convention adopted for convenience given that this quantity is naturally embedded in all MTFs simulated in this study. The optical parameters were determined by fitting a simulated optical MTF, MTF_{opt}^{sim}, to an empirically-based optical MTF, MTF_{opt}^{emp}. MTF_{opt}^{emp} itself was determined using Eq.(3.1) with values for MTF_{sys}, MTF_{rad} and MTF_{aper} obtained from previously published empirical results for the prototype, radiation transport simulation of that scintillator, and calculation, respectively.

The simulation of MTF_{opt}^{sim} was based on Monte Carlo techniques involving use of the optical simulation capabilities of Geant4.[19] Optical photons were generated within a narrow volume of the scintillator having a cross-sectional area corresponding to the slit used in the radiation transport part of the MTF simulations. While the photons were generated uniformly across that area, they followed a characteristic probability distribution in the depth direction that was based on the depth profile of the radiation energy deposited in the prototype scintillator. In those simulations, the interaction of optical photons with surfaces that separate neighboring media dominates optical spreading in the scintillator, since absorption and scattering in the scintillator crystal are negligible given the high degree of transparency of BGO.[20] The types of boundary interactions that could occur are included in Fig. 3.3 which represents a flowchart of the optical simulation steps. Briefly, at each boundary, there are four possible outcomes for a given photon (absorption, total internal reflection, transmission or reflection) and the probability for each outcome is controlled by three parameters – absorptivity (α), roughness (β) and transmittance (τ). The set of values for these parameters that provided the best fit to the empirical results were subsequently used to simulate (also using Geant4) the optical gain distribution and PSF for each of the hypothetical scintillator designs.

For each hypothetical scintillator design, the simulation of the optical gain distribution and PSF involved the generation of optical photons inside the central element of a segmented scintillator consisting of 101×101 elements. A simulation consisting of 10,000 runs, with each run using 10,000 optical photon histories, was

performed for a given design. While the photons were generated uniformly across the area of the crystal in the central element, they followed the radiation energy deposition profile for the corresponding scintillator in the depth direction. Following their transport through the scintillator, those optical photons exiting the bottom

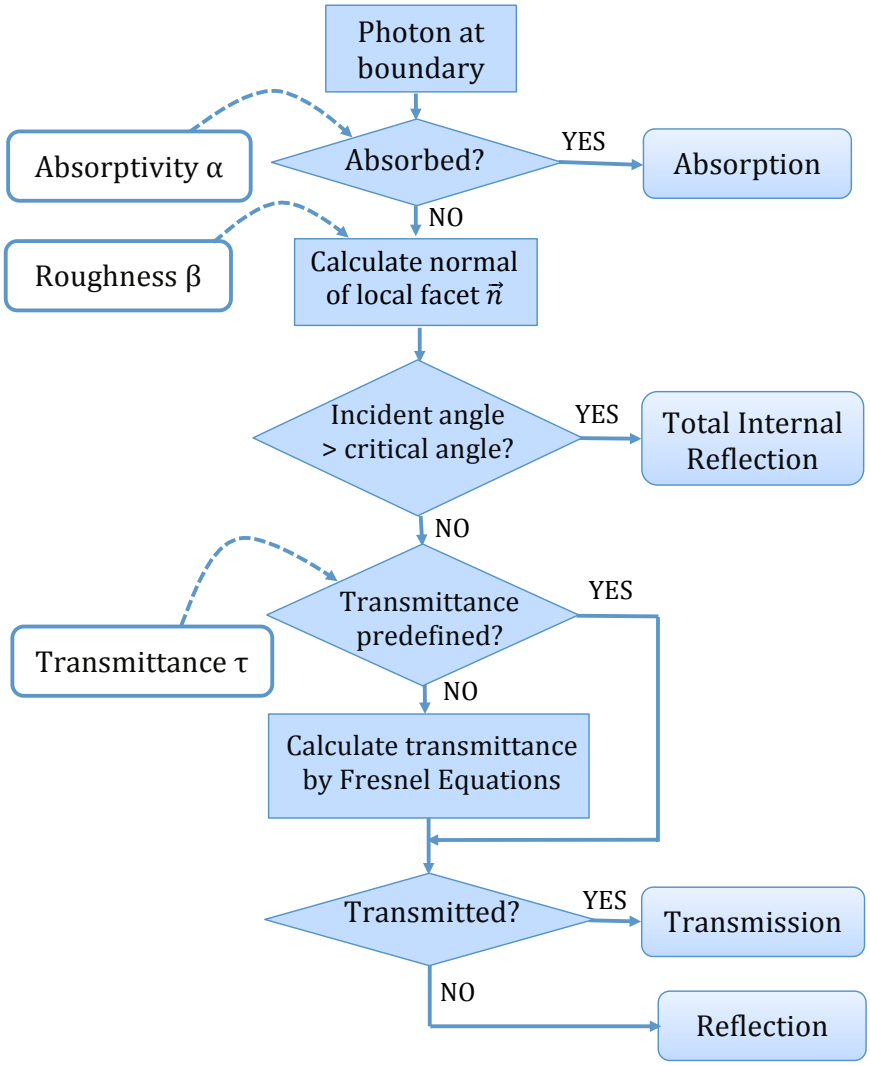

Figure 3.3. Flowchart illustrating the logic applied to the consideration of the various boundary processes involved in the optical transport simulations. The sequence of decisions corresponds to the program structure of the optical simulation code in Geant4. The parameters that could, in principle, be used to characterize each boundary in the optical model are indicated on the left while the four possible outcomes are on the right. Note that, in the code, the value of transmittance can either be predefined or calculated using Fresnel Equations.

surface of the scintillator were recorded and that information was used as follows. In order to account for optical Swank noise in the radiation images, a histogram of the total number of recorded exiting photons per run, representing the optical gain distribution, was formed. For each scintillator element of each radiation image, this distribution, with a mean value μ and a standard deviation σ, was scaled according to the actual number of optical photons generated from the radiation energy deposited in that element (i.e., the radiation signal), using the following expressions for the mean value, μ_{sc}, and standard deviation, σ_{sc}, of the scaled distribution:

$$\mu_{sc} = \mu \frac{q\eta}{N_0}, \quad \sigma_{sc} = \sigma \sqrt{\frac{q\eta}{N_0}} \tag{3.2}$$

In these expressions, q is the signal value in the radiation image, η is the energy-to-light conversion gain (8,000 photons per MeV for BGO), and N_0 is the number of optical photons used in each simulation (10,000). For each element, random sampling was performed according to the corresponding scaled distribution to convert the radiation signal to a new signal value, resulting in an optical, noise-corrected image. In order to account for optical blur, the recorded exiting photons across all 10,000 runs were binned according to the element pitch to produce a discrete optical PSF which was convolved with the noise-corrected image to form the final, optically-adjusted image.

The inclusion of optical effects through use of a simulated optical gain distribution and PSF, as opposed to directly simulating the transport of the individual

optical photons generated by each X ray interacting in the scintillator, consolidates the computation burden of optical transport simulations to a single optical simulation per design. This resulted in a significant reduction in the computation time required for the optical simulations from an estimated 10^8 to 10^{10} CPU hours to only ~30 CPU hours per design. As a result, whereas the present study would have required a total of ~10^{11} CPU hours (dominated by optical transport simulation for the CBCT study), only ~3.3×10^6 CPU hours (dominated by radiation transport simulation for that study) was required.

II.C. Determination of *Contrast*, *Noise*, *CNR* and MTF

For the CBCT simulation study, for each phantom insert set and scintillator design, 180 projection radiation images were obtained by scanning the phantom tomographically with 2° angular increments over a 360° rotation. Separately, a set of 180 flood radiation images was obtained in the absence of the phantom, each using the same dose as that used for the individual projection images of the phantom. All radiation images were adjusted to include optical Swank noise and optical blur. A Feldkamp-based algorithm employing a ramp filter was used to reconstruct the spatial distribution of attenuation coefficients of the phantom from a combination of the set of adjusted projection images and the average of the 180 adjusted flood images.[7] The reconstructed voxel pitch and single slice thickness were chosen to be equal to the element pitch of the scintillator design. From the reconstructed tomographic images, a suitable number of consecutive single slices were averaged so as to provide a slice thickness of ~5 mm, irrespective of the element pitch. All reconstructed images were

subject to a cupping artifact correction to remove a background trend due to beam hardening.[7]

Performance of the various scintillators was characterized in terms of contrast (*Contrast*), noise (*Noise*), and Contrast-to-noise ratio (*CNR*) of the tissue-equivalent inserts relative to the water-equivalent background in the reconstructed images of the contrast phantom. The analysis methods closely follow those used in a previous study.[2] In brief, the contrast of a given insert was calculated in Hounsfield units (HU) using the equation:

$$Contrast = \frac{S_{obj} - S_{water}}{S_{water}} \times 1000 \text{ (HU)}, \tag{3.3}$$

where S_{obj} and S_{water} represent the mean signal in the insert and water-equivalent regions, respectively. The signal for each insert is taken from a region consisting of an inner circle of ~14.2 mm diameter that excludes the edge of the insert while the signal for the background includes regions between the inserts, excluding the edges and center of the phantom. Similarly, the noise in the inserts was calculated using the equation:

$$Noise = \frac{\sigma_{obj}}{S_{water}} \times 1000 \text{ (HU)}, \tag{3.4}$$

where σ_{obj} represents the standard deviation of the signal in the inserts. CNR was calculated using:

$$CNR = \frac{S_{obj} - S_{water}}{\sigma_{obj}}. \tag{3.5}$$

For the MTF simulation study, for each scintillator design, an image frame of energy deposited in the scintillator crystals by the angled radiation slit was obtained. This image was adjusted to include optical Swank noise and optical blur. From this adjusted image, a line spread function was determined using the angled-slit technique, the 1D Fourier transform of which yielded the MTF. Note that the analysis methods described above were also used to obtain CNR and MTF results in the absence of optical effects – results which are referred to as "radiation-only".

III. RESULTS

III.A. Determination of optical parameters

A list of the various optical parameters that could, in principle, be employed in optical simulation of interactions of photons with the top, side and bottom surfaces of the elements of the segmented scintillator is given in Table 3.2. For the present study, the top surface parameters were specified so as to correspond to either a black or a mirror top reflector (black: α_{top}=1; mirror: α_{top}=0, τ_{top}=0) – representing the reflectors employed in the previous empirical study.[1] In addition, transmittance for the sidewall and bottom surfaces, τ_{side} and τ_{bot}, were calculated using Fresnel Equations [21] employing the refractive index values appearing in Table 3.2. For the remaining optical parameters, a series of test simulations were performed to confirm that, as expected, the parameters of the sidewall surfaces (sidewall absorptivity, α_{side}, and roughness, β_{side}) dominate the lateral spread of optical photons. For that reason, those dominant parameters were varied in a two-dimensional parameter sweep to find

the combination of values that provide the best fit to the empirically determined optical MTFs for both the black and mirror top reflectors. The other applicable parameters (roughness of the top and bottom surfaces, β_{top} and β_{bot}) were kept constant at arbitrary values since variation in these values had negligible effect on the results.

Table 3.2. Summary of optical parameters associated with simulations performed with the Geant4 package: absorptivity, α, roughness, β, and transmittance, τ, for the top, side and bottom of the scintillator elements. The first two columns indicate those parameters that could, in principle, be used in the simulations. For those parameters and for each of a black and mirror top reflector, the table also indicates: the fixed value assigned to some parameters; the parameters that were irrelevant in the study ("Not applicable"); the parameters whose values have little effect upon the fitting ("Insensitive"); the range of parameter values (and increment) considered in the fitting of the empirically determined optical MTF; and the parameters whose values were calculated ("Calculated"). Finally, the values used for the refractive indices of BGO, septal wall material and a-Si of the underlying AMFPI array are also shown.

		Black reflector	**Mirror reflector**
Top surface	α_{top}	1	0
	β_{top}	Not applicable	1 (Insensitive)
	τ_{top}	Not applicable	0
Side surface	α_{side}	Range: 0 – 0.15 (Increment: 0.01)	
	β_{side}	Range: 0 – 1 (Increment: 0.1)	
	τ_{side}	Calculated	
Bottom surface	α_{bot}	Not applicable	
	β_{bot}	1 (Insensitive)	
	τ_{bot}	Calculated	
Refractive Index	n_{BGO}	2.15	
	n_{septa}	1.55	
	n_{a-Si}	1.7	

Figure 3.4 shows MTF results related to the determination of the optical parameters from empirical MTF results, MTF_{sys}, obtained from the prototype BGO scintillator using the black and mirror top reflectors. The figure includes values for the various factors appearing in Eq. (3.1): MTF_{sys} (from reference 1), MTF_{rad} (from simulation) and MTF_{aper} (from calculation), as well as MTF_{opt}^{emp} (obtained from these three quantities using the equation). In addition, the simulated optical MTFs, MTF_{opt}^{sim}, which represent the best fits to MTF_{opt}^{emp} for both reflectors, are also shown. The agreement between MTF_{opt}^{sim} and MTF_{opt}^{emp} is seen to be good right up to the Nyquist frequency of ~0.5 mm^{-1}. The values of sidewall absorptivity α_{side} and

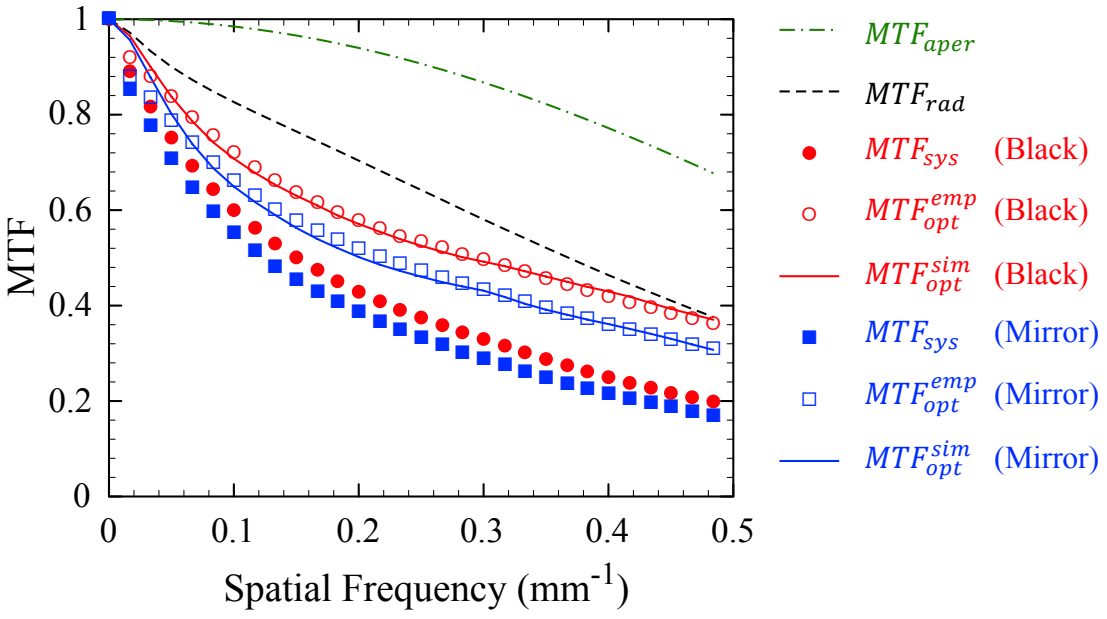

Figure 3.4. Measured and simulated presampled MTF results corresponding to the prototype BGO segmented scintillator. For each of a *black* and *mirror* top reflector, results are shown for previously reported empirical results obtained from the prototype, MTF_{sys};[1] for optical MTF values extracted from the empirical results, MTF_{opt}^{emp}; and for fits to those optical values, MTF_{opt}^{sim}. The calculated aperture function, MTF_{aper}, and simulated radiation MTF, MTF_{rad}, are also shown.

roughness β_{side} determined from these fits are 0.08 and 0.5, respectively. Note that the optical MTFs are much lower than the upper limit represented by the aperture function which corresponds to the optical MTF of a segmented scintillator exhibiting perfect optical isolation between scintillator elements. The deduced values for the optical parameters therefore reflect the good, but less than perfect, optical isolation provided by the septal walls of the BGO prototype.

III.B. Validation of the hybrid modeling technique

In Fig. 3.5, simulated reconstructed images of the contrast phantom using the hybrid model, for a design representing that of the BGO prototype, are compared to corresponding empirical images previously reported for that prototype.[2] Note that, since a mirror top reflector was used in that empirical study, all simulations of the optical gain distribution and PSF employed such a reflector. In the figure, two phantom insert sets corresponding to six different inserts are shown. In comparison with the simulated images employing only radiation transport (Fig. 3.5(b)), the addition of optical effects by means of the hybrid model results in images (Fig. 3.5(c)) that exhibit a smoother, less noisy background that is qualitatively closer to the empirical results (Fig. 5(d)).

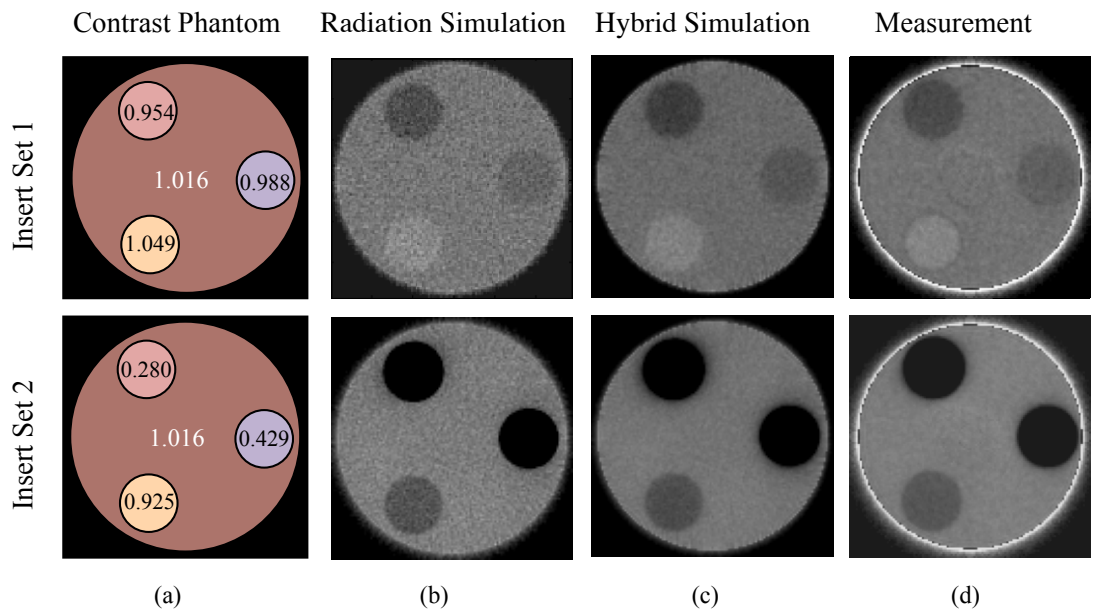

Figure 3.5. Phantom information and MV CBCT images related to the prototype BGO scintillator for two phantom insert sets corresponding to different sets of soft-tissue inserts. (a) Values of electron densities of inserts and background relative to water. (b) Reconstructed images obtained using simulation of radiation transport only. (c) Reconstructed images obtained using the hybrid model. (d) Reconstructed images from a previous empirical study.[2] All reconstructed images were acquired at a dose of 4 cGy.

The agreement between the simulations using the hybrid model and empirical results extends beyond visual similarity. In the case of *Contrast*, results from both radiation-only simulation and hybrid simulation provide equally good agreement with empirical results, as seen in Fig. 3.6. This is simply a consequence of the fact that this metric is signal-based and is determined by the attenuation properties of the object imaged, so that optical Swank noise and blur are not expected to affect it. However, for *Noise* and *CNR*, the degree of agreement between the hybrid simulation results and empirical results is much better than that between radiation-only simulation results and empirical results. This closer agreement is largely the result of the reduction in noise introduced by the optical blur in the simulated images. The

good qualitative and quantitative agreement between the images obtained from the hybrid model and those obtained empirically, as demonstrated in Figs. 3.5 and 3.6, strongly supports the validity of the optical parameters used as well as the predictive capabilities of the hybrid modeling technique.

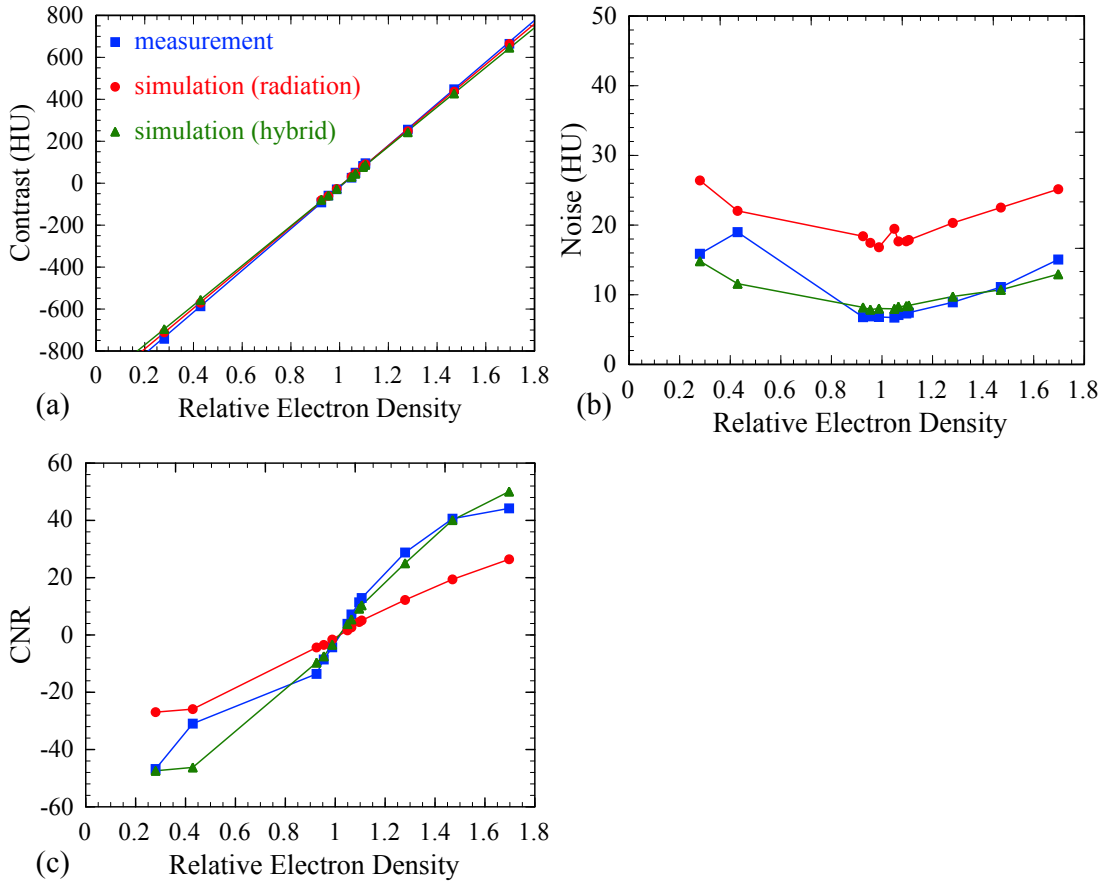

Figure 3.6. Results related to the prototype BGO scintillator for four phantom insert sets corresponding to twelve different soft-tissue inserts (see Table 3.1) for (a) *Contrast*, (b) *Noise*, and (c) *CNR*. The results shown were obtained from simulations employing radiation transport only (circle symbols), from simulations using the hybrid model (triangle symbols), and from a previous empirical study [2] (square symbols). Note that, as previously reported,[2] the empirical result for each of *Noise* and *CNR* at a relative electron density of 0.429 is anomalous compared to the overall trend of the remainder of the dataset.

III.C. Performance evaluation of scintillator designs

Using the hybrid modeling technique, MV CBCT and spatial resolution performance for the phantom corresponding to Insert Set 1 in Fig. 3.5 were evaluated for various hypothetical scintillator designs. For segmented scintillators with 1.016 mm pitch (corresponding to that of the prototype) and thicknesses ranging from 0.5 to 6 cm, Fig. 3.7 shows *Contrast*, *Noise* and *CNR* results obtained from MV CBCT

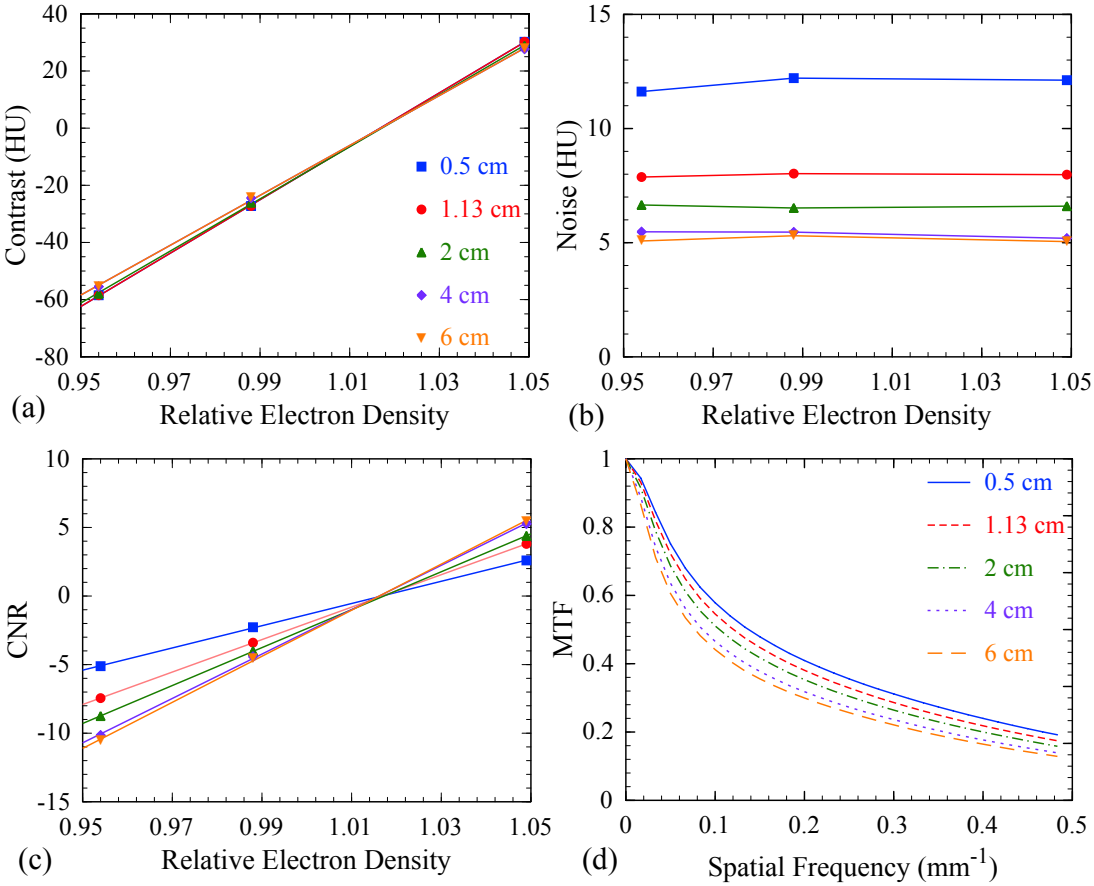

Figure 3.7. Simulation results obtained using the hybrid model for hypothetical 1.016 mm pitch BGO scintillator designs with varying thicknesses for (a) *Contrast*, (b) *Noise*, and (c) *CNR*. The results are plotted as a function of electron density of tissue-equivalent inserts relative to water. (d) Simulated results for MTF for those designs. Note that the lines appearing in the *Contrast* and *CNR* plots represent linear fits to the results.

images of the phantom as well as the corresponding MTFs. As seen in Fig. 3.7(a), thicker scintillators result in a slightly shallower slope in the plot of *Contrast* versus relative electron density of the inserts, due to a small reduction in the *absolute* values of contrast. Such diminution of contrast is probably the result of additional background scatter in the projection images caused by a higher probability of reabsorption of recoil Compton X rays for thicker scintillators. As seen in Fig. 3.7(b), thicker scintillators exhibit lower *Noise* as a result of the increase in the number of quanta sampled due to improved x-ray detection efficiency and increased optical blur. As a consequence, thicker scintillators provide a steeper *CNR*-slope (and therefore better soft tissue visualization), as seen in Fig. 3.7(c). However, thicker scintillators also suffer from reduced MTF, as seen in Fig. 3.7(d), due to more pronounced lateral spread of both radiation energy deposition and optical photons in the scintillator.

A similar performance evaluation was performed for segmented scintillators with a thickness of 1.13 cm (corresponding to that of the prototype) and element pitches ranging from 0.508 mm to 1.524 mm, and the results are shown in Fig. 3.8. For *Contrast*, the dependence on element pitch is almost negligible, with only a small deviation apparent at a pitch of 1.524 mm, as seen in Fig. 3.8(a). This deviation may be the result of larger statistical variations of *Contrast* due to a smaller number of voxels used in the regions of interest. For *Noise*, scintillators with a larger pitch exhibit lower *Noise* levels, as seen in Fig. 3.8(b), due to the larger number of quanta collected by a given element and the reduced optical Swank noise contribution due to a smaller aspect ratio of the crystals.[22] As a consequence, scintillators with larger

pitch provide steeper *CNR*-slope, as seen in Fig. 3.8(c), leading to better soft-tissue visualization. However, as expected, scintillators with larger pitch also exhibit degraded spatial resolution characterized by lower MTF, as seen in Fig. 3.8(d).

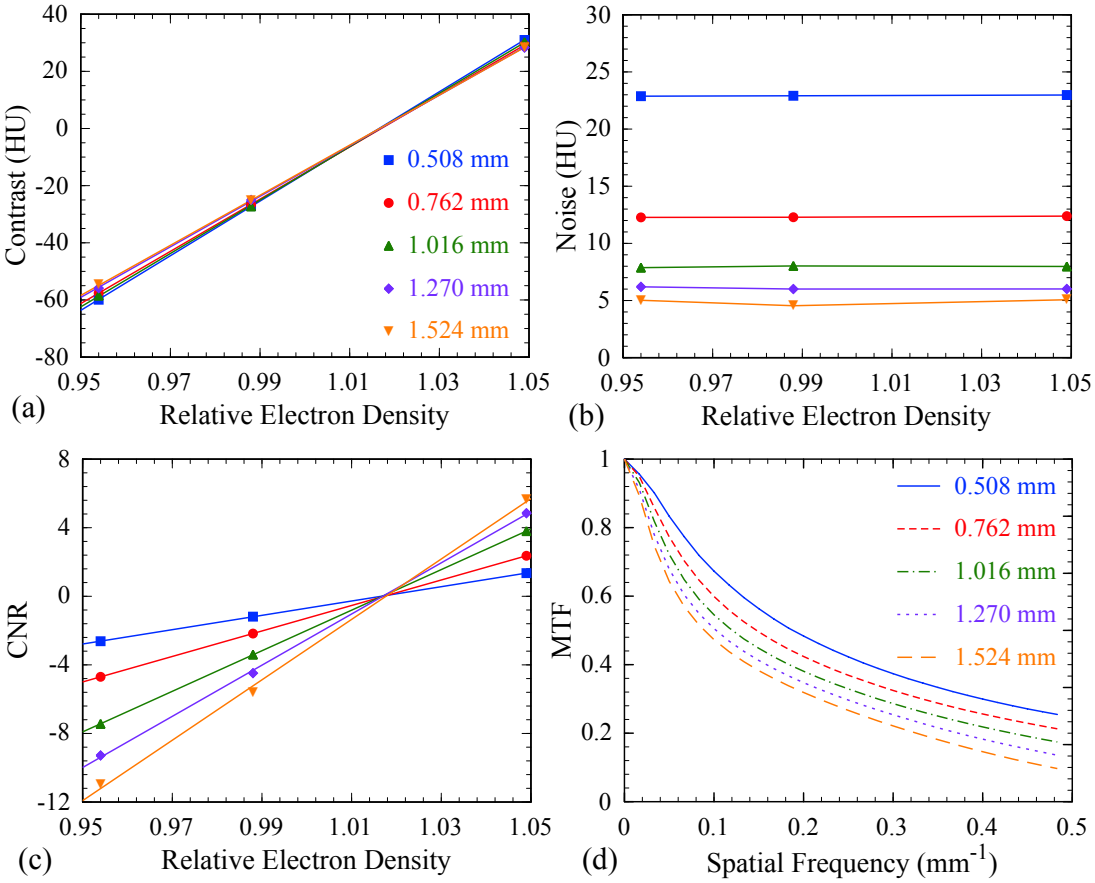

Figure 3.8. Simulation results obtained using the hybrid model for hypothetical 1.13 cm thick BGO scintillator designs with varying element pitches for (a) *Contrast*, (b) *Noise*, and (c) *CNR*. The results are plotted as a function of electron density of tissue-equivalent inserts relative to water. (d) Simulated results for MTF for those designs. Note that the lines appearing in the *Contrast* and *CNR* plots represent linear fits to the results.

III.D. Optimization of scintillator design

The complexities of how scintillator design affects CNR and spatial resolution performance makes it of interest to identify those regions in the continuum of design

offering the best achievable combination of CNR and MTF (referred to as optimum performance in this chapter). Toward this objective, these two performance metrics were determined using the hybrid model for scintillator designs with pitches ranging from 0.508 to 1.524 mm and thicknesses ranging from 0.5 to 6 cm, and the results are shown in the form of bar charts in Figs. 3.9(a) and 3.9(b). As seen in Fig. 3.9(a), the behavior of *CNR*-slope with increasing thickness is complex. For pitches 1.016 mm and greater, *CNR*-slope increases throughout the range, but with diminishing returns beyond ~3 cm. For smaller pitches of 0.508 and 0.762 mm, *CNR*-slope increases up to thicknesses of ~4 and 5 cm, respectively, before slightly decreasing – a result of the significant contribution of optical Swank noise for designs with high aspect ratio crystals. The behavior of spatial resolution, defined in this instance as the spatial frequency at which MTF drops to 0.5 (f_{50}), is simpler, as observed in Fig. 3.9(b). For all pitches considered, performance degrades with increasing thickness in an asymptotic manner.

A method for finding regions of design offering optimum performance is illustrated in Fig. 3.9(c), where contour lines of iso-*CNR*-slope and iso-f_{50} are plotted, based upon the results reported in Figs. 3.9(a) and 3.9(b) and employing a spline interpolation between data points. In the figure, the iso-*CNR*-slope lines represent values ranging from 39.5 to 235.9 at intervals of 10.3 while the iso-f_{50} lines represent values ranging from 0.0736 to 0.2101 mm^{-1} at intervals of 0.00455 mm^{-1}. (Note that the arrows superimposed on the contour lines indicate the direction of increasing value for each of *CNR*-slope and f_{50}.) The determination of optimum performance

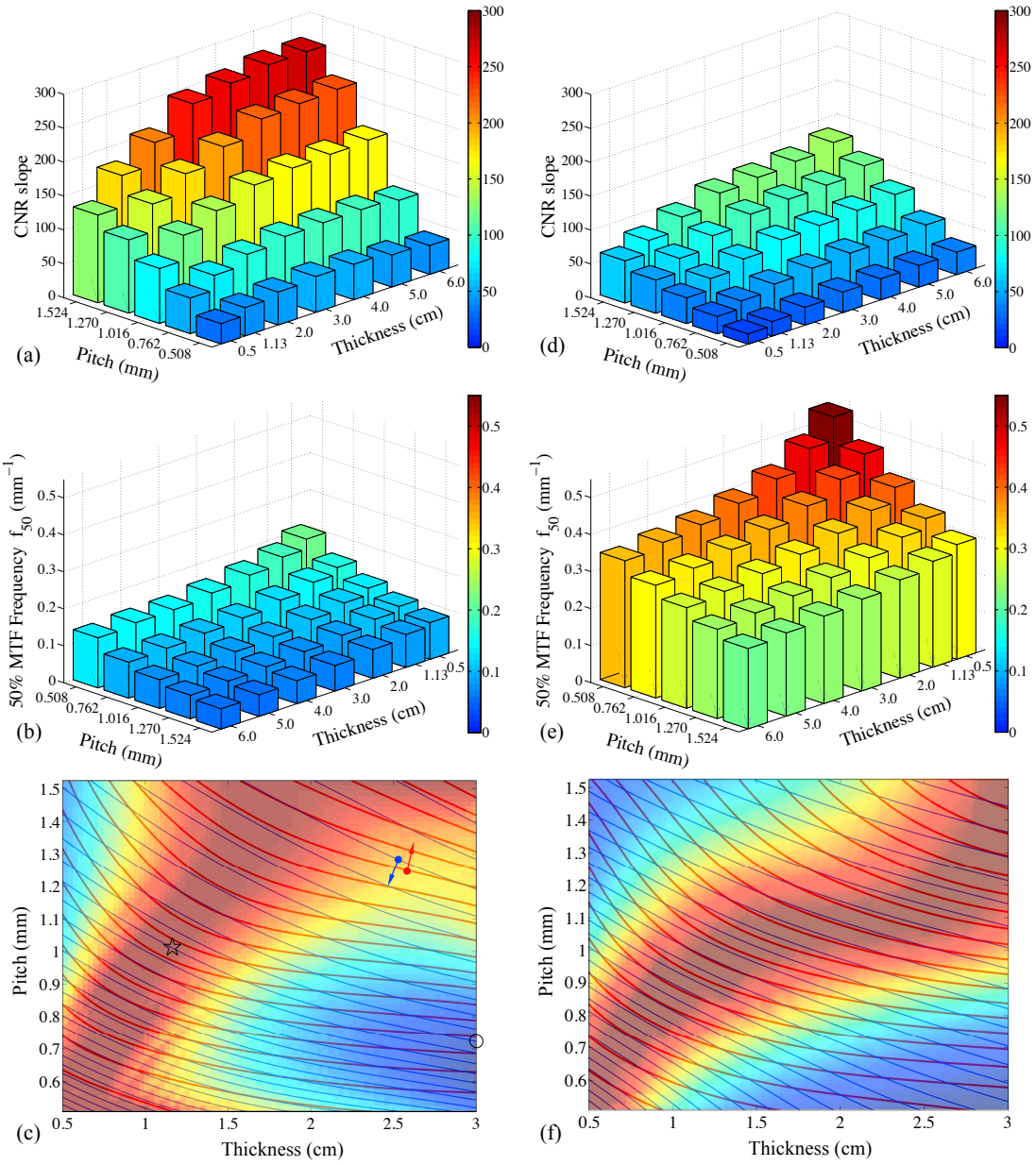

Figure 3.9. Simulation results obtained using the hybrid model for (a) *CNR*-slope, (b) 50% MTF frequency, f_{50}, and (c) contour lines of iso-*CNR*-slope (red lines) and iso-f_{50} (blue lines) along with an overlying optimization map, as a function of the pitch and thickness of various hypothetical scintillator designs. Corresponding results obtained using radiation transport simulation only are plotted in (d), (e) and (f). Note that, for purposes of enhanced presentation, the direction for increasing values of element pitch and scintillator thickness is reversed between the *CNR*-slope and f_{50} plots.

entailed finding the location corresponding to the highest value of f_{50} along a given line of iso-*CNR*-slope or, equivalently, finding the location corresponding to the highest value of *CNR*-slope along a given line of iso-f_{50}. The degree of optimization (i.e., proximity to optimum performance) is indicated by means of a color spectrum where hotter colors represent regions of superior performance. In this color map, results were presented only up to a thickness of 3 cm since, for larger thicknesses, regions of optimum performance occur at pitches larger than the upper limit of 1.524 mm.

Information of the type given in Fig. 3.9(c) provides insight that can guide decision-making in scintillator design. For example, at an element pitch of 0.8 mm (which approximately corresponds to the pitch presently used in conventional MV AMFPIs), optimum performance is achieved for a scintillator thickness of ~0.9 cm. For thicker scintillators employing the same pitch of 0.8 mm, the improvement in *CNR*-slope is relatively minor whereas the degradation in spatial resolution is more significant, as indicated by the shallower slopes of the iso-*CNR*-slope lines compared to the steeper slopes of the iso-f_{50} lines. The map also illustrates the impact of a tradeoff between element pitch and scintillator thickness. For example, while a scintillator design with a pitch of ~0.72 mm and a thickness of 3 cm (indicated by a circle symbol) provides the same f_{50} as a design with a pitch of 1.016 mm and a thickness of ~1.13 cm (indicated by a star symbol and corresponding to the BGO prototype), *CNR* performance is slightly inferior, as indicated by the corresponding contour lines. This demonstrates that choosing a much thicker (and thus more costly)

scintillator to improve x-ray detection efficiency, while reducing pitch to preserve spatial resolution, is not necessarily an effective strategy.

The results of a parallel analysis involving simulation of radiation transport only – conceptually corresponding to the performance of "ideal" scintillators exhibiting no optical Swank noise or optical blur – are shown in Figs. 3.9(d) to 3.9(f). In this case, compared to the results shown in Figs. 3.9(a) and 3.9(b), the values appearing in 3.9(d) and 3.9(e) are systematically lower for *CNR*-slope and higher for f_{50}, largely due to the absence of optical blur. Also, the behavior of *CNR*-slope with increasing thickness demonstrates a much simpler trend, consisting of a monotonic increase with diminishing returns beyond ~3 cm. In the optimization map shown in Fig. 3.9(f), the iso-*CNR*-slope lines represent levels ranging from 19.8 to 110.7 at intervals of 4.55, and iso-f_{50} lines represent levels ranging from 0.258 to 0.535 mm^{-1} at intervals of 0.00925 mm^{-1}. Compared to the results shown in Fig. 3.9(c), the map in Fig. 3.9(f) exhibits a noticeably different pattern for optimum performance – with thicker scintillators more strongly favored for pitches greater than ~0.9 mm. Note that from an examination of the individual contributions of optical Swank noise and optical blur, it is found that both effects significantly contribute to shifting optimum performance toward thinner scintillator designs. For Swank noise this outcome is simply due to an accelerating decrease in CNR-slope as scintillator thickness increases. In the case of blur, it is a consequence of opposing trends of more significant degradation of spatial resolution compared to relatively moderate improvement of CNR-slope as scintillator thickness increases. Comparison of results

which are based on simulations employing optical parameters obtained from actual prototypes (such as those in Fig. 3.9(c)), with results which correspond to optically ideal scintillators (such as those in Fig. 3.9(f)), can provide valuable insight for improving the optical properties of segmented scintillator designs.

IV. SUMMARY AND DISCUSSION

Thick, segmented scintillators represent a promising replacement for the type of phosphor screens employed in current MV AMFPIs for radiation therapy by virtue of offering order of magnitude improvement in DQE. This significant improvement greatly facilitates soft-tissue visualization at low dose using MV CBCT. In order to maximize the clinical benefit of these scintillators, it is important to optimize their performance through judicious choice of design parameters such as scintillator thickness and element pitch. Toward achieving this goal, a theoretical study exploring the performance of various BGO scintillator designs in terms of contrast-to-noise ratio and modulation transfer function has been reported. The study employs a novel hybrid modeling technique which takes into account both radiation and optical effects.

For a given scintillator design, the hybrid technique employs images obtained from Monte Carlo simulation of radiation transport in combination with an optical gain distribution and PSF obtained from Monte Carlo simulation of optical transport. While parameter values for the radiation transport simulation are readily available, those for optical transport need to be determined for the scintillator material, side

surfaces (i.e., septal walls) as well as top and bottom surfaces of the crystal elements. These optical parameter values could, in principle, be determined using direct, independent optical measurements on each component, although the multitude of surface properties (absorptivity, roughness and transmittance) that needs to be considered constitutes a challenge. In this chapter, realistic values for these parameters were obtained through fitting simulated optical MTFs to their empirical counterparts which were extracted from measured results obtained from a prototype BGO segmented scintillator with a thickness of ~1.13 cm. Of course, these values are specific to the form of the optical model chosen for the current study – so that changes to the model could result in different sets of parameters and values.

The inclusion of optical effects by means of a simulated optical gain distribution and PSF, as opposed to directly simulating the transport of the individual optical photons generated by each X ray interacting in the scintillator, offers a number of advantages. The consolidation of optical transport into a single optical simulation that is decoupled from the radiation transport results in significant reduction in the computational time per design required for the optical simulations – which allows examination of a far greater range of scintillator designs than would otherwise be practical. This reduction originates from the fact that the time necessary for simulating an optical gain distribution and PSF is dose-independent, requiring only on the order of 10^8 optical photon histories per design, whereas the time needed to perform a conventional Monte Carlo optical transport simulation scales linearly with the dose in addition to requiring a number of optical photon histories consistent with

the light yield of the scintillator. Another advantage of decoupling the optical effects from the radiation transport is the flexibility of performing repeated calculations of the optical gain distribution and PSF (for example to examine the effect of varying the values of the optical parameters) without having to repeat the radiation simulation.

In this study, the rectangular cuboid crystal shape assumed for the various hypothetical scintillator designs was chosen since it is considerably more practical to manufacture than focused shapes. However, this makes the reported performance results subject to the effects of beam divergence.[23] While those effects are generally small as a result of the relatively limited detection area considered in the simulations (which restricted the maximum divergence angle to 3°), they nevertheless do contribute to more lateral spread of radiation energy. For locations further off the central beam axis, divergence effects would of course be more pronounced, reducing MTF (particularly for thicker detectors), and leaving *CNR* unaffected since noise is not affected by beam divergence.[23] In this case, regions of optimum performance would be shifted toward thinner scintillators than those indicated in Fig. 3.9(c) – due to significant degradation of spatial resolution.[23] However, the use of focused scintillators would largely restore spatial resolution (as discussed in Chapter 2), resulting in a performance optimization map similar to that of Fig. 3.9 (c).

While the present study focuses on two dimensional matrices of optically isolated scintillating crystals for CBCT imaging at 6 MV, the hybrid modeling technique described in this chapter could be applied to other situations. For example,

it would be anticipated that optimization of such detectors for lower megavoltage energies realized through use of low-Z target materials [24-27] would favor designs with thinner crystals. Alternatively, the methodology could be applied toward the design of detectors required for other imaging geometries, such as fan-beam configurations of the type used in Tomotherapy treatment machines. In this case, the reduced level of scattered radiation would also be expected to favor thinner crystals.

It is interesting to note how the optical parameters employed in this study affect scintillator performance. For example, the 8% absorptivity used in the study has a detrimental effect on optical Swank noise for thicker scintillators since Swank noise is highly dependent on the efficiency of light transport within the scintillator. Another example is that light transmission through septal walls results in progressively more spatial resolution degradation as scintillator thickness increases. Both wall absorption and transmission diminish the benefit of improved quantum detection efficiency provided by thicker scintillators, prompting the need for careful performance optimization of scintillator design. For segmented scintillators with highly transparent crystals, relatively low absorption in the septal walls, and a low aspect ratio for the crystals, optical Swank noise has negligible effect on total image noise. This situation applies in the case of the prototype BGO scintillator, since BGO material has an optical mean free path length of ~30 cm and the prototype has a crystal aspect ratio of only ~11. Therefore, for this prototype, the inclusion of optical Swank noise in the hybrid modeling technique had a minor effect on the simulation results, as is demonstrated by the close agreement between the simulated and

empirical noise performance – an agreement that is largely a result of the inclusion of optical blur. For designs with thicker scintillators (up to 6 cm) and smaller pitches (down to 0.508 mm), the corresponding increase in the aspect ratio of the crystals significantly increases Swank noise [22] – resulting in a less pronounced increase in CNR as a function of increasing scintillator thickness, and even a decrease of CNR for designs with the largest aspect ratios. For segmented scintillators with better septal wall properties (i.e., lower absorption and lower transmission), the effects of Swank noise and optical blur are expected to be less important, resulting in a performance optimization that would more closely approach the ideal scintillator behavior shown in Fig. 3.9(f).

In the current study, the use of the MTF metric associated with 2D imaging system spatial resolution provided a computationally practical means to evaluate the performance of hypothetical segmented scintillator designs – in the spirit of providing insight about how the trade-offs in contrast-to-noise ratio and resolution are affected by basic design parameters. Beyond this study, it would be instructive to examine the effect of scintillator design upon 3D spatial resolution – which would entail accounting for factors beyond the pitch and thickness of the scintillator. Previous empirical and theoretical investigations of 3D spatial resolution for CBCT systems [28-30] have demonstrated that 3D MTF depends upon many factors such as: the details of the reconstruction algorithm (including the choice of filter), the voxel size, the number of projection images, the magnification factor, the position and direction of MTF analysis within the reconstructed volume, and scatter from the phantom or

patient. Depending upon the decisions made to account for these many additional details, the shape of the resulting optimization maps compared to those of the present study could well be affected. Finally, it should be noted that the computation time required for such a simulation study of 3D resolution would, of itself, be significantly greater than that of the entire present study.

REFERENCES – CHAPTER 3

[1] Y. Wang, L. E. Antonuk, Q. Zhao, Y. El-Mohri and L. Perna, "High-DQE EPIDs based on thick, segmented BGO and CsI:Tl scintillators: Performance evaluation at extremely low dose," Medical Physics **36**, 5707-5718 (2009).

[2] Y. El-Mohri, L. E. Antonuk, Q. Zhao, R. B. Choroszucha, H. Jiang and L. Liu, "Low-dose megavoltage cone-beam CT imaging using thick, segmented scintillators," Physics in Medicine and Biology **56**, 1509-1527 (2011).

[3] Y. El-Mohri, L. E. Antonuk, R. B. Choroszucha, Q. Zhao, H. Jiang and L. Liu, "Optimization of the performance of segmented scintillators for radiotherapy imaging through novel binning techniques," Physics in Medicine and Biology **59**, 797 (2014).

[4] M. F. Fast, T. Koenig, U. Oelfke and S. Nill, "Performance characteristics of a novel megavoltage cone-beam-computed tomography device," Physics in Medicine and Biology **57**, N15-N24 (2012).

[5] D. Létourneau, J. W. Wong, M. Oldham, M. Gulam, L. Watt, D. A. Jaffray, J. H. Siewerdsen and A. A. Martinez, "Cone-beam-CT guided radiation therapy: technical implementation," Radiotherapy and Oncology **75**, 279-286 (2005).

[6] J. Siewerdsen, M. Daly, B. Bakhtiar, D. Moseley, S. Richard, H. Keller and D. Jaffray, "A simple, direct method for x-ray scatter estimation and correction in digital radiography and cone-beam CT," Medical Physics **33**, 187-197 (2006).

[7] Y. Wang, L. E. Antonuk, Y. El-Mohri, Q. Zhao, A. Sawant and H. Du, "Monte Carlo investigations of megavoltage cone-beam CT using thick, segmented scintillating detectors for soft tissue visualization," Medical Physics **35**, 145-158 (2008).

[8] M. Loubele, F. Maes, R. Jacobs, D. van Steenberghe, S. White and P. Suetens, "Comparative study of image quality for MSCT and CBCT scanners for dentomaxillofacial radiology applications," Radiation protection dosimetry **129**, 222-226 (2008).

[9] N. Mail, D. Moseley, J. Siewerdsen and D. Jaffray, "The influence of bowtie filtration on cone-beam CT image quality," Medical Physics **36**, 22-32 (2009).

[10] C. Beltran, R. Lukose, B. Gangadharan, A. Bani-Hashemi and B. A. Faddegon, "Image quality & dosimetric property of an investigational Imaging Beam Line MV-CBCT," J. Appl. Clin. Med. Phys. **10**, 37-48 (2009).

[11] C. Ling, P. Zhang, T. Etmektzoglou, J. Star-lack, M. Sun, E. Shapiro and M. Hunt, "Acquisition of MV-scatter-free kilovoltage CBCT images during RapidArc™ or VMAT," Radiotherapy and Oncology **100**, 145-149 (2011).

[12] D. Sheikh-Bagheri, Ph.D. Thesis, Carleton University, 1999.

[13] H. Fujita, D. Tsai, T. Itoh, K. Doi, J. Morishita, K. Ueda and A. Ohtsuka, "A simple method for determining the modulation transfer function in digital radiography," IEEE Trans. Med. Imag. **11**, 34-39 (1992).

[14] A. Sawant, L. E. Antonuk, Y. El-Mohri, Q. Zhao, Y. Wang, Y. Li, H. Du and L. Perna, "Segmented crystalline scintillators: Empirical and theoretical investigation of a high quantum efficiency EPID based on an initial

engineering prototype CsI(Tl) detector," Medical Physics **33**, 1053-1066 (2006).
[15] R. K. Swank, "Absorption and noise in x-ray phosphors," J. Appl. Phys. **44**, 4199-4203 (1973).
[16] I. Kawrakow and D. W. O. Rogers, "The EGSnrc Code System: Monte Carlo Simulation of Electron and Photon Transport," Technical Report PIRS–701, National Research Council of Canada, Ottawa, Canada (2000).
[17] I. Kawrakow, "egspp: the EGSnrc C++ class library," Technical Report PIRS-899, National Research Council of Canada, Ottawa, Canada (2005).
[18] Y. El-Mohri, K.-W. Jee, L. E. Antonuk, M. Maolinbay and Q. Zhao, "Determination of the detective quantum efficiency of a prototype, megavoltage indirect detection, active matrix flat-panel imager," Medical Physics **28**, 2538-2550 (2001); Erratum: Med. Phys. **33**, 251 (2006).
[19] S. Agostinelli, et al., "GEANT4–a simulation toolkit," Nucl. Instrum. Meth. A **506**, 250-303 (2003).
[20] P. Lecoq, P. Li and B. Rostaing, "BGO radiation damage effects: optical absorption, thermoluminescence and thermoconductivity," Nucl. Instrum. Meth. A **300**, 240-258 (1991).
[21] M. Born and E. Wolf, *Principles of optics: electromagnetic theory of propagation, interference and diffraction of light*. (CUP Archive, 1999).
[22] Y. Wang, L. E. Antonuk, Y. El-Mohri and Q. Zhao, "A Monte Carlo investigation of Swank noise for thick, segmented, crystalline scintillators for radiotherapy imaging," Medical Physics **36**, 3227-3238 (2009).
[23] Y. Wang, Y. El-Mohri, L. E. Antonuk and Q. Zhao, "Monte Carlo investigations of the effect of beam divergence on thick, segmented crystalline scintillators for radiotherapy imaging," Physics in Medicine and Biology **55**, 3659-3673 (2010).
[24] B. A. Faddegon, V. Wu, J. Pouliot, B. Gangadharan and A. Bani-Hashemi, "Low dose megavoltage cone beam computed tomography with an unflattened 4 MV beam from a carbon target," Medical Physics **35**, 5777-5786 (2008).
[25] R. T. Flynn, J. Hartmann, A. Bani-Hashemi, E. Nixon, R. Alfredo, C. Siochi, E. C. Pennington and J. E. Bayouth, "Dosimetric characterization and application of an imaging beam line with a carbon electron target for megavoltage cone beam computed tomography," Medical Physics **36**, 2181-2192 (2009).
[26] J. L. Robar, T. Connell, W. Huang and R. G. Kelly, "Megavoltage planar and cone-beam imaging with low-Z targets: Dependence of image quality improvement on beam energy and patient separation," Medical Physics **36**, 3955-3963 (2009).
[27] D. Sawkey, M. Lu, O. Morin, M. Aubin, S. Yom, A. Gottschalk, A. Bani-Hashemi and B. Faddegon, "A diamond target for megavoltage cone-beam CT," Medical Physics **37**, 1246-1253 (2010).
[28] A. L. C. Kwan, J. M. Boone, K. Yang and S.-Y. Huang, "Evaluation of the spatial resolution characteristics of a cone-beam breast CT scanner," Medical Physics **34**, 275-281 (2007).

[29] K. Yang, A. L. C. Kwan and J. M. Boone, "Computer modeling of the spatial resolution properties of a dedicated breast CT system," Medical Physics **34**, 2059-2069 (2007).

[30] J.-P. Bissonnette, D. J. Moseley and D. A. Jaffray, "A quality assurance program for image quality of cone-beam CT guidance in radiation therapy," Medical Physics **35**, 1807-1815 (2008).

CHAPTER 4

DESIGN AND PERFORMANCE OF A KV/MV DUAL ENERGY AMFPI FOR RADIOTHERAPY IMAGING

I. INTRODUCTION

Motivated by the promising performance of MV AMPFIs incorporating segmented scintillators as well as by ongoing research interest in a kV beam (or a low-energy MV beam with a greater kV component)[1, 2] with the same field-of-view (FOV) as that of the treatment beam, it is of interest to explore the possibility of performing both kV and MV imaging using a single imaging detector. In this chapter, considerations for the design of such a dual energy imager are explored through examination of the performance of a variety of hypothetical AMFPIs based on x-ray converters employing the segmented scintillator approach. The performance of such imagers is characterized through simulation modeling in terms of contrast, noise and CNR using volumetric (CBCT) imaging, as well as MTF, Swank factor and signal using planar imaging.

II. METHODS

II.A. Converter designs examined in the study

Each converter design consists of a 2D matrix of identical elements

comprising rectangular cuboid-shaped, scintillating crystals optically isolated by 0.05 mm thick, polystyrene septal walls. (Thus, as in Chapter 3, the elements in each converter are not focused toward the radiation source.) All designs employ BGO material with thicknesses ranging from 0.25 to 4 cm, and element-to-element pitches (referred to as converter pitches) ranging from 0.508 to 1.016 mm. BGO was chosen due to the promising performance exhibited by previous prototypes based on this material, which offers desirable properties such as high electron density, high refractive index, and high optical transparency.[3-5] The lower limit for thickness corresponds to a point where the QE for MV imaging is ~15%, representing a substantial improvement compared to that of conventional MV AMFPIs, whereas the 4 cm upper limit (for which the QE is ~80%) corresponds to a point beyond which the rate of improvement in QE as a function of thickness diminishes rapidly. The lower limit for pitch corresponds to a point below which the scintillator fill factor drops sharply (due to the volume occupied by the fixed septal wall thickness), while the upper limit roughly corresponds to a point beyond which the advantageous spatial resolution offered by kV imaging would be severely compromised. Note that the 1 mm copper plate commonly employed as a build-up layer in the converter of conventional portal imagers was eliminated to avoid the detrimental effect of filtering of low energy X rays that provide high contrast in kV imaging. (The performance of an MV imaging system operated in the absence of an overlying metal plate has been previously examined.)[6-8] Also note that a reflector with negligible radiation attenuation was introduced to provide desirable optical properties and was modeled in the simulation with a zero mass attenuation coefficient for traversing X rays. Two

extreme cases for the reflector were examined: one with 100% absorptivity and 0% reflectivity (referred to as "black"), and the other with 0% absorptivity and 100% reflectivity (referred to as "mirror").

The AMFPI array was modeled as an ~1 mm thick barium-doped glass plate representing the array substrate [9] while the ~1 μm thick pixel circuitry fabricated on the substrate was ignored due to its negligible effect on radiation attenuation. The array was coupled to the side of the converter opposite to that where the reflector resides. The optical coupling efficiency of the photodiode was assumed to be 58% for light emitted by BGO. Throughout the study, the pixel pitch of the array was assumed to be the same as the converter pitch.

In addition to the two reflector types, the positioning of the array and the reflector relative to the x-ray source was also varied. In this chapter, the side of the converter facing the x-ray source is referred to as the *entrance* surface while the other side is referred to as the *exit* surface. Under kV imaging conditions, dose drops quickly with depth into the converter from the entrance surface, with most of the radiation stopping in the first ~2 mm while, for an MV beam, dose is deposited more evenly throughout the thickness of the converter – as illustrated in Fig. 4.1. This significant difference in dose deposition requires careful design of the converter to preserve the respective benefits of both kV and MV imaging. Since energy deposition for kV photons is concentrated near the entrance surface, a conventional

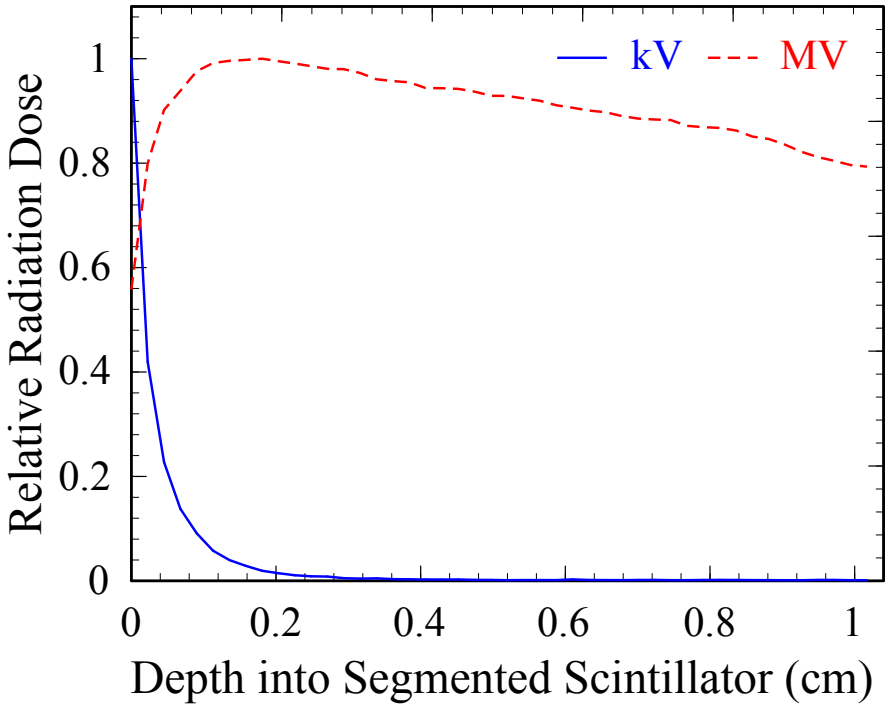

Figure 4.1. Radiation dose profiles corresponding to 100 kVp (solid line) and 6 MV (dashed line) beam spectra along the depth of an ~1 cm thick BGO converter, obtained using the same Monte Carlo simulation techniques described in section II.B.1. The dose values for each spectrum have been normalized to unity at their respective maxima. Note that, whereas the kV profile exhibits a sharp decrease with depth, the MV profile follows the familiar pattern associated with the depth-dose distribution for a treatment beam.[10]

front illumination configuration, where the array is coupled to the exit surface and the reflector to the entrance surface as illustrated in Fig. 4.2(a), would lead to significant lateral spread of those optical photons reaching the array. This lateral spread, which is a consequence of imperfections in the optical isolation between neighboring scintillator elements, results in degradation of spatial resolution – an effect which increases for progressively thicker converter designs.

One possible means to reduce this loss of spatial resolution is through use of a *rear illumination* configuration [11-14] in which the array is coupled to the entrance

surface and the reflector to the exit surface of the converter, as shown in Fig. 4.2(b). In this configuration, for kV imaging, the majority of the optical photons generated in the direction of the array traverse much shorter distances before being detected, thereby reducing lateral optical spread and preserving spatial resolution of the imager. In the case of MV imaging, there is a parallel, though much reduced, benefit – due to the more uniform distribution of absorbed energy across the scintillator, as illustrated in Fig. 4.1.

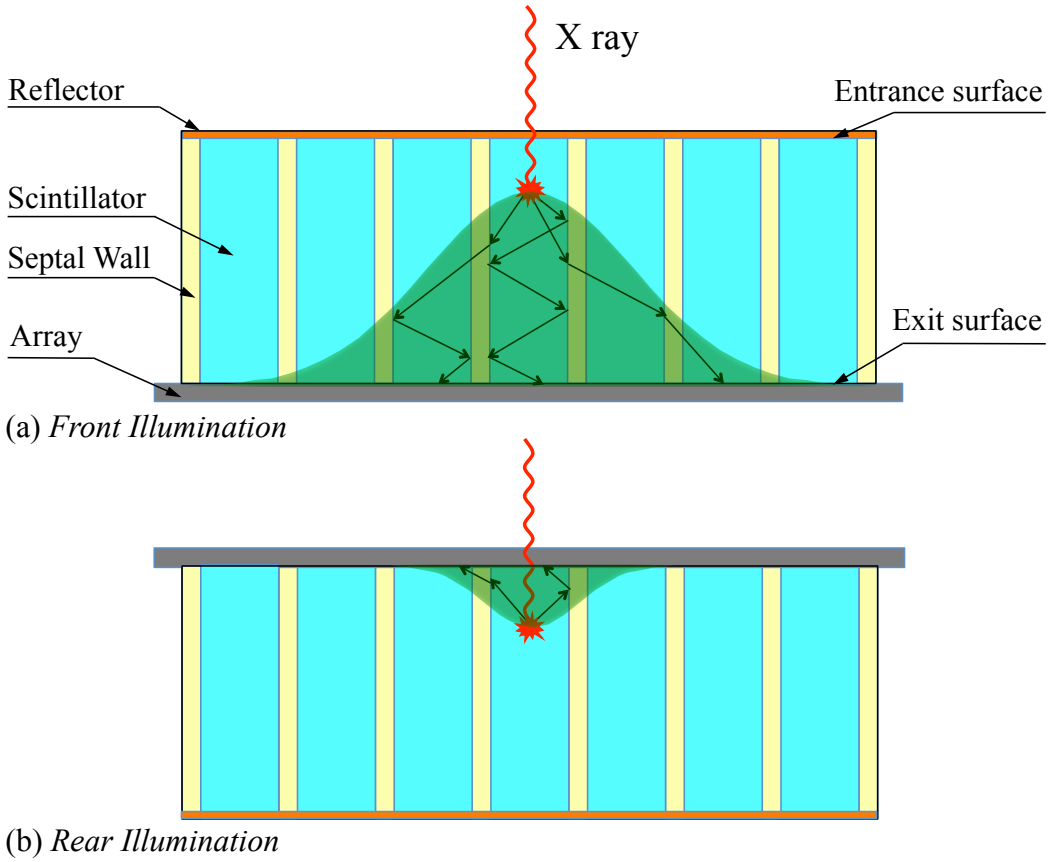

(a) *Front Illumination*

(b) *Rear Illumination*

Figure 4.2. Schematic, cutaway diagrams of imagers based on converters employing a segmented scintillator illustrating (a) front and (b) rear illumination configurations. The transparent bell-shaped regions superimposed on the diagrams signify the approximate lateral spread of optical photons reaching the array under kV imaging conditions. The arrows appearing in these regions correspond to examples of possible trajectories of optical light photons reaching the array.

For each converter of a certain thickness and pitch, a total of four configurations were explored: front illumination with a black reflector (referred to as "*front-black*"), front illumination with a mirror reflector ("*front-mirror*"), rear illumination with a black reflector ("*rear-black*"), and rear illumination with a mirror reflector ("*rear-mirror*").

II.B. Simulation framework

To characterize the MTF and CNR of the imager, the Monte Carlo-based hybrid modeling technique reported in Chapter 3 was employed. In addition, the effect of electronic additive noise was introduced through an analytical circuit noise model. A flowchart illustrating the major implementation steps of this coupled framework is shown in Fig. 4.3 and is described below.

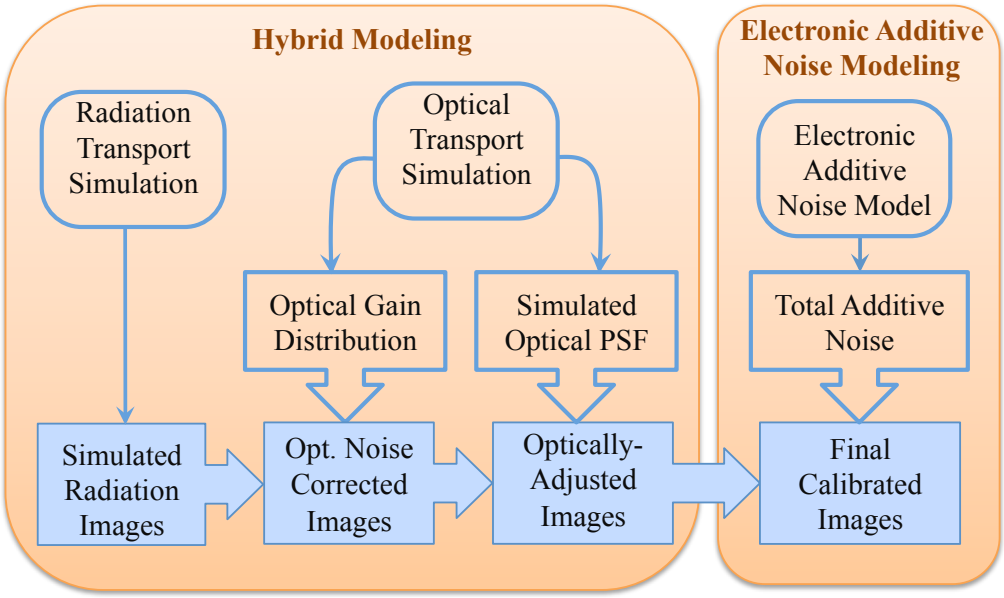

Figure 4.3. Flowchart illustrating the simulation framework consisting of hybrid modeling (box on the left) and electronic additive noise modeling (box on the right) used in the study.

II.B.1 Hybrid model

Radiation transport of X rays and optical transport of optical photons generated inside the scintillator were simulated using the hybrid modeling technique described in Chapter 3. This technique decouples radiation and optical transport simulations and condenses the more computationally expensive optical simulation part into a single optical simulation per converter design. As diagrammatically summarized on the left of Fig. 4.3, it entails a sequential process where radiation images (obtained from radiation transport simulations) are corrected with optical gain distributions and optical point spread functions (PSF) (both obtained from optical transport simulations) to account for optical Swank noise and optical blur, respectively.

Monte Carlo radiation transport simulations were performed using the EGSnrc code,[15] with the geometries of the converters and the contrast phantom modeled using the EGSnrc C++ class library (egspp),[16] and with the egspp user code, as well as the input file that defines the geometry, modified as necessary. The parameter settings and algorithm options in the code that were employed in the study follow those used in previous theoretical investigations.[3] Both kV and MV simulations employed a point source located 130 cm away from the entrance surface of the converter. The kV spectrum corresponds to that of the 100 kVp "standard head" protocol of a Varian On-Board Imager (OBI) and was described using the TASMIP model,[17] with the tube voltage set to 100 kV and the intrinsic filtration set to 1.45 mm aluminum. A 6 MV spectrum corresponding to that of a Varian radiotherapy linear accelerator was

adopted for MV simulations.[18]

The optical transport simulations were performed using the Geant4 package.[19] The details and validation of the optical model, as well as the values for the associated optical parameters (which were obtained from a prototype segmented scintillator), appear in Chapter 3.

Both the radiation and optical transport Monte Carlo simulations were performed on a 64-bit Linux cluster with ~1000 processor cores (4.0 GHz AMD FX series). The study required a total of ~3.04 million CPU hours, with a large majority of the time spent on the radiation transport simulations.

II.B.2 Additive noise model

An analytical noise model was employed to account for the effect of electronic additive noise. The symbols in the following equations and the values of related parameters are summarized in Table 4.1. The model takes into account the two dominant components of additive noise, reset noise associated with the thermal noise of the TFTs in the array pixels ($\sigma_{TFT-thermal}$) and noise of the external preamplifier electronics (σ_{amp}). The TFT reset thermal noise can be calculated from [20]

$$\sigma_{TFT-thermal} = \frac{1}{q}\sqrt{2k_B T C_{pd}} \ (e^-), \tag{4.1}$$

where q is the electron charge, k_B is the Boltzmann Constant, T is room temperature in Kelvin, and C_{pd} is the photodiode capacitance of each array pixel. Following the parallel-plate capacitor model, the photodiode capacitance can be calculated from [21]

$$C_{pd} = \varepsilon_0 \varepsilon_{Si} \frac{A_{pd}}{d} = \varepsilon_0 \varepsilon_{Si} \frac{\eta a_{pix}^2}{d}, \quad (4.2)$$

where ε_0 is the vacuum permittivity, ε_{Si} is the relative static permittivity of silicon, A_{pd} is the area of the photodiode in each pixel, η is the optical fill factor of the array pixels, a_{pix} is the pixel pitch of the array, and d is the thickness of the photodiode. The array fill factor is assumed to be 100% – given the relatively large pixel pitches considered in the study.[22] The preamplifier noise was estimated using an expression based on the characteristics of a high performance preamplifier,[23]

$$\sigma_{amp} = 15 C_{data} + 285 \ (e^-). \quad (4.3)$$

Table 4.1. Symbols, definitions and values of the fixed parameters used in the electronic additive noise model. Note that the value used for photodiode thickness, d, corresponds to that of a modern array design (M13).[22]

Symbols	Definitions	Values
$\boldsymbol{\sigma_{TFT-thermal}}$	TFT reset thermal noise	
$\boldsymbol{\sigma_{amp}}$	Preamplifier noise	
$\boldsymbol{\sigma_{total}}$	Total additive noise	
$\boldsymbol{C_{data}}$	Data line capacitance	115 pF
$\boldsymbol{C_{pd}}$	Photodiode capacitance	
$\boldsymbol{A_{pd}}$	Photodiode area	
$\boldsymbol{a_{pix}}$	Array pixel pitch	
$\boldsymbol{d}$	a-Si layer thickness in photodiode	1.50 μm
$\boldsymbol{\varepsilon_0}$	Vacuum permittivity	8.85×10^{-12} F/m
$\boldsymbol{\varepsilon_{Si}}$	Relative static permittivity of silicon	12
$\boldsymbol{\eta}$	Array optical fill factor	100%
$\boldsymbol{q}$	Electron charge	1.60×10^{-19} C/e
$\boldsymbol{k_B}$	Boltzmann Constant	1.38×10^{-23} $m^2kg/(s^2K)$
$\boldsymbol{T}$	Room temperature	295 K

In this equation, the value of the data line capacitance (C_{data}) was conservatively estimated using the capacitance per unit length of an array with a large pixel pitch,[20] scaled to the data line length of typical MV AMFPIs (i.e., 40 cm).

The total additive noise, σ_{total}, was calculated using

$$\sigma_{total} = \sqrt{\sigma_{TFT-thermal}^2 + \sigma_{amp}^2} \ (e^-). \tag{4.4}$$

For each pitch examined in the study, a Gaussian distribution with zero mean and variance of σ_{total} was formed. For each pixel of the optically-adjusted images obtained from the hybrid modeling technique, the additive noise was introduced through random sampling according to that distribution, resulting in additive noise calibrated images, as indicated in Fig. 4.3.

II.C. Determination of CBCT imaging metrics

For the radiation transport simulation of CBCT imaging, a contrast phantom with dimensions, composition and inserts similar to those of a phantom used in a previous empirical study [4] was simulated under both kV and MV imaging conditions. The phantom consists of an 11.4 cm diameter, solid water cylinder with three 2.8 cm diameter, cylindrical tissue-equivalent inserts, all with a common length of 6 cm. Consistent with earlier studies reported in reference 4 and Chapter 3, the center of the phantom was positioned 124.2 cm from the source – thereby leaving a 1 mm gap between the converter and the bottom of the phantom. The inserts correspond to breast, solid water and brain with electron densities of 0.954, 0.988 and 1.049 relative to water, respectively. All converter designs have a detection area of ~70×140 mm^2,

resulting in matrix formats of 141×281, 95×189, and 71×141 for the examined pitches of 0.508, 0.762 and 1.016 mm, respectively. This converter area was chosen so as to be sufficiently large to allow imaging of the phantom. For a given converter design, imager configuration and imaging condition, 180 projection radiation images were obtained by scanning the phantom tomographically at 2° angular increment over 360°. For each tomographic scan, the x-ray fluence was 1.14×10^8 and 4.32×10^7 X rays/mm^2 at the entrance surface of the converter for kV and MV CBCT, respectively. The kV fluence provides a dose equivalent to the 145 mAs "standard head" protocol for the Varian OBI kV CBCT imaging system, while the MV fluence provides a dose equivalent to that used in a previous empirical MV CBCT study (corresponding to a minimum of one beam pulse per projection).[4] In addition, for each converter design, imager configuration and imaging condition, a set of 180 radiation flood images was obtained in the absence of the phantom, each using the same fluence as that used for the individual projection images of the phantom. Due to the distinctively different characteristics of the kV and MV dose profiles, a weighted central slice CT dose index ($CTDI_W$) was used as a surrogate for imaging dose for kV and MV CBCT in order to facilitate comparisons between the kV and MV CBCT image doses used in the study. $CTDI_W$ is defined as [24]

$$CTDI_W = \frac{1}{3}\sum D_C + \frac{2}{3}\sum D_P, \tag{4.5}$$

where the dose at two landmark locations, the center (D_C) and the periphery (D_P, defined at 1 cm inside the phantom surface), are summed over all projection angles in the tomographic scan. Based on this definition, the fluence values used in kV and

MV CBCT simulations correspond to $CTDI_W$ values of ~0.91 and ~3.0 cGy respectively.

For the optical transport simulation, the segmented scintillator in each converter design took the form of a matrix of 101×101 elements. For each design, 10,000 simulation runs, each consisting of 10,000 optical photon histories, were performed. All photons were generated in the central element of the matrix, following the 3D radiation energy deposition profile of the corresponding converter design. The optical gain distribution and optical PSF obtained from this simulation were applied to the simulated radiation images to yield optically adjusted images, which accounted for the effect of both optical Swank noise and optical blur, as detailed in Chapter 3. The optically adjusted images were then corrected for additive noise of the corresponding design to generate the final calibrated images.

A Feldkamp-based algorithm employing a ramp filter was used to reconstruct the volumetric images corresponding to the contrast phantom from a combination of the calibrated projection images and the average of the 180 calibrated flood images. The voxel pitch and single slice thickness used in the reconstruction were chosen to be equal to the converter pitch for each design. A suitable number of the reconstructed slices were binned to generate a slice thickness of ~5 mm, followed by a cupping artifact correction to remove the background trend caused by beam hardening.[4]

The CBCT performance of various converter designs was characterized in terms of contrast (*Contrast*), noise (*Noise*) and *CNR* of the tissue-equivalent inserts relative to the water-equivalent background in the reconstructed phantom images. *Contrast* for a given insert was calculated in Hounsfield units (HU) using the equation

$$Contrast = \frac{S_{obj} - S_{water}}{S_{water}} \times 1000 \text{ (HU)}, \tag{4.6}$$

where S_{obj} and S_{water} represent the mean signal in the insert and water-equivalent background, respectively. Each signal was taken from a circular region with a ~14.2 mm diameter that excluded the edges of the inserts and the phantom. *Noise* was calculated using the equation

$$Noise = \frac{\sigma_{obj}}{S_{water}} \times 1000 \text{ (HU)}, \tag{4.7}$$

where σ_{obj} represents the standard deviation of the signal in the insert. Finally, *CNR* was calculated from

$$CNR = \frac{S_{obj} - S_{water}}{\sigma_{obj}}. \tag{4.8}$$

II.D. Determination of imager MTF

The spatial resolution for each converter design was characterized in terms of the presampled MTF using the angled slit technique.[25] The radiation and optical transport simulation of MTF followed the steps described in Chapter 3, generating an optically adjusted slit image for each design. Additive noise was subsequently included to yield a final calibrated slit image. This image was used to determine an

oversampled line spread function, the 1D Fourier transform of which yielded the MTF.

II.E Determination of Swank factor and signal

The steps used to determine Swank factor and signal (accounting for contributions of both radiation and optical effects) largely followed those reported in reference 26. For each imager configuration and converter design, radiation transport simulation was performed using the EGSnrc code package, yielding a phase space file containing information for each energy deposition event within the converter for each interacting X ray. Using this phase space file, simulation of optical transport was subsequently performed using the Geant4 code package to tally the number of optical photons detected for each X ray in the form of a pulse height distribution. The Swank factor I and signal S were calculated using the equations [27]

$$I = \frac{M_1^2}{M_0 M_2}, \tag{4.9}$$

$$S = \frac{M_1}{M_0}, \tag{4.10}$$

where M_i is the i^{th} order moment of the pulse height distribution, $P(x)$

$$M_i = \sum_k x_k^i \, P(x_k). \tag{4.11}$$

III. RESULTS

III.A. Comparison of imager configurations

A comparison of the relative merits of the four imager configurations

described in Section II.A was performed through characterization of their MTF, Swank factor and signal performance under kV and MV imaging conditions. Figures 4.4 through 4.7 show results for the full range of converter thicknesses (0.25 to 4.0 cm) at a selected pitch of 1.016 mm – the same pitch as that of a prototype BGO segmented scintillator reported in a previous empirical study.[4]

Figure 4.4 shows the kV MTF results for the different imager configurations. As expected, the rear illumination results, shown in Figs. 4.4(b) and 4.4(d), exhibit

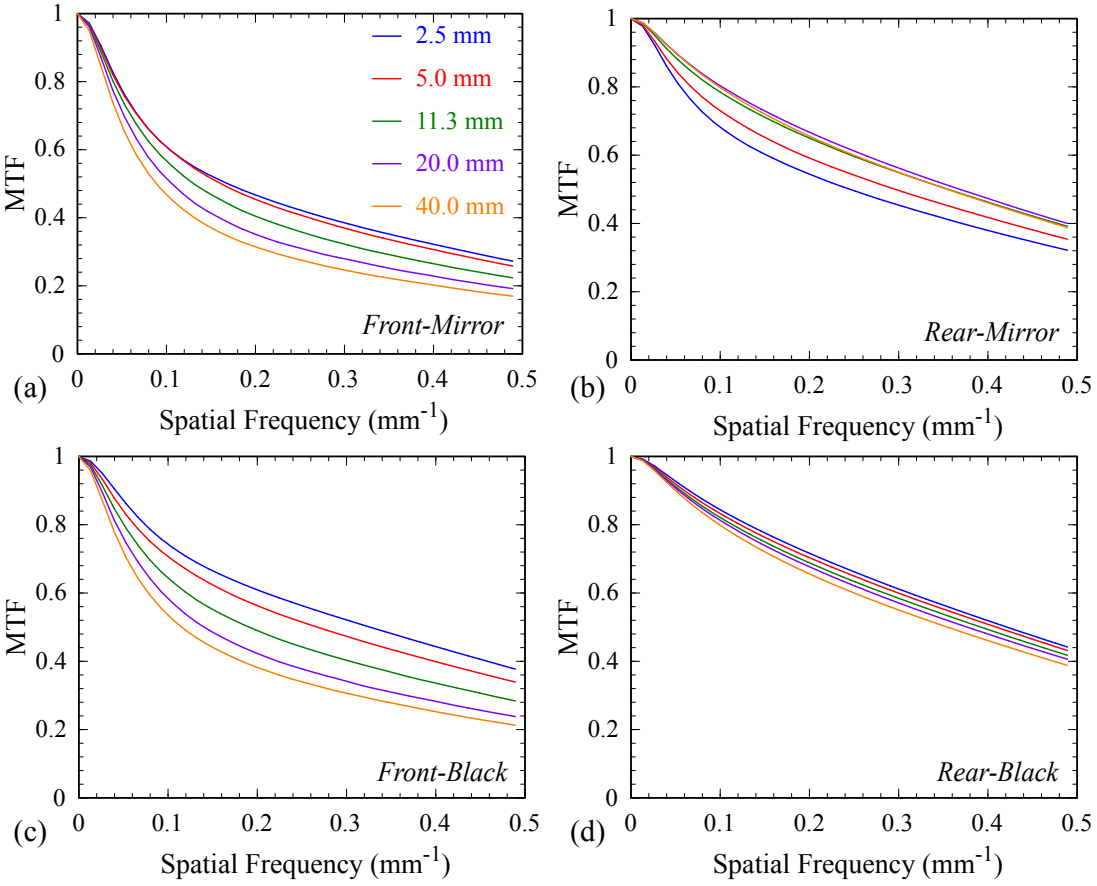

Figure 4.4. MTF results under kV imaging conditions for 1.016 mm pitch imagers employing various converter thicknesses for the (a) *front-mirror*, (b) *rear-mirror*, (c) *front-black*, and (d) *rear-black* configurations.

systematically higher MTF compared to that for the corresponding front illumination cases shown in Figs. 4.4(a) and 4.4(c). This is a consequence of reduced lateral optical spread for rear illumination, as schematically illustrated in Fig. 4.2. Note that, for all but the *rear-mirror* configuration, MTF improves with decreasing converter thickness due to reduced scatter of primary X rays and lateral spread of optical photons. However, for the *rear-mirror* configuration (Fig. 4.4(b)), the MTF generally degrades with decreasing thickness. This reversed behavior originates from the increasing fraction of optical photons that are reflected by the mirror reflector and reach the array as thickness decreases. Such photons tend to undergo more interactions with the septal walls, leading to more lateral spread which, in turn, results in deterioration of spatial resolution. The absence of such photons for the *rear-black* configuration results in systematically higher MTF compared to that for the *rear-mirror* configuration. In addition, for the *rear-black* configuration, the MTF curves are closely clustered and relatively insensitive to changes in converter thickness, allowing for the possibility of using a greater thickness to achieve higher detection efficiency in MV imaging without substantial degradation of kV spatial resolution.

As is apparent in Fig. 4.5(a), under kV conditions the rear illumination configurations (open symbols) provide better Swank factor than their front illumination counterparts (solid symbols). In addition, for a given converter thickness, *rear-black* and *rear-mirror* exhibit nearly identical Swank factors. The rear illumination configurations also provide generally higher signal than their front

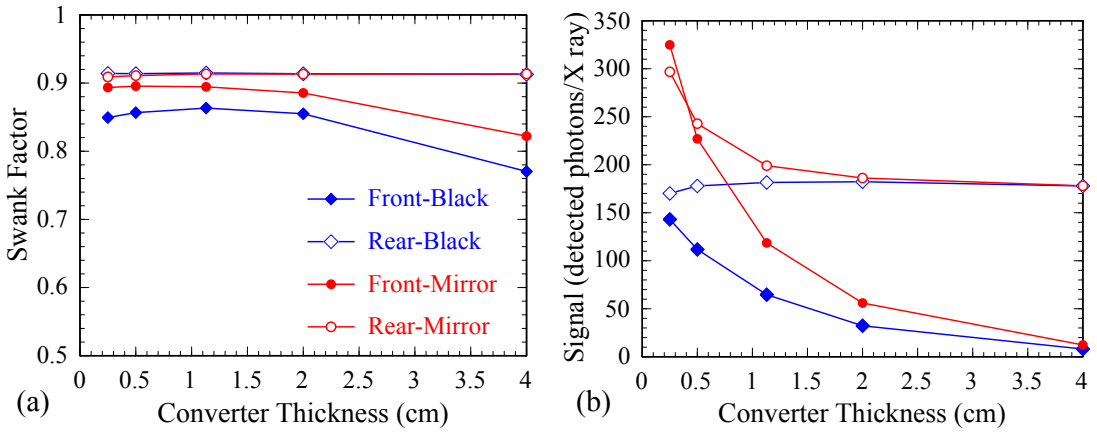

Figure 4.5. kV results for (a) Swank factor and (b) signal (defined as the average number of detected optical photon per interacting X ray) as a function of converter thickness for 1.016 mm pitch imagers.

illumination counterparts, as shown in Fig. 4.5(b). For all but the *rear-black* configuration, signal decreases with thickness due to the increased number of absorbed photons along a longer mean optical path length. However, for the *rear-black* configuration, signal is relatively independent of converter thickness – largely as a result of the negligible contribution from optical photons generated in material beyond ~0.25 cm. It is interesting to note that, for configurations with the same type (i.e., *mirror* or *black*) but different positioning of reflector (i.e., *front* and *rear*), signal values generally converge at smaller thicknesses – due to similarities in the mean optical path lengths for front and rear illumination. This similarity results from a relatively more uniform energy deposition, and therefore more uniform generation of optical photons, throughout the converter thickness for thinner converters. Conversely, for configurations with the same reflector positioning but different reflector types, signal values converge at larger thicknesses due to the diminished importance of reflector type, resulting from reduced numbers of photons reaching the

reflector. For example, for the two rear illumination configurations, although *rear-black* provides lower signal values than *rear-mirror* at smaller thicknesses, this signal difference quickly diminishes as thickness increases, resulting in a relative difference of only ~2% at 2 cm and a negligible difference at 4 cm. Since a greater thickness is advantageous for improved quantum efficiency for MV imaging, the adoption of a black reflector is not expected to significantly constrain signal compared to the mirror reflector.

Figure 4.6 shows MV MTF results for the various imager configurations. In all cases, MTF performance is seen to improve with decreasing converter thickness. In addition, for a given thickness, the *rear-black* configuration is seen to provide equivalent or higher MTF compared with the other three configurations. Figure 4.7 shows that, as in the kV case, the rear illumination configurations provide generally better MV Swank factor and signal performance than their front illumination counterparts. In Fig. 4.7(b), while signal increases toward an asymptotic limit as thickness increases for rear illumination, largely due to asymptotically increasing QE, for front illumination signal initially increases and then decreases due to the competing effects of increasing QE and decreasing optical collection efficiency. Note that the signal results in Fig. 4.7(b) exhibit the same general trends of convergence observed in the kV case. Considering the two reflector types for rear illumination, although *rear-black* provides lower Swank factor and signal than *rear-mirror*, the differences are small for thick converters, with relative differences of only ~4% and

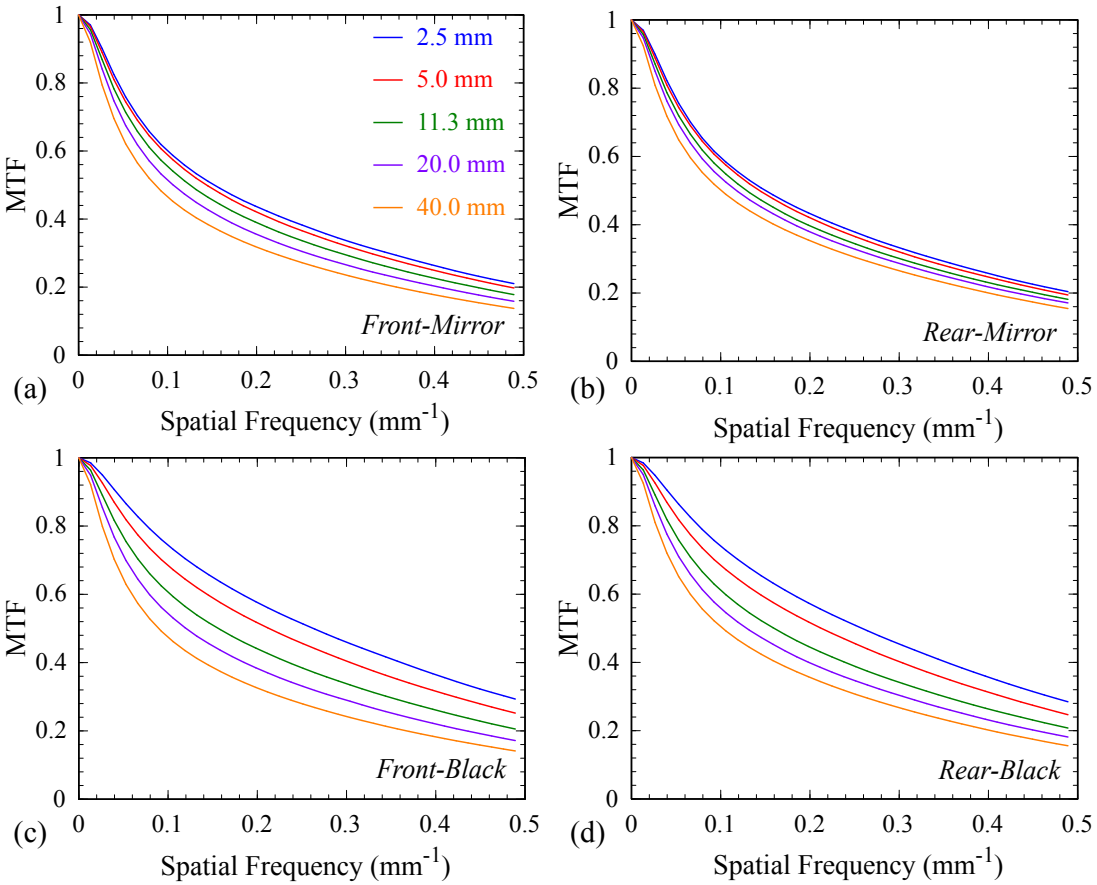

Figure 4.6. MTF results under MV imaging conditions for 1.016 mm pitch imagers employing various converters thicknesses for the (a) *front-mirror*, (b) *rear-mirror*, (c) *front-black*, and (d) *rear-black* configurations.

8% for Swank factor and signal, respectively, at a thickness of 2 cm, and negligible differences at 4 cm.

The results of the above analysis of MTF, Swank factor and signal suggest that the *rear-black* configuration represents the most favorable design choice for a converter intended for kV and MV operation. This conclusion applies throughout the range of converter pitches considered in the study, the results for which (though not shown) exhibit trends similar to those at 1.016 mm. For that reason, only the *rear-black* configuration is considered in the following sections.

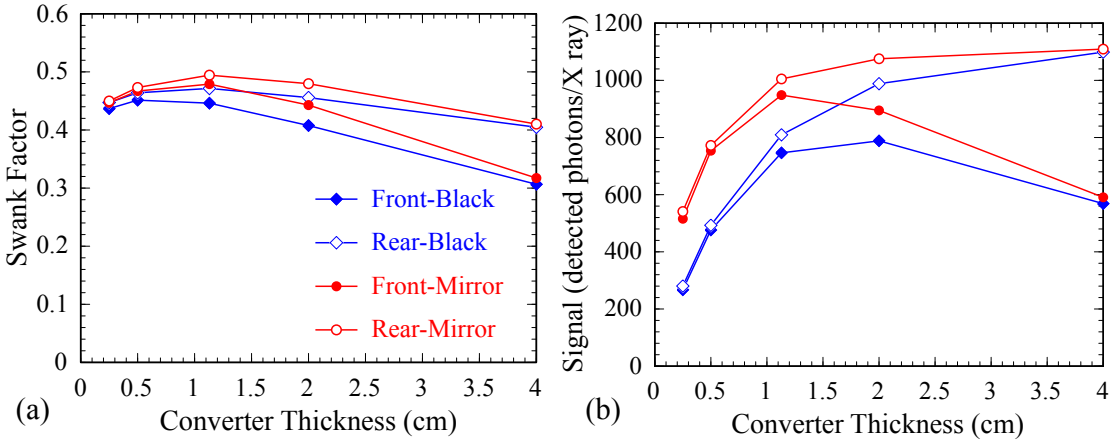

Figure 4.7. MV results for (a) Swank factor and (b) signal as a function of converter thickness for 1.016 mm pitch imagers.

III.B. Comparison of converter designs

CNR performance for CBCT imaging under kV and MV imaging conditions as a function of converter thickness and pitch is shown in Fig. 4.8. For a given thickness and imaging condition, CNR consistently increases with pitch as a result of reduced noise due to more x-ray quanta being detected by larger cross-sectional areas of scintillator elements. However, for a given pitch, the kV and MV behaviors of CNR as a function of thickness are distinctly different. In the case of kV and for a given pitch, CNR is relatively insensitive to changes in thickness (as seen in Fig. 4.8(a)). This insensitivity is a consequence of the roughly constant level of QE under kV imaging conditions (ranging from ~94% to 99% for the thicknesses examined) as well as of the relative independence of MTF and Swank factor to changes in thickness (as described in the previous section). By comparison, in the case of MV and for a given pitch, the value of CNR increases with thickness (as seen in Fig. 4.8(b)) due to the significant increase in QE from ~15% to 80% for the

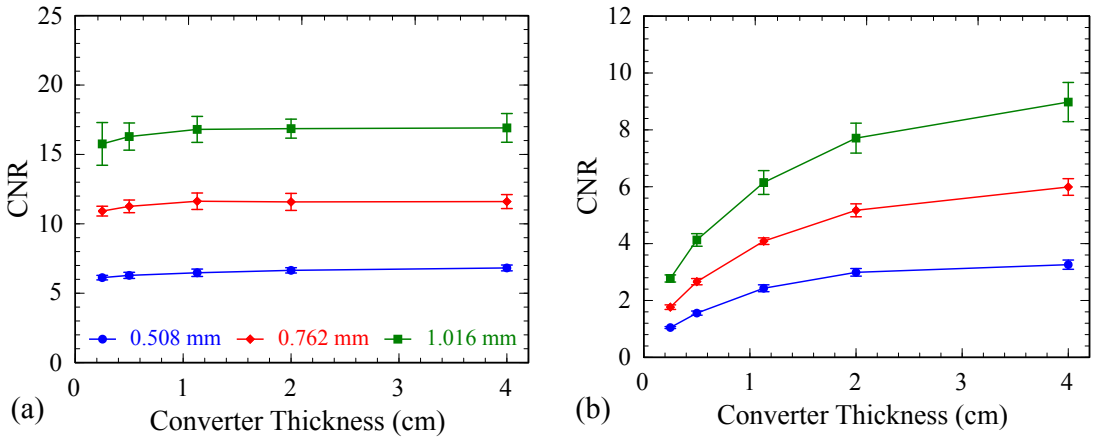

Figure 4.8. Absolute value of CNR as a function of converter thickness and pitch for a phantom insert with a relative electron density of 0.954. The results were obtained using imager designs with the *rear-black* configuration and pitches ranging from 0.508 to 1.016 mm under (a) kV conditions with a $CTDI_W$ of ~0.91 cGy and (b) MV conditions with a $CTDI_W$ of ~3.0 cGy.

thicknesses examined. Note that the increase in CNR exhibits an asymptotic behavior due to diminishing improvement in QE from increased converter thickness. For example, at a pitch of 0.508 mm, while CNR increases by ~32% from 1 to 2 cm, the increase is only ~9% from 2 to 4 cm.

It is clear that the identification of a single segmented scintillator converter design which exhibits performance that fulfills the needs of both kV and MV imaging is hindered by an inherent incompatibility. Specifically, MV imaging favors thicker converter designs with larger pitch so as to achieve higher CNR performance (as discussed in Section III.C in Chapter 3), whereas kV imaging favors smaller pitch to maintain higher MTF performance, while being relatively insensitive to the choice of thickness. For that reason, a converter thickness of ~2 cm would be a favorable choice given the rapidly diminishing returns on MV CNR beyond this thickness,

coupled with considerations of increasing material cost and difficulty of manufacture for thicker scintillators. Moreover, within the bounds of the current study, the preferred converter pitches for kV and MV imaging are 0.508 and 1.016 mm, respectively. This difference could be reconciled either through selection of a common intermediate pitch (e.g., 0.762 mm) or through selection of the smaller pitch in combination with the use of binning for MV (but not for kV) operation, as explored in the next section.

III.C. Comparison of pitch-binning combinations

In this section, additive noise, MV CNR and MTF performance are examined for the various combinations of converter pitches and binning modes schematically depicted in Fig 4.9. Figures 4.9(a) through 4.9(c) illustrate cases corresponding to pitches of 0.508, 0.762 and 1.016 mm with 1×1 binning (i.e., full resolution readout with no binning). These combinations, which result in sampling pitches of 0.508, 0.762 and 1.016 mm, are denoted as $508_{1\times1}$, $762_{1\times1}$ and $1016_{1\times1}$, respectively. Figures 4.9(d) and 4.9(e) illustrate the combinations of a 0.508 mm pitch and two different 2×2 binning modes (both corresponding to a sampling pitch of 1.016 mm) which are denoted as $508_{2\times2}^{quad}$ and $508_{2\times2}^{pair}$, respectively. While the binning of $508_{2\times2}^{quad}$ is performed in a post-acquisition (i.e., purely digital) manner, that of $508_{2\times2}^{pair}$ is a two-step process where the first step is a dual gate line readout [3, 4] resulting in 2×1 analog binning, followed by 1×2 digital binning. This two-step binning mode offers the advantage of faster image acquisition (by virtue of

simultaneous readout of pairs of gate lines) and reduced preamplifier noise.[3, 4] Values for TFT reset thermal noise, preamplifier noise and total additive noise used in the CNR calculations for the different pitch-binning combinations of Fig. 4.9 are summarized in Table 4.2.

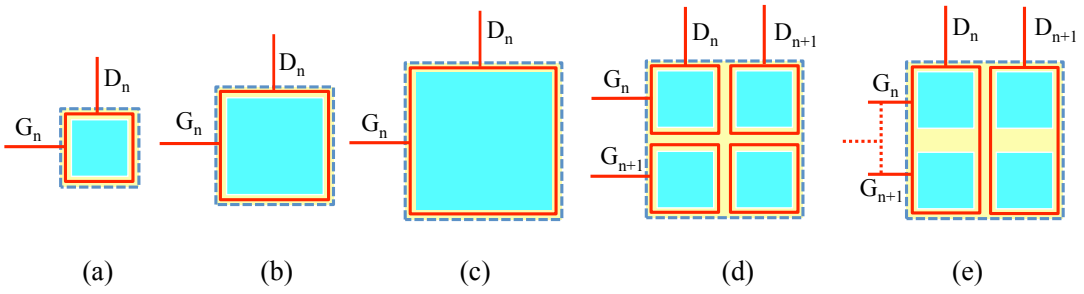

Figure 4.9. Schematic representations of the various pitch-binning combinations examined in the study: (a) $508_{1\times1}$, (b) $762_{1\times1}$, (c) $1016_{1\times1}$, (d) $508_{2\times2}^{quad}$, and (e) $508_{2\times2}^{pair}$. In the drawings, D_n and D_{n+1} represent array data lines, while G_n and G_{n+1} represent array gate lines. Note that in (e), two gate lines are read out at the same time, indicated by the dotted line connecting them. The solid shaded squares represent the cross-section of scintillator elements, the solid frames represent the readout area, and the dashed squares represent the area corresponding to the sampling pitch. See text for further details.

Table 4.2. Estimates of the TFT reset thermal noise $\boldsymbol{\sigma_{TFT-thermal}}$, preamplifier noise $\boldsymbol{\sigma_{amp}}$ and the total additive noise $\boldsymbol{\sigma_{total}}$ of the various pitch-binning combinations calculated using Eqs. (4.1), (4.3) and (4.4).

Pitch-binning Combination	$\mathbf{508_{1\times1}}$	$\mathbf{762_{1\times1}}$	$\mathbf{1016_{1\times1}}$	$\mathbf{508_{2\times2}^{quad}}$	$\mathbf{508_{2\times2}^{pair}}$
Converter Pitch (mm)	0.508	0.762	1.016	0.508	0.508
Sampling Pitch (mm)	0.508	0.762	1.016	1.016	1.016
$\boldsymbol{\sigma_{TFT-thermal}}$ (e^- [rms])	2408	3611	4816	4816	4816
$\boldsymbol{\sigma_{amp}}$ (e^- [rms])	2010	2010	2010	4020	2843
$\boldsymbol{\sigma_{total}}$ (e^- [rms])	3137	4133	5219	6273	5593

Figure 4.10 shows the MV CNR performance for designs incorporating the various pitch-binning combinations. Note that, due to their similar additive noise and identical signal performance, $508_{2\times2}^{quad}$ and $508_{2\times2}^{pair}$ exhibit nearly identical CNR values and therefore only the results for $508_{2\times2}^{quad}$ are shown. For the three combinations with no binning, CNR increases with converter pitch for a given thickness, and increases with converter thickness for a given pitch – in both cases due to increased numbers of detected x-ray quanta per scintillator element. For all converter thicknesses, $508_{2\times2}^{quad}$ exhibits systematically lower (~15% to 21%) CNR compared to that of $1016_{1\times1}$, despite having identical sampling pitch. This is

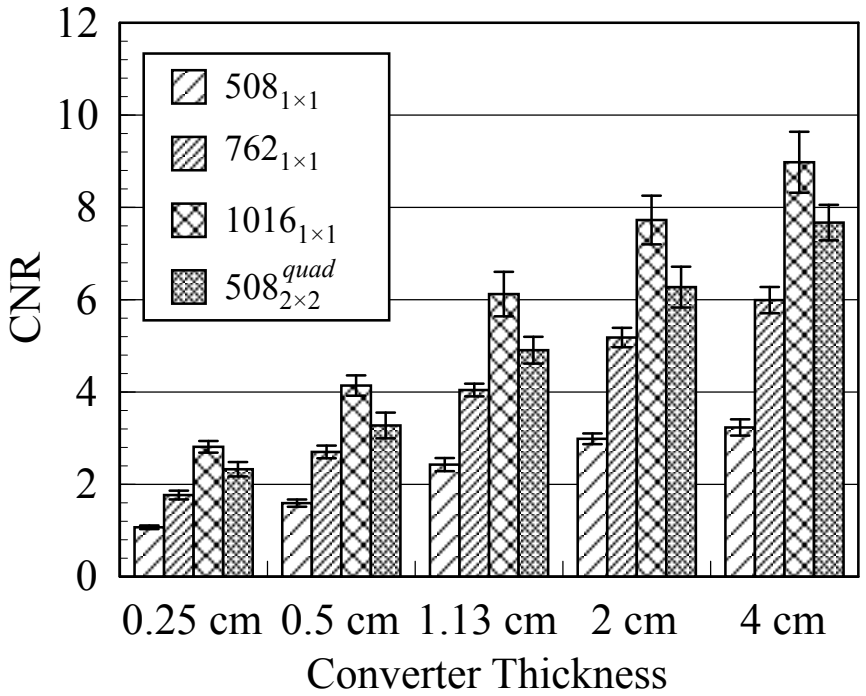

Figure 4.10. Absolute value of CNR under MV imaging conditions as a function of converter thickness for a phantom insert with a relative electron density of 0.954. These results were obtained using converters corresponding to various pitch-binning combinations.

primarily a consequence of two contributing factors – increased Swank noise due to a larger aspect ratio for the scintillator elements,[26] as well as reduced QE due to the displacement of BGO crystal by more septal wall material. However, $508_{2\times2}^{quad}$ exhibits systematically higher (~21% to 31%) CNR compared to $762_{1\times1}$ – largely as a result of increased numbers of sampled x-ray quanta.

Figure 4.11 shows the MV MTF performance for 2 cm thick converters corresponding to various pitch-binning combinations. As a result of binning, the MTF for $508_{2\times2}^{quad}$ (which is the same as that for $508_{2\times2}^{pair}$) falls off more rapidly with spatial frequency compared to the MTF for $508_{1\times1}$, resulting in a relative difference of

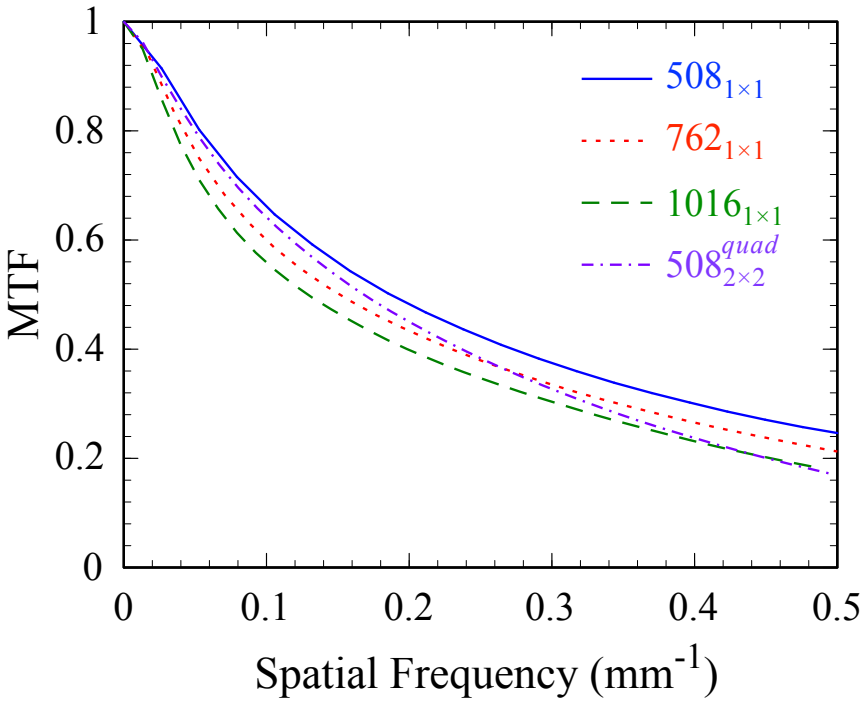

Figure 4.11. MV MTF results for 2 cm thick converters corresponding to various pitch-binning combinations.

~25% at a frequency of 0.49 mm^{-1} (the Nyquist frequency for a sampling pitch of 1.016 mm). However, despite having the same sampling pitch, the MTF for $508_{2\times2}^{quad}$ is systematically higher than that for $1016_{1\times1}$ almost up to the Nyquist frequency, due to more constrained optical lateral spread as a result of more septal wall material in the path of optical photons for the former combination. Note that $762_{1\times1}$ and $508_{2\times2}^{quad}$ demonstrate somewhat comparable MTF, with the former and latter combinations exhibiting slightly better performance at spatial frequencies above and below ~0.26 mm^{-1}, respectively.

In light of the various findings reported above, and under the assumptions of the current study, our results suggest that the most advantageous design for a dual energy imager based on BGO would incorporate a converter with a 0.508 mm pitch and 2 cm thickness, operated using the rear-illumination configuration and coupled to a black reflector. The imager should be operated at full resolution for kV imaging (i.e., $508_{1\times1}$) and 2×2 binning mode for MV imaging (i.e., $508_{2\times2}^{quad}$). An example of the CBCT performance of such an imager is provided in the next section.

III.D. Performance of the proposed dual energy imager

Reconstructed CBCT images of the contrast phantom obtained from imagers incorporating various converter designs are shown in Fig. 4.12. Figures 4.12(a) and 4.12(b) show simulated MV and kV CBCT images acquired from the proposed BGO-based dual energy imager (referred to as the BGO imager) corresponding to pitch-

binning combinations of $508_{2\times2}^{quad}$ and $508_{1\times1}$, respectively. Compared with the MV image (obtained at ~3.0 cGy), the kV image exhibits superior soft-tissue visualization by virtue of better CNR performance, despite the use of a much smaller dose of~0.91 cGy – a result of higher contrast and lower noise under kV conditions. It is of interest to note that, for the insert in the lower left of each image, the gray scale relative to the background is reversed between the kV and MV images. This is likely a result of the specific chemical composition of that insert, combined with the difference in the dominant x-ray interaction mechanisms and their behaviors under kV and MV imaging conditions: the photoelectric effect under kV conditions, which scales with the fourth power of electron density; and the Compton effect under MV conditions, which scales linearly with electron density. For purposes of comparison, Fig. 4.12(c) shows a kV CBCT image for a simulated imager based on a 600 μm

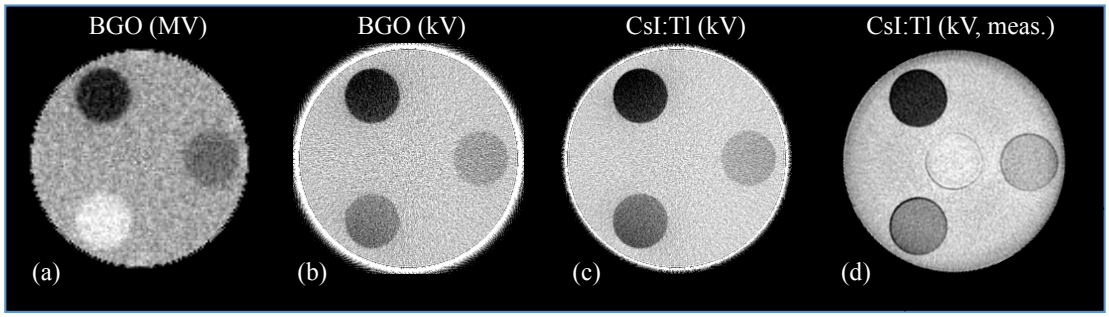

Figure 4.12. Reconstructed CBCT images obtained from a simulated imager based on a 2 cm thick BGO converter and corresponding to pitch-binning combinations of (a) $508_{2\times2}^{\text{quad}}$ at 6 MV, and (b) $508_{1\times1}$ at 100 kVp. For purposes of comparison, CBCT images obtained under 100 kVp from (c) a simulated imager based on a 600 μm thick CsI:Tl converter and (d) a Varian OBI are also shown. Note that the MV CBCT image was obtained at a $CTDI_W$ of ~3.0 cGy, while all kV CBCT images were obtained at a $CTDI_W$ of ~0.91 cGy. The reconstructed voxel pitches for the four images in (a) through (d) are ~0.98, ~0.49, ~0.49 and ~0.65 mm, respectively. Also note that the relative electron densities of the inserts (clockwise from the top) are 0.954, 0.988 and 1.049.

thick CsI:Tl converter (referred to as the CsI:Tl imager), representing the type of kV CBCT imagers used in radiotherapy treatment rooms. The simulation used the same general framework employed for the BGO imager, but with a value of 63% assumed for the optical coupling efficiency of the photodiode for light emitted by CsI:Tl. However, for the simulation of radiation effects, the columnar-structured CsI:Tl used in clinical imagers was approximated as a homogenous layer with a packing density of 75%.[28] For optical effects, optical spread was accounted for through use of the optical MTF deduced from the reported system MTF of a commercial kV CBCT imager based on CsI:Tl,[29] while optical Swank noise was neglected given that the Swank factor is close to unity under kV conditions.[28] Moreover, the same additive noise level as that used for the BGO imager simulations was assumed. The kV image obtained from the CsI:Tl imager (Fig. 4.12(c)), exhibits visual traits similar to those in the kV image obtained from the BGO imager (Fig. 4.12(b)) – except for a slight difference in contrast for the lower left insert. This difference is largely due to the difference in spectral response between CsI:Tl and BGO scintillator material.

Quantitatively, CNR values extracted from the image obtained from the CsI:Tl imager (Fig. 4.12(c)) are higher than those extracted from the image obtained from the BGO imager (Fig. 4.12(b)) by ~22% to 44% for the three inserts. For the BGO image, CNR performance was degraded as a result of the filtration of incident X rays by the 1 mm thick layer of glass substrate in the rear illumination configuration, and by the detrimental effect of additive noise on CNR resulting from the relatively modest optical yield of the BGO material (~8,000 photons per MeV deposited

energy). By comparison, for the CsI:Tl image, there is no filtration effect (since rear illumination is not used) and the additive noise has negligible effect on CNR due to the much larger optical yield of CsI:Tl (~54,000 photons per MeV deposited energy). For comparison, Fig. 4.12(d) shows an image obtained from a commercial kV CBCT system employing a CsI:Tl converter and a physical phantom [4] whose chemical composition was the basis for the simulated phantom. The slight differences between the simulated and measured CBCT images shown in Figs. 4.12(c) and 4.12(d) are believed to be due to inhomogeneities in the physical phantom (including air gaps around the inserts and at the center)[4] and/or differences between the reconstruction algorithm used for the simulation results and that employed in the commercial system.

Figure 4.13 shows simulated results for radiation MTF (obtained in the absence of optical effects) and system MTF, both obtained under kV imaging conditions for the BGO and CsI:Tl imagers. The imagers have nearly identical radiation MTFs, with the BGO imager exhibiting a slight advantage at higher frequencies (e.g., ~4% at the Nyquist frequency). However, after the inclusion of optical effects, system MTF for the BGO imager is lower than that for the CsI:Tl imager. This difference is mainly due to the greater lateral spread of optical photons in the BGO converter, which is a consequence of the use of thicker scintillator material and the non-ideal optical isolation of the septal walls.

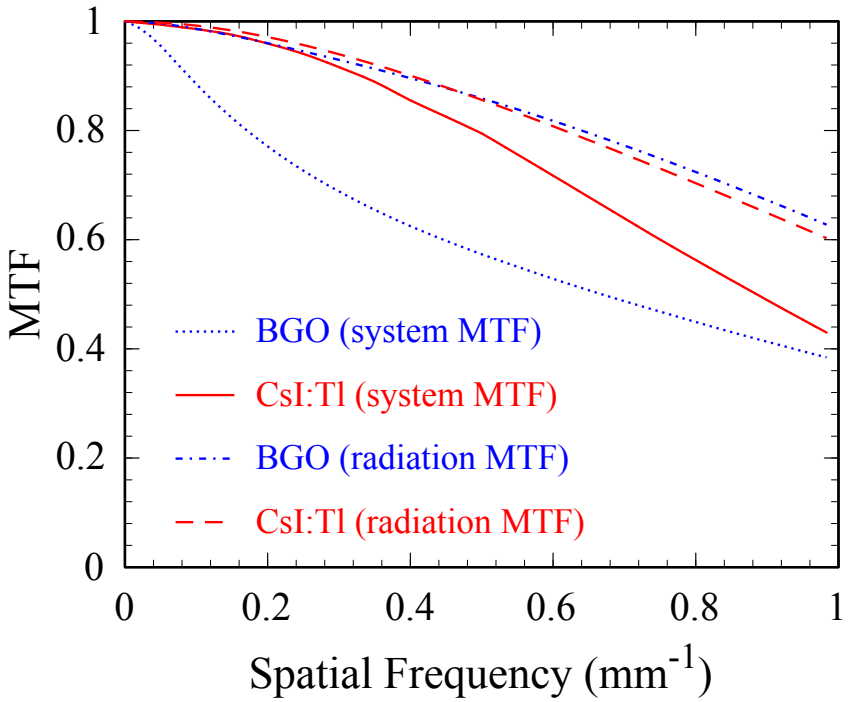

Figure 4.13. Results for system MTF and radiation MTF obtained under kV irradiation conditions for the same simulated BGO and CsI:Tl imagers used to generate the images in Figs. 4.12(b) and 4.12(c), respectively.

IV. SUMMARY AND DISCUSSION

In this study, theoretical modeling through Monte Carlo simulation has demonstrated that, through careful design, a single imager based on a thick, segmented BGO scintillator should be able to achieve soft tissue visualization at low, clinically practical doses by virtue of high QE for MV imaging, while helping to preserve the high spatial resolution and high contrast offered by kV imaging. Such a dual energy imager could facilitate simplification of current treatment room imaging systems and their associated quality assurance. In addition, such an imager operated in conjunction with a treatment machine offering coincident kV and MV FOVs could reduce geometric uncertainties and facilitate more precise integration of kV and MV imaging information.

Beyond the constraints and assumptions of the present study, a number of observations relating to the methodology used are as follows.

For converters with septal walls providing improved optical properties (i.e., increased and reduced septal wall reflectivity and absorption, respectively), it is anticipated that the *rear-black* configuration would remain the most favorable imaging configuration for a dual-energy (i.e., kV and MV) imager – although with a diminished relative advantage compared to the other configurations. For that configuration and with septal walls that provide improved optical isolation, MTF and CNR would increase and decrease, respectively – due to reduced lateral spread of optical photons. While MTF and CNR would still be largely independent of converter thickness under kV conditions, for MV conditions the increase in CNR as a function of converter thickness would be even less pronounced for thicknesses larger than ~2 cm, thereby continuing to favor the choice of a thickness of ~2 cm.

The hypothetical converter designs examined in this study incorporate segmented scintillators of unfocused, rectangular cuboid crystal shapes, which are more practical to manufacture than focused shapes. However, this necessarily makes the reported performance results subject to the detrimental effect of beam divergence, as reported in reference 30 and Chapter 2. While this effect is small as a result of the relatively limited detection area examined in this study (which restricted the maximum divergence angle to ~3°), for imagers with larger detection area and for locations further away from the central beam axis, this effect would be more

pronounced, especially for MV imaging conditions. (Note that for kV imaging conditions, this effect is almost negligible due to the fact that most of the kV X rays are stopped in the initial ~2 mm of BGO material near the entrance surface, as shown in Fig. 4.1.) Although the effect of beam divergence would lead to degradation in MTF for all imaging configurations, it is expected that the *rear-black* configuration would remain the overall most favorable configuration. In addition, since the beam divergence effect does not affect noise (as discussed in Section III.B. in Chapter 2), CNR would remain the same, maintaining the choice of the most favorable converter design as well.

For imagers incorporating BGO converters, while the *rear-black* configuration generally provides superior performance compared to that of other configurations, under kV imaging conditions CNR performance is expected to be lower than that of commercial kV CBCT systems employing CsI:Tl converters. This lower CNR performance can be partly attributed to the reversed position of the AMFPI array glass substrate, which causes filtration of the low energy component of the kV spectrum. (Such an effect is negligible under MV imaging conditions.) However, this detrimental effect could be mitigated through the use of a thinner substrate and/or a less dense substrate material such as plastic. In fact, flexible substrates made of plastic are under investigation for adoption into AMFPI array designs by virtue of their robustness compared to glass.[31, 32]

The converter designs examined in this study are based on BGO, which has an optical yield of ~8,000 photons per MeV of deposited energy. Due to this relatively low yield compared to that of other common inorganic scintillator materials, the performance of imagers incorporating BGO converters is more affected by additive noise, especially for kV imaging which utilizes much smaller doses than MV imaging, as reported in Section III-D. Other scintillator materials with higher yield, such as $CdWO_4$ and LYSO (having yields of ~12,000 to 15,000 and ~32,000 photons per MeV of deposited energy, respectively), would be good candidates for minimizing the effect of additive noise in order to improve CNR – thus helping to achieve quantum-limited behavior for both kV and MV imaging.

The methodology presented in this chapter for investigating the design of an imager to be operated at both diagnostic and radiotherapy energies should be applicable to other dual imaging conditions as well. For example, given the recent availability of treatment machines offering an additional, relatively low MV x-ray beam with a greater diagnostic spectral component to facilitate higher-contrast imaging,[1, 2] the present methodology could help to guide the design of an imager that would provide the most advantageous combined performance with the treatment and imaging beams. Finally, the possibility of extending the current methodology to include consideration of dosimetric capabilities in imager design is of interest and is under investigation.

REFERENCES – CHAPTER 4

[1] D. Roberts, V. Hansen, M. Thompson, G. Poludniowski, A. Niven, J. Seco and P. Evans, "Kilovoltage energy imaging with a radiotherapy linac with a continuously variable energy range," Med. Phys. **39**, 1218-1226 (2012).

[2] D. Parsons, J. L. Robar and D. Sawkey, "A Monte Carlo investigation of low-Z target image quality generated in a linear accelerator using Varian's VirtuaLinac," Med. Phys. **41**, 021719 (2014).

[3] Y. Wang, L. E. Antonuk, Q. Zhao, Y. El-Mohri and L. Perna, "High-DQE EPIDs based on thick, segmented BGO and CsI:Tl scintillators: Performance evaluation at extremely low dose," Med. Phys. **36**, 5707-5718 (2009).

[4] Y. El-Mohri, L. E. Antonuk, Q. Zhao, R. B. Choroszucha, H. Jiang and L. Liu, "Low-dose megavoltage cone-beam CT imaging using thick, segmented scintillators," Phys. Med. Biol. **56**, 1509-1527 (2011).

[5] Y. El-Mohri, L. E. Antonuk, R. B. Choroszucha, Q. Zhao, H. Jiang and L. Liu, "Optimization of the performance of segmented scintillators for radiotherapy imaging through novel binning techniques," Phys. Med. Biol. **59**, 797-818 (2014).

[6] T. Falco and B. G. Fallone, "Characteristics of metal-plate/film detectors at therapy energies. I. Modulation transfer function," Med. Phys. **25**, 2455-2462 (1998).

[7] C. Kausch, B. Schreiber, F. Kreuder, R. Schmidt and O. Dössel, "Monte Carlo simulations of the imaging performance of metal plate/phosphor screens used in radiotherapy," Med. Phys. **26**, 2113-2124 (1999).

[8] M. Lachaine, E. Fourkal and B. G. Fallone, "Investigation into the physical characteristics of active matrix flat panel imagers for radiotherapy," Med. Phys. **28**, 1689-1695 (2001).

[9] J. Yorkston, L. E. Antonuk, Y. El-Mohri, K.-W. Jee, W. Huang, M. Maolinbay, X. Rong, J. H. Siewerdsen and D. P. Trauernicht, "Improved spatial resolution in flat-panel imaging systems," in *Medical Imaging 1998,* (International Society for Optics and Photonics, 1998), pp. 556-563.

[10] F. H. Attix, *Introduction to radiological physics and radiation dosimetry*. (John Wiley & Sons, 2008).

[11] K. Sato, F. Nariyuki, H. Nomura, A. Takasu, S. Fukui, M. Nakatsu, Y. Okada, T. Nabeta and Y. Hosoi, "Effect of x-ray incident direction and scintillator layer design on image quality of indirect-conversion flat-panel detector with GOS phosphor," in *Medical Imaging 2011,* (International Society for Optics and Photonics, 2011), pp. 79614I-79614I.

[12] S. Rivetti, N. Lanconelli, M. Bertolini, A. Nitrosi and A. Burani, "Characterization of a clinical unit for digital radiography based on irradiation side sampling technology," Med. Phys. **40**, 101902 (2013).

[13] Y. Yano, H. Yabuuchi, N. Tanaka, J. Morishita, T. Akasaka, Y. Matsuo, S. Sunami, T. Kamitani, M. Jinnouchi and Y. Yamasaki, "Detectability of simulated pulmonary nodules on chest radiographs: Comparison between

irradiation side sampling indirect flat-panel detector and computed radiography," European journal of radiology **82**, 2050-2054 (2013).
[14] N. Tanaka, Y. Yano, H. Yabuuchi, T. Akasaka, M. Sasaki, M. Ohki and J. Morishita, "Basic imaging properties of an indirect flat-panel detector system employing irradiation side sampling (ISS) technology for chest radiography: comparison with a computed radiographic system," Radiological Physics and Technology **6**, 162-169 (2013).
[15] I. Kawrakow and D. W. O. Rogers, "The EGSnrc Code System: Monte Carlo Simulation of Electron and Photon Transport," Technical Report PIRS–701, National Research Council of Canada, Ottawa, Canada (2000).
[16] I. Kawrakow, "egspp: the EGSnrc C++ class library," Technical Report PIRS-899, National Research Council of Canada, Ottawa, Canada (2005).
[17] J. M. Boone and J. A. Seibert, "An accurate method for computer-generating tungsten anode x-ray spectra from 30 to 140 kV," Med. Phys. **24**, 1661-1670 (1997).
[18] D. Sheikh-Bagheri, Ph.D. Thesis, Carleton University, 1999.
[19] S. Agostinelli, et al., "GEANT4–a simulation toolkit," Nucl. Instrum. Meth. A **506**, 250-303 (2003).
[20] M. Maolinbay, Y. El-Mohri, L. Antonuk, K.-W. Jee, S. Nassif, X. Rong and Q. Zhao, "Additive noise properties of active matrix flat-panel imagers," Med. Phys. **27**, 1841-1854 (2000).
[21] P. A. Tipler and G. Mosca, *Physics for scientists and engineers*, 6 ed. (Freeman, W. H. & Company, New York, NY, 2007).
[22] L. E. Antonuk, Q. Zhao, Y. El-Mohri, H. Du, Y. Wang, R. A. Street, J. Ho, R. Weisfield and W. Yao, "An investigation of signal performance enhancements achieved through innovative pixel design across several generations of indirect detection, active matrix, flat-panel arrays," Med. Phys. **36**, 3322-3339 (2009).
[23] M. Maolinbay, T. Zimmerman, R. Yarema, L. Antonuk, Y. El-Mohri and M. Yeakey, "Design and performance of a low noise, 128-channel ASIC preamplifier for readout of active matrix flat-panel imaging arrays," Nuclear instruments and methods in physics research section A: Accelerators, Spectrometers, Detectors and Associated Equipment **485**, 661-675 (2002).
[24] M. F. Fast, T. Koenig, U. Oelfke and S. Nill, "Performance characteristics of a novel megavoltage cone-beam-computed tomography device," Phys. Med. Biol. **57**, N15-N24 (2012).
[25] H. Fujita, D. Tsai, T. Itoh, K. Doi, J. Morishita, K. Ueda and A. Ohtsuka, "A simple method for determining the modulation transfer function in digital radiography," IEEE Trans. Med. Imag. **11**, 34-39 (1992).
[26] Y. Wang, L. E. Antonuk, Y. El-Mohri and Q. Zhao, "A Monte Carlo investigation of Swank noise for thick, segmented, crystalline scintillators for radiotherapy imaging," Med. Phys. **36**, 3227-3238 (2009).
[27] R. K. Swank, "Absorption and noise in x-ray phosphors," J. Appl. Phys. **44**, 4199-4203 (1973).

[28] W. Zhao, G. Ristic and J. A. Rowlands, "X-ray imaging performance of structured cesium iodide scintillators," Med. Phys. **31**, 2594-2605 (2004).
[29] E. Samei, "Image quality in two phosphor-based flat panel digital radiographic detectors," Med. Phys. **30**, 1747-1757 (2003).
[30] Y. Wang, Y. El-Mohri, L. E. Antonuk and Q. Zhao, "Monte Carlo investigations of the effect of beam divergence on thick, segmented crystalline scintillators for radiotherapy imaging," Phys. Med. Biol. **55**, 3659-3673 (2010).
[31] R. A. Street, W. S. Wong and R. Lujan, "Curved electronic pixel arrays using a cut and bend approach," Journal of Applied Physics **105**, 104504 (2009).
[32] R. A. Street, "Jet Printed TFTs and Circuits for Flexible Electronics," SID Symposium Digest of Technical Papers **44**, 267-270 (2013).

CHAPTER 5

SUMMARY AND CONCLUSION

In this dissertation, a series of theoretical studies were performed using Monte Carlo simulation to optimize the design of AMFPIs based on segmented scintillators for radiotherapy imaging applications. The influence of imager design specifications (such as use of a focused geometry, as well as the physical size and optical properties of scintillator elements) on imager performance, under MV only or dual energy conditions (i.e., MV and kV), has been systematically investigated.

As a potential solution to counter the detrimental effect of beam divergence on thick detectors, segmented scintillators with a focused geometry were theoretically investigated in Chapter 2. A focused planar geometry was found to effectively eliminate degradation in MTF and DQE due to beam divergence, achieving uniform imaging performance across the entire detection area for large-area, thick, segmented scintillators. Although the arrangement of scintillator elements on a planar surface would likely be more practical to implement than an arrangement on a spherical cap, the manufacturing and positioning of elements with thousands of different shapes, as well as the sensitivity of the focused imager to lateral displacement could present challenges.

A theoretical study involving simulation of both radiation and optical transport was performed to examine the influence of optical effects on the imaging performance of segmented scintillators. In Chapter 3, a hybrid modeling technique was devised to circumvent the prohibitive computational burden associated with brute-force Monte Carlo simulation of optical transport, successfully accounting for the optical effects on practical computational timescales. Based on the theoretical examination of various segmented scintillator designs, an optimization map, which takes into account CNR and spatial resolution performance, was generated to guide decision-making in scintillator design.

Beyond the encouraging performance of thick, segmented scintillators which increase DQE and CNR for MV imaging, the possibility of extending their clinical application to include kV imaging was also explored. Chapter 4 presented a methodology for identifying the most favorable design of a dual energy imager based on the segmented scintillator approach. Such a design maintains the desirably high level of imaging performance at MV energies made possible by thick, segmented scintillators, while helping to provide performance comparable to that of commercial imagers at kV energies. The capability to acquire high quality images under both kV and MV imaging conditions using a single detector could facilitate simplification of the equipment presently used for kV and MV imaging in the treatment room, as well as reduce the quality assurance effort associated with such systems. The methodology used in this study is expected to be applicable to the design of imagers for other dual energy imaging conditions.

Future work on the development of imagers employing segmented scintillators could include manufacture and characterization of prototypes based on scintillating materials with desirable properties similar to those of BGO, but with a higher optical yield – such as $CdWO_4$. Moreover, reduction of optical crosstalk between neighboring scintillator elements could be achieved through use of septal wall material with higher reflectivity which could provide improved optical isolation. In addition, it may be possible to obtain more accurate parameters used for optical simulations through measurements involving individual scintillator elements.

In conclusion, the theoretical studies presented in this dissertation, which build upon the results of earlier theoretical and empirical characterizations of engineering prototypes, provide valuable insight for the design of future prototypes. It is anticipated that, through careful design assisted by theoretical modeling and empirical measurements, AMFPIs based on segmented scintillators can provide significantly improved performance compared to that of existing imagers in the treatment room, thereby increasing the clinical utility of in-room kV and MV imaging.

APPENDICES

APPENDIX A

FILL FACTORS FOR VARIOUS ELEMENT ARRANGEMENTS IN FOCUSED SEGMENTED SCINTILLATORS

For the warped rectangular and concentric ring arrangements of individual scintillating crystals on a spherical cap illustrated in Figs. 2.2(a) and 2.2(b), respectively, of Chapter 2, the fill factors are both less than 100%. Moreover, the fill factors for these arrangements of a curved, focused scintillator geometry would vary with the solid angles subtended by each crystal and by the entire converter. For the example of a converter positioned at a distance of 130 cm from the x-ray source, with a base diameter of 40 cm, a crystal cross-sectional dimension of 1016×1016 μm^2, and with no minimum septal wall thickness, the fill factors would be, at most, 97.2% (rectangular) and 94.3% (ring). However, the presence of septal walls having a minimum thickness would cause further reduction in fill factor. For the aforementioned setup, a crystal cross-sectional dimension of 966×966 μm^2 and a minimum septal wall thickness of 50 μm lead to fill factors of 87.9% (rectangular) and 85.3% (ring), while a 916×916 μm^2 crystal and a minimum septal wall thickness of 100 μm lead to fill factors of 79.0% (rectangular) and 76.7% (ring).

By comparison, for the rectilinear grid arrangement of individual scintillating crystals of a focused, planar scintillator geometry, as illustrated in Fig. 2.2(c), while the nominal fill factor would be 100%, fill factor would decrease with the introduction of septal walls. For example, for elements with a pitch of 1016 μm, fill factor would be reduced to 90.4% and 81.3% for wall thicknesses of 50 and 100 μm, respectively, independent of the area of the overall scintillator. Thus, for comparable element sizes and septal wall thicknesses, the fill factor of the rectilinear grid arrangement is greater than that of warped rectangular and concentric ring arrangements discussed above.

APPENDIX B

ELEMENT SHAPES OF PLANAR FOCUSED SEGMENTED SCINTILLATORS

For the rectilinear grid arrangement of a planar, focused segmented scintillator geometry such as schematically illustrated in Figs. 2.1(d) and 2.3 of Chapter 2, the individual elements have the shape of a frustum and the volume of each element, V, is given by:

$$V = \frac{h}{3}\left(A_t + A_b + \sqrt{A_t A_b}\right), \qquad (B.1)$$

where h is the perpendicular height of the frustum, A_t and A_b are the areas of the top and bottom surfaces of the frustum, respectively, and A_t is always less than A_b. Since the element-to-element pitch on the top surface and on the bottom surface remain constant across the scintillator, A_t and A_b also remain constant. In addition, all the elements share the same perpendicular height h (which is equal to the scintillator thickness). Therefore, according to Eq. (B.1), all the elements for a given rectilinear grid arrangement have the same volume, despite the variation in shape of those elements across the scintillator.

For each frustum-shaped element, although the cross-sectional area of the scintillator crystal and that of the entire element varies along the thickness of the scintillator (both becoming smaller going from the bottom to the top surface), the ratio of these two areas remains constant and is equal to the fraction of entire element volume occupied by scintillator crystal (i.e., the fill factor). In the case of a converter with an element pitch of 1016 μm on the bottom surface and 100 μm septal walls, the fill factor of an element is ~81.3%, as given by $(\frac{1016-100}{1016})^2$, across the entire converter.

APPENDIX C

A UNIFIED INPUT FILE GENERATOR FOR EGSnrc

For the radiation transport simulations reported in Chapters 2 to 4 which used the simulation package EGSnrc, the particle source, the geometry in which the particles are transported and the various algorithm options (e.g., switches for enabling different physical mechanisms, initialization parameters, etc.) are specified in an input file. The content of this input file varies due to geometry changes that depend upon the purpose of the simulation (i.e., to determine MTF, NPS, QE or CBCT), or due to different imager designs, or due to required changes in the initialization parameters. The calculation performed based on a specific file is denoted as a simulation *job*. To facilitate the generation of input files for various simulation jobs, a unified input file generator for EGSnrc was created using MATLAB.

In the unified input file generator, various parameters are specified to determine the purpose of the simulation, describe the geometries of the radiation source and of the objects to be irradiated (i.e., the phantom and imager), and define random number seeds. The parameters and the possible values that these parameters could take are listed in Table C.1. The input files created by the generator are properly formatted to conform to the syntax specified by the egspp package, a library

Table C.1. A brief summary of various parameters in the unified input file generator.

Category	Parameter	Possible values/Notes
General	Simulation purpose	MTF; NPS; QE; CBCT
Converter	Overlying layer material	Copper (for MV); Air (for kV)
	Focused scintillator	Unfocused or focused
	Scintillator material	CsI; BGO; LYSO; $CdWO_4$
	Septal wall material	Polystyrene (with optical isolation); or the same as scintillator material (without optical isolation)
	Scintillator thickness	In centimeters
	Element-to-element pitch	In centimeters
	Septal wall width	In centimeters
	Matrix format of elements	Depends on simulation type
	Source to detector distance (SDD)	In centimeters
	Positional shift	Lateral shift (in x- or y-direction); SDD shift (in z-direction)
Phantom	Insert set number	Four sets (corresponding to a total of 12 inserts as detailed in Table 3.1 in Chapter 3); only enabled for CBCT
	Phantom rotation angle	In degrees
	Phantom diameter	In centimeters
	Phantom insert diameter	In centimeters
	Phantom position	In z-direction
Source	Source spectrum	6 MV; 100 kVp
	Number of histories	Depends on simulation type
Initialization	Random seeds	Two integers between 1 and 30,000 (range specified by EGSnrc)

of C++ classes which was developed to extend the utility of EGSnrc and to facilitate geometry definition.

There are two modes of operation for the unified input file generator: *stand-alone* and *batch*. The stand-alone mode should be used for the simulation of MTF or QE, each of which generally requires only one input file for a certain geometry. For

the simulation of NPS and CBCT, each of which requires large numbers of input files with the same geometry, the script should be operated in the batch mode.

APPENDIX D

PARALLELIZATION OF CBCT SIMULATION

The simulation of CBCT for imagers incorporating various converter designs (as reported in Chapters 3 and 4) was performed using parallel processing on Skynet, a custom-built Linux *cluster* consisting (at the time of the studies) of ~154 nodes, each with an 8-core CPU (AMD FX-8150 and FX-8350 at ~4 GHz). The calculation workload on each node was managed on a Linux *server* using HTCondor (University of Wisconsin, Madison, WI), a high-throughput computer software framework. Both the cluster and the server have access to a network file system, where the files required for the simulation are stored and the simulation results are transferred to and analyzed.

The CBCT simulation for a certain converter design at a certain dose is denoted as a simulation *task*. In order to increase the flexibility of scheduling for parallel execution on the cluster, each *task* is divided, with increasingly finer granularity, into *batches*, *rotations* and *projections*. This hierarchical structure is organized into a 3-level folder structure on the network file system, as illustrated in Fig. D.1. At the *projection* level, the simulation of each projection is implemented by

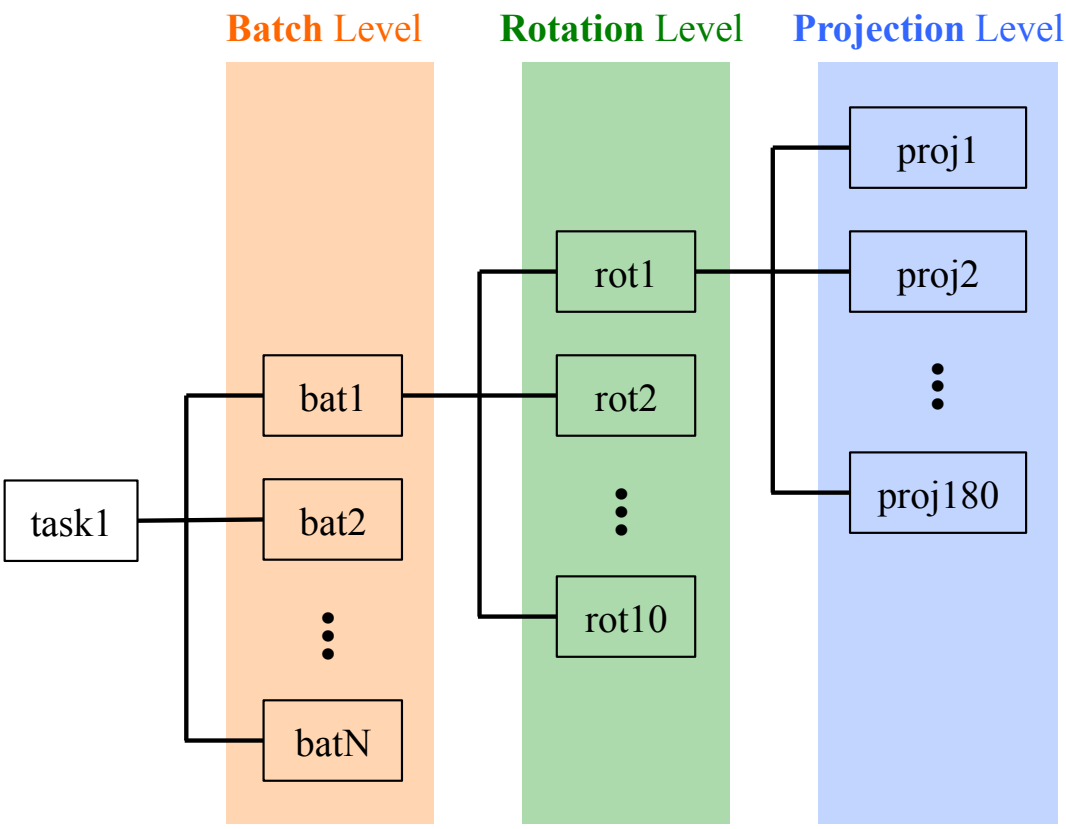

Figure D.1. The folder structure on the network file system used for parallelization of the CBCT simulations. Note that the number of folders on each level is different. For each task, the total number of batches, N, depends on the total dose required for the task.

submitting to the cluster a single simulation *job*, which requires a specific input file (as detailed in Appendix C).

For each *projection*, the simulation job is assigned a number of histories, a pair of random numbers and a projection angle in the corresponding input file. The number of histories is chosen so that the simulation job can be completed in approximately one hour, depending on the purpose and parameter settings of the simulation. The pair of random numbers, which is unique for each *projection*, is used

to initialize the simulation job. The projection angle takes values from 0° to 358° with a 2° separation, and 180 *projections* corresponding to a 360° full scan are grouped into a *rotation*. Every 10 *rotations* are grouped into a *batch*, the total number of which depends on the required dose for the simulation *task*. For example, in order to achieve a total dose of ~3.0 cGy, an MV CBCT simulation *task* such as those performed in Chapter 3 requires 30 *batches*. Since each *batch* consists of 10 *rotations* and each *rotation* consists of 180 *projections*, each *task* corresponds to a total of 54,000 *projections* (i.e., 54,000 simulation jobs).

The successful execution of a simulation job on the cluster requires a number of important files. These files are classified into three categories: (i) script files, which contain Unix commands to create the folder structure and/or to submit jobs to the cluster, or call other script files; (ii) an input file, which specifies the type and settings of each simulation job; and (iii) a submit description file, which defines the rules for the job submission to the cluster and configures the running environment on the cluster node.

Figure D.2 shows the process for the parallelization of a simulation *task*, which can be broken down into 5 steps as follows:

Step 1) Inside the task folder, the script file "batLaunch.sh" creates a *batch* level folder, containing 10 *rotation* folders, each of which in turn contains 180 *projection* folders. Note that for purpose of clearer presentation, only one projection

folder, along with the rotation folder which contain the projection folder is illustrated. The script file "batLaunch.sh" also creates a submit description file "proj1.condor" inside the projection folder.

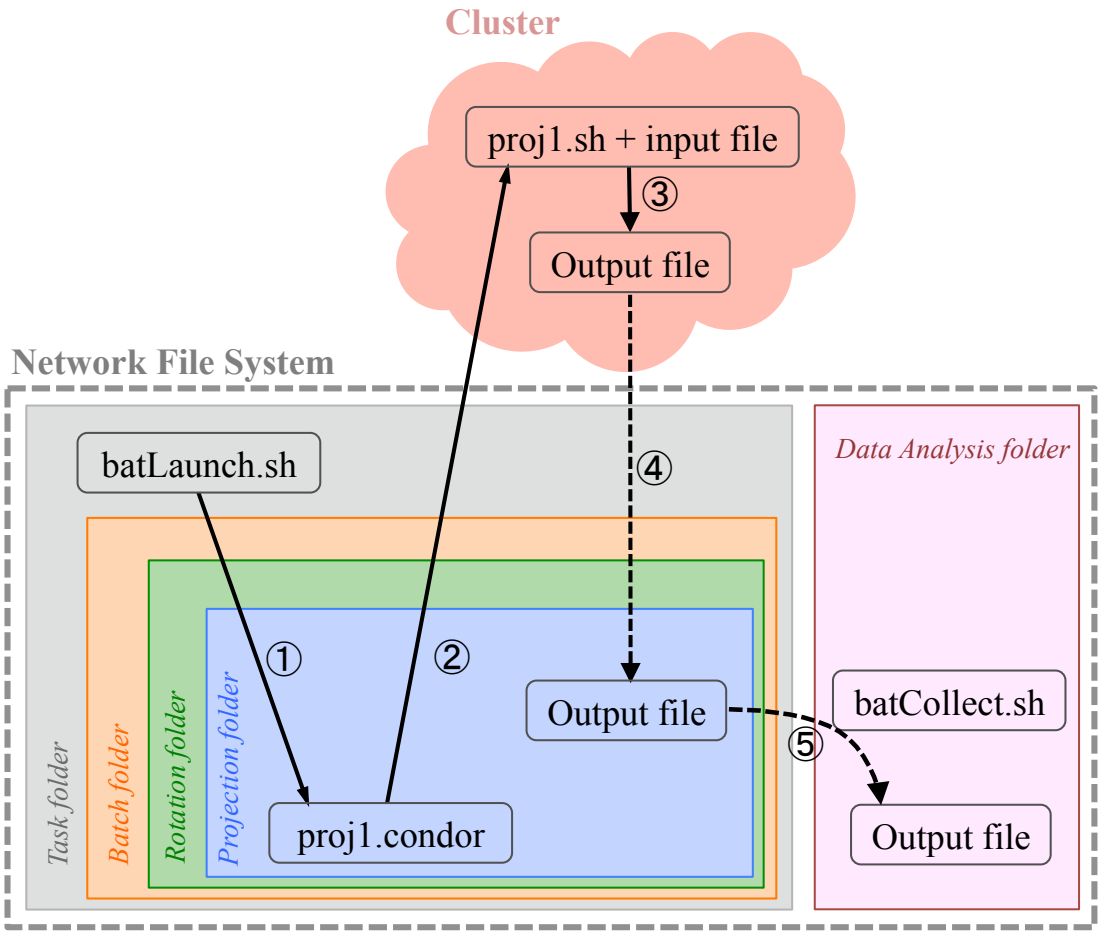

Figure D.2. Schematic diagram of the process for the parallelization of a simulation task. Different steps in the process are marked with circled numbers beside solid or dashed arrows. The solid arrows indicate calling orders of files, pointing from the calling file to the called file, while the dashed arrows indicate the transfer of the same file. The shaded cloud in the top half of the diagram represents the cluster, and the dashed box in the bottom half of the diagram represents the network file system, which hosts a *task-batch-rotation-projection* nested folder structure and a data analysis folder.

Step 2) Within the *projection* folder, the command "condor_submit proj1.condor" submits the job to a core which satisfies the criteria prescribed by the submit description file "proj1.condor". In addition, "proj1.condor" specifies the script file to be executed on the cluster, "proj1.sh".

Step 3) On the cluster, the script file "proj1.sh" is executed to perform the simulation job described by the input file. During each simulation job, temporary files containing intermediate results as well as the output file containing final results are generated and stored in a RAM drive on the node.

Step 4) After successful completion of each simulation, the output file is transferred to the projection folder on the network file system, and the intermediate files are purged from the RAM drive of the node to make room for new simulation jobs.

Step 5) After the completion of all simulation jobs, the script file "batCollect.sh" collects all of the output files into the data analysis folder, where data analysis and/or image reconstruction is performed.